THREE-DIMENSIONAL MAGNETOTELLURIC MODELLING AND INVERSION

by

Stephen Keith Park

B.S. University of California, Riverside (1978)

SUBMITTED TO THE DEPARTMENT OF
EARTH, ATMOSPHERIC, AND PLANETARY SCIENCES
IN PARTIAL FULFILLMENT
OF THE REQUIREMENTS
FOR THE DEGREE OF

DOCTOR OF PHILOSOPHY

at the

MASSACHUSETTS INSTITUTE OF TECHNOLOGY

October 1983

© Massachusetts Institute of Technology 1983

Signature of Author _____

Department of Earth, Atmospheric, and Planetary Sciences
October 27, 1983

Certified by _____
Theodore R. Madden
Thesis Supervisor

Accepted by _____
Theodore R. Madden
Chairman, Committee on Graduate Students

Undergrad
WITHDRAWN
MASSACHUSETTS INSTITUTE OF TECHNOLOGY
NOV 15 1983
MIT LIBRARIES
LIBRARIES

THREE-DIMENSIONAL MAGNETOTELLURIC MODELLING AND INVERSION

by

Stephen Keith Park

Submitted to the Department of Earth, Atmospheric, Planetary Sciences on October 27, 1983 in partial fulfillment of the requirements for the degree of Doctor of Philosophy in Geophysics

ABSTRACT

Distortions of the magnetotelluric fields caused by three-dimensional structures can be severe and are not predictable using one-dimensional and two-dimensional models. While three-dimensional modelling methods have been available for five years (Hohmann and Ting, 1978), these are limited to simple structures. We have developed a practical, efficient,three-dimensional modelling algorithm based on the differential form of Maxwell's equations. We use an extension of Ranganayaki's generalized thin sheet analysis (1978) which allows us to stack heterogeneous layers.

We use this modelling algorithm to examine what kinds of distortion occur near three-dimensional bodies. We have identified three major physical mechanisms governing this distortion: horizontal current gathering; vertical current gathering; and local induction of current loops. We present simple procedures for estimating the order-of-magnitude contribution from each mechanism, given rudimentary knowledge of the structure. Each mechanism produces a different spatial and frequency distortion in the background field, so identification of the dominant mechanism is possible. This identification aids in the qualitative interpretation of field data.

We then use two- and three-dimensional modelling to deduce the structure in the Beowawe Known Geothermal Resource Area in Nevada from magnetotelluric data. An important result from this interpretation is that the truncation along strike of a conductive, two-dimensional body does not affect the electric fields significantly. This insensitivity only occurs when the fields within the conductor are dominated by the local induction mechanism. Two-dimensionality in this case can mean ratios of length to width of 2 or greater.

The theoretical basis for a practical three-dimensional inversion is also presented here. The inversion method

replaces conductivity perturbations with equivalent sources and then applies Lanczos' generalized reciprocal theorem (1956) to derive the surface field sensitivity to a conductivity change at depth. We hope to use this method to examine the question of uniqueness in three-dimensional inversion.

We also present our attempts at solving the multiple scales problem. Ultimately, a practical modelling algorithm must be able to simultaneously account for both regional and local structure. Multiple scales is a method by which many different length scales are included in the same model. We have a better understanding of the problem now, and propose a using a boundary value approach which may bypass the difficulties we encountered. Much work is still needed, however.

Thesis Supervisor: Theodore R. Madden

Title: Professor of Geophysics

ACKNOWLEDGEMENTS

This thesis has been written using the first person plural deliberately. It does not represent just my work. Ted Madden has contributed as much to this work as I have. As I look through the chapters, I realize that virtually all of the intuitive leaps have been his (or subtly suggested by him). I have the greatest admiration for him, despite the fact that it may not have seemed that way sometimes in our interactions. I will greatly miss his friendship and intellectual stimulation when I leave here.

My officemates, both past and present, have also contributed to this thesis and my education. Rambabu Ranganayaki, Adolfo Figueroa-Vinas, Olu Agunlowe, Ru Shan Wu, John Williams, Fran Bagenal, Jia Dong Qian, Bob Davis, and Brian Bennett are among those. A special note of thanks goes to Earle Williams, Gerry LaTorraca, and Dale Morgan, who are not only colleagues but dear friends also.

Gene Simmons, Kei Aki, and Peter Molnar were among those outside of the Geoelectricity Group who provided help along the way. I owe a great debt of gratitude to Renee Zollinger, Ann Leifer, Ellen Brown, Scott Phillips, Darby Dyar, Kaye Shedlock, Kathy Perkins, Wayne Hagman, Mary Reid, and Tom Wissler for helping me through rough times while here. The help from my good friends was appreciated. To all the people who drank beer with me on Wednesdays and Fridays, remember, that is a tradition that must not die!

My parents, Harold and Joan Park, were probably the most instrumental people in getting me here in the first place. Their constant encouragement got me through all this school nonsense to the point I am at now. How do you begin to say thank you? I know of no adequate words.

Thanks go to Shawn Biehler, who sent me here, and Tien Lee, who agreed with him. I still remember Shawn's comment about MIT--"You'll get a damn fine education if you can stand the climate.". I agree wholeheartedly.

I owe thanks to Judy Roos, Sharon Feldstein, Debby Roecker, Jan Natier-Barbaro, Doug Pfeiffer, Jean Titilah, and Ann Harlow for putting up with my unorthodox ways of dealing with the MIT Administration. I am fully convinced MIT would have had me arrested long ago for creative accounting in field work if it had not been for the tolerance and flexibility of these people.

The NSF, USGS, and the Department of Earth and Planetary Sciences have provided financial aid for this work. Chevron Oil Company has provided both the data set and money for some of this work.

TABLE OF CONTENTS

	Page
Title Page	i
Abstract	ii
Acknowledgements	iv
Table of Contents	vi
List of Figures	vii
List of Tables	ix
Definitions of Variables	x
Chapter 1 Introduction	1
1.1 Introduction	1
1.2 Thesis Organization	4
Chapter 2 Three-Dimensional Modelling	6
2.1 Introduction	6
2.2 Thin Sheet Theory	7
2.3 Three-Dimensional Field Behavior	19
2.4 Minimum Phase	55
2.5 Summary	62
Chapter 3 Three-Dimensional Inversion	63
3.1 Introduction	63
3.2 Formulation of the Inverse Problem	65
3.3 Comparison to a Simple 1-D Inversion	78
3.4 Source Terms fo 3-D Inversion	84
3.5 Summary	90
Chapter 4 MT Interpretation in Beowawe, Nevada	91
4.1 Introduction	91
4.2 Geology and Previous Geophysics	92
4.3 MT Interpretation	98
4.4 Effect of Truncation of a 2-D Body	128
4.5 Summary	133
Chapter 5 Multiple Scales	134
5.1 Introduction	134
5.2 Ranganayaki's Approach	136
5.3 Equivalent Sources and Multiple Scales	148
Chapter 6 Summary	151
References	153
Appendix A Error Analysis for Thin Sheet Approximation	157
Appendix B Field Estimation Procedure	167
Appendix C Processing and Interpretation of MT Data	178
Appendix D Rotation of Conductivity Tensor	182
Biographical Note	183

LIST OF FIGURES

	Page
2.2.1 Model with Coordinate System	16
2.2.2 Repetition Assumption	17
2.2.3 Source Condition	18
2.3.1 Current Gathering--Model 1	33
2.3.2 Site 5--Model 1	34
2.3.3 Site 23--Model 1	35
2.3.4 Site 32--Model 1	36
2.3.5 Site 50--Model 1	37
2.3.6 Current Gathering--Model 2	38
2.3.7 Site 5--Model 2	39
2.3.8 Site 23--Model 2	40
2.3.9 Site 32--Model 2	41
2.3.10 Site 50--Model 2	42
2.3.11 Induction-- Model 3	43
2.3.12 Site 5--Model 3	44
2.3.13 Site 23--Model 3	45
2.3.14 Site 32--Model 3	46
2.3.15 Site 41--Model 3	47
2.3.16 Conductor Interactons--Model 4	48
2.3.17 Site 22 with Surface Conductor--Model 4	49
2.3.18 Site 22 without Surface Conductor--Model 4	50
2.3.19 Site 43 with Surface Conductor--Model 4	51
2.3.20 Site 43 without Surface Conductor--Model 4	52
2.3.21 Site 44 with Surface Conductor--Model 4	53
2.3.22 Site 44 without Surface Conductor--Model 4	54
2.4.1 Predictions of Apparent 'Resistivity' from Phase inside Conductor	60
2.4.2 Predictions of Apparent 'Resistivity' from Phase outside Conductor	61
3.2.1 Integration Volume	77
4.2.1 Geologic Map of Beowawe, Nevada	96
4.2.2 Geophysical Investigations of Beowawe, Nevada	97
4.3.1 Beowawe MT Site 1	106
4.3.2 Beowawe MT Site 2	107
4.3.3 Beowawe MT Site 3	108
4.3.4 Beowawe MT Site 4	109
4.3.5 Beowawe MT Site 5	110
4.3.6 Beowawe MT Site 6	111
4.3.7 Beowawe MT Site 7	112
4.3.8 Beowawe MT Site 8	113
4.3.9 Beowawe MT Site 10	114
4.3.10 Beowawe MT Site 11	115
4.3.11 Beowawe MT Site 12	116
4.3.12 Rotation Angles for Sites 1-3	117
4.3.13 Rotation Angles for Sites 4-6	118
4.3.14 Rotation Angles for Sites 7-10	119
4.3.15 Rotation Angles for Sites 11-12	120

4.3.16 Plot of all Sounding Curves Corrected for Surface Heterogeneity 121
4.3.17 Generalized MT Sites 1 and 2 with Curves of Good Fit 122
4.3.18 Model Used to Generate Curves of Good Fit 123
4.3.19 Sensitivity Analysis--Surface Structure 124
4.3.20 Sensitivity Analysis--Lower Crust 125
4.3.21 Sensitivity Analysis--Resistivity Across Strike 126
4.3.22 Sensitivity Analysis--Resistivity Along Strike 127
4.4.1 Simplified Model Used to Study Truncation Effects 132
5.2.1 Multiple Scales Grid 143
5.2.2 Model Used to Compare Ranganayaki's Solution to Correct Solution 144
5.2.3 Comparison of Multiple Scales Solution to Correct Solution 145
5.2.4 Model Used to Compare Improved Multiple Scales Solution to Correct Solution 146
5.2.5 Comparison of Improved Multiple Scales Solution to Correct Solution 147
5.3.1 Proposed Multiple Scales Method 150
A.1.1 Model for Numerical Evaluation of Error Criteria 166
B.1.1 Field Perturbation Mechanisms 175
B.1.2 Anisotropic Quarter-Spaces 176
B.1.3 Two-Dimensional Elliptical Body 177

LIST OF TABLES

		Page
2.3.1	N-S Field Contribution Estimates for 100 Second Periods	31
2.3.1	E-W Field Contribution Estimates for 100 Second Periods	32
4.4.1	Parallel and Perpendicular Resistivities for Various Aspect Ratios	131
A.1.1	Error Analysis for TM Mode	164
A.1.2	Error Analysis for TE Mode	164
A.1.3	Numerical Error Analysis	165

DEFINITION OF VARIABLES

1-D	conductivity is a function of depth only
2-D	conductivity is a function of depth and one horizontal variable
3-D	conductivity is a function of depth and both horizontal variables
E	electric field (V/m)
H	magnetic field (A/m)
J	current density (A/m^2)
ω	angular frequency (rad/sec)
σ	conductivity (mhos/m)
σ_{ij}	tensor elements of conductivity tensor
ρ	resistivity, inverse of conductivity (ohm-m)
k_x, k_y	horizontal wavenumbers (rad/m)
k_z	vertical wavenumber (rad/m)
$\hat{z}, \hat{i}_z$	unit vectors in z direction
$\hat{x}, \hat{i}_x$	unit vetcors in x direction
$\hat{y}, \hat{i}_y$	unit vectors in y direction
ρ_a	apparent resistivity (ohm-m)
Z	impedance tensor (ohms)
Y	admittance tensor (mhos)

CHAPTER 1

1.1 Introduction

Low frequency electromagnetic waves generated by solar wind-magnetosphere interactions induce currents in a conductive earth (Jacobs, 1970). Fields produced by these currents in turn modify the total fields. The magnetotelluric (MT) method, first introduced by Cagniard (1953), involves measurement of the total electric and magnetic fields at the earth's surface. The total field variation at the surface is influenced by the subsurface conductivity. The MT method is used to map the conductivity structure. This structure is then combined with knowledge of the relationship between conductivity and geologic materials to infer geologic structure.

The MT method has been used to determine sedimentary basin structure (Vozoff, 1972), locate geothermal reservoirs (Morrison, et.al., 1979), delineate mineral deposits (Strangway, et.al., 1973), and study deep crustal structure (Swift, 1967). The targets of these surveys have all been three-dimensional bodies, while interpretation techniques until recently have been limited by one-dimensional or two-dimensional models (e.g. Swift, 1967, Laird and Bostick, 1970). Madden (1980) has shown that lower crustal resistivity may be severely underestimated when data around 3-D structures are interpreted using 1-D models. This problem

is especially prevalent in the Basin and Range Province of the western United States (e.g., Stanley, et. al., 1977 or Jiracek, et. al., 1979 for examples of such surveys).

Three-dimensional modelling poses severe computational problems. Asymptotic approximation and series expansion of the fields around 3-D structures were the two techniques commonly used before the advent of high-speed computers in the early 1970's. Kaufman and Keller (1981) provide an excellent review of these analytic solution methods.

Many different mathematical techniques have been applied to the numerical problem of modelling the electromagnetic response of 3-D structures. These techniques can be broadly classed into two methods-- the integral equation approach and the differential equation approach. Thin sheet approximations are used by researchers with both classes of methods.

The integral equation approach is the most common (e.g. Weidelt, 1975; Hohmann and Ting, 1978; Dawson and Weaver, 1979). Variations in conductivity are treated as equivalent current sources, and the fields are computed using dyadic Green's functions for a simple earth model. The integral equation methods have the advantage that they are computationally efficient for simple structures (Hohmann and Ting, 1978). This efficiency is lost, however, when modelling complicated conductivity distributions (Reddy, et. al., 1977).

The differential equation approach is the next most common method. This approach can be applied to complex structures , but most implementations are computationally inefficient. Finite differencing has been used (Lines and Jones, 1973), as has finite element modelling (Reddy, et.al., 1977). Hermance (1982) has used finite differencing modelling combined with approximating fields by their DC limits to model the MT response at very low frequencies. Ranganayaki and Madden (1980) use spectral methods (Orzag, 1972) applied to a thin, heterogeneous sheet. This approach seems the most efficient because the step size can be equal to the smallest scale length for conductivity variations.

Thin sheet approximations were introduced first by Price (1949). The region containing conductivity variations is thin compared to the electromagnetic skin depth in that region. The media on either side of the heterogeneous sheet may be homogeneous (Weidelt, 1975) or layered (Ranganayaki and Madden, 1980). Weidelt (1975) and Dawson and Weaver (1979) use thin layer approximations with their integral equation modelling approaches.

Our work presented here is an extension of Ranganayaki and Madden's (1980) generalized thin sheet approach. The original formulation of the problem allowed only one heterogeneous layer to be used. We have modified this formulation to allow us to stack heterogeneous layers.

1.2 Thesis Organization

We will examine four different topics concerning field behavior around 3-D structures. Chapter 2 contains the modification of the generalized thin sheet approach to allow stacking of heterogeneous layers. This is the forward modelling problem. We present several models to illustrate some key aspects of field behavior around 3-D structures. We also discuss whether fields around complicated structures obey the minimum phase assumption commonly used in data processing (Boehl, et.al., 1977).

Chapter 3 establishes the theoretical groundwork for a practical 3-D inversion scheme using the forward modelling method of Chapter 2. We use the generalized reciprocity theorem (Lanczos, 1956) to give us the field responses at the surface due to conductivity perturbations at depth. We show that our inversion scheme reduces to a linearized inversion method when applied to a 1-D model.

Chapter 4 is an analysis of MT data collected around a geothermal area at Beowawe, Nevada. The data are fit well with a 2-D structure. Considerations of possible 3-D effects, however, suggests that the 2-D structure need not be long in the strike direction.

Chapter 5 examines the problem of modelling effects from regional structure and local structure simultaneously. This problem has several different length scales--hence the name multiple scale analysis (Ranganayaki, 1978). The

results here are all negative, but shed considerable insight into the difficulties in the multiple scaling problem. We suggest a method which may bypass these difficulties.

'Ten years ago, we thought we knew a lot more about MT than we do today.'

M.G. Bloomquist

CHAPTER 2

2.1 Introduction

The 3-D modelling algorithm presented in this chapter consists of stacking thin heterogeneous layers over homogeneous layers of arbitrary thickness. We will present the extension of Ranganayaki's (1978) thin sheet analysis which allows us to stack these heterogeneous layers. Ranganayaki's work allowed the use of just one heterogeneous layer. We also discuss some of the important features of electromagnetic field behavior around 3-D bodies and show several models to illustrate these features. Finally, we show whether fields near 3-D bodies obey the minimum phase criterion used by Boehl, et. al. (1977). This assumption is important in data processing applications. Some of the material in this chapter has been published in Madden and Park (1982) and Park, et. al. (1983).

2.2 Thin Sheet Theory

Maxwell's equations, with a time dependence assumption of $\exp(-j\omega t)$ in all fields, are

$$\nabla \times E = j\omega\mu H \tag{2.2.1}$$

$$\nabla \times H = \sigma E - j\omega\varepsilon E \tag{2.2.2}$$

Conductivities within the earth range from .00001 mhos/m to 1 mho/m, and the magnetotelluric method uses low frequencies ($f \leq 100$ Hertz). The displacement current term in (2.2.2) is thus much smaller than the conduction current term and can be neglected.

The conductivity in (2.2.2) is a tensor conductivity. Its general form is

$$\sigma = \begin{bmatrix} \sigma_{xx} & \sigma_{xy} & \sigma_{xz} \\ \sigma_{yx} & \sigma_{yy} & \sigma_{yz} \\ \sigma_{zx} & \sigma_{zy} & \sigma_{zz} \end{bmatrix} \tag{2.2.3}$$

We assume that one of the principal axes of the medium is the z axis, but that the x and y axes are not necessarily principal axes. The conductivity tensor thus reduces to

$$\sigma = \begin{bmatrix} \sigma_{xx} & \sigma_{xy} & 0 \\ \sigma_{yx} & \sigma_{yy} & 0 \\ 0 & 0 & \sigma_{zz} \end{bmatrix} \tag{2.2.4}$$

The coordinate system and the model are shown in Figure 2.2.1.

We rewrite Maxwell's equations using the conductivity tensor in (2.2.4) so that we separate the horizontal and vertical components of the electric and magnetic fields in the curl operators. The new equations are

$$\partial E_S/\partial z=-j\omega\mu(\hat{i}_z\times H_S) + \nabla_S(E_z) \qquad (2.2.5)$$

$$\partial H_S/\partial z=-\hat{i}_z\times(\sigma_S E_S) + \nabla_S(H_z) \qquad (2.2.6)$$

$$H_z=(\nabla_S\times E_S)\cdot\hat{i}_z/(j\omega\mu) \qquad (2.2.7)$$

$$E_z=(\nabla_S\times H_S)\cdot\hat{i}_z/\sigma_{zz} \qquad (2.2.8)$$

where $\nabla_S=(\partial/\partial x,\ \partial/\partial y)$, $E_S=(E_x, E_y)$, $H_S=(H_x, H_y)$, $(\nabla_S\times F_S)\cdot\hat{i}_z=(\partial F_y/\partial x - \partial F_x/\partial y)$, and

$$\sigma_S=\begin{bmatrix}\sigma_{xx} & \sigma_{xy}\\ \sigma_{yx} & \sigma_{yy}\end{bmatrix}.$$

We want to eliminate E_z and H_z from the set of equations because we ultimately want only the horizontal fields. We substitute (2.2.7) into (2.2.6) and (2.2.8) into (2.2.5) to get

$$\partial E_S/\partial z=-j\omega\mu(\hat{i}_z\times H_S)+\nabla_S(\rho_{zz}(\nabla_S\times H_S)\cdot\hat{i}_z) \qquad (2.2.9)$$

$$\partial H_S/\partial z=-\hat{i}_z\times(\sigma_S F_S)+\nabla_S((\nabla_S\times E_S)\cdot\hat{i}_z/(j\omega\mu)) \qquad (2.2.10)$$

where $\rho_{zz}=1/\sigma_{zz}$. Equations (2.2.9) and (2.2.10) are the equations which govern the behavior of fields within a heterogeneous layer.

We have two types of derivatives in (2.2.9) and (2.2.10) - horizontal derivatives and vertical ones. The

vertical derivatives are approximated by finite differences. This approximation limits us to using small step sizes in the vertical direction-- hence the term 'thin sheet'. Both analytic and numerical error analyses indicate field errors of 10% or less occur when using vertical step sizes which are no larger than 20% of the horizontal step size (See Appendix A). The thickness:skin depth ratio must also be less than 0.5 for the fields to be accurate to within 10%.

The horizontal derivatives must be handled differently because we use a horizontal step size equal to the smallest scale length for conductivity variations. We assume the model repeats indefinitely in both the x and y directions. This repetition is illustrated in Figure 2.2.2. The conductivity variations, and thus the field variations, will have a wavenumber structure involving a finite number of wavenumbers. Horizontal derivatives are computed exactly using multiplication by wavenumbers in the wavenumber domain. Transformation between the space and wavenumber domains is efficiently achieved through the use of a 2-D fast Fourier transform (2-D because we have both x and y directions).

We now approximate the vertical derivatives with finite differences and derive upward continuation operators relating the fields at the bottom of a heterogeneous layer (H_s^-,E_s^-) with those at the top of the same layer (H_s^+,E_s^+).

The approximations to the vertical derivatives are

$$\frac{\partial E_S}{\partial z} \approx \frac{E_S^- - E_S^+}{\Delta z} \tag{2.2.11}$$

and

$$\frac{\partial H_S}{\partial z} \approx \frac{H_S^- - H_S^+}{\Delta z} \tag{2.2.12}$$

because we want an upward continuation operator, while the z axis is positive downward. We substitute (2.2.11) and (2.2.12) into (2.2.9) and (2.2.10), respectively, and rearrange the equations to get

$$E_S^+ = E_S^- + \Delta z\left[j\omega\mu(\hat{i}_z \times H_S^-) - \nabla_S(\rho_{zz}(\nabla_S \times H_S^-)\cdot\hat{i}_z)\right] \tag{2.2.13}$$

$$H_S^+ = H_S^- + \Delta z\left[\hat{i}_z \times (\sigma_S E_S^-) - \nabla_S((\nabla_S \times E_S^-)\cdot\hat{i}_z/(j\omega\mu))\right] \tag{2.2.14}$$

Note that we have approximated the fields within the layer with those at the bottom of the layer. We use continuity of tangential fields at the interfaces between layers. The surface fields at the top of a layer are thus identically equal to those at the bottom of the layer immediately above, and we have a way to continue fields between layers.

We use a technique similar to the method of Fourier analysis to solve for the fields at the surface of the earth. We first find all possible solutions to our problem (the stack of layers with (2.2.13) and (2.2.14) governing the field behavior) and then apply boundary and source

conditions at the surface of the earth. These conditions allow us to combine our set of all possible solutions into a single solution which satisfies our system of equations and all boundary and source conditions. The set of all possible solutions is finite because the fields anywhere can be represented by a finite number of wavenumber pairs (k_x, k_y).

The next step is to determine the set of all possible solutions. We assume the magnetic field at the bottom of the stack of heterogeneous layers, H_B, has the form of a pure exponential, $A \cdot \exp(jk_x'x+jk_y'y)$, where A is an arbitrary scalar constant. We apply an impedance boundary condition at the bottom of the stack of heterogeneous layers, so we know $E_B = ZH_B$. This tensor impedance, Z, is computed for each (k_x', k_y') wavenumber pair for the stack of homogeneous layers. This method (Ranganayaki, 1978) yields the impedance for a 1-D model for arbitrary horizontal wavenumbers. We then continue E_B and H_B up through the stack of heterogeneous layers to the earth's surface using (2.2.13) and (2.2.14). This continuation process is done twice for each unique wavenumber pair--once for

$$H_B = (A,0) \cdot \exp(\ldots)$$

and once for $H_B = (0,A') \cdot \exp(\ldots)$.

The electric and magnetic fields at the surface of the model will have a wavenumber structure reflecting: 1) the composite wavenumber structure of the conductivity distribution; and 2) the original wavenumber pair chosen for H_B.

The source is a current sheet at the surface of the earth (see Figure 2.2.3 for source configuration). A current sheet is used because it allows for the possibility of electromagnetic (EM) modelling and is necessary for the inverse problem later. We apply an admittance boundary condition to the fields above the current sheet to account for fields radiated back into the atmosphere. The relationship between the electric and magnetic fields in the air is governed by

$$\nabla \times E = j\omega\mu H \tag{2.2.15}$$

$$\nabla \times H = 0 \tag{2.2.16}$$

because $\sigma_{air} \approx 0$. Equations (2.2.15) and (2.2.16) are combined into a form $H_s^+ = Y_{air} \cdot E_s^+$ in the wavenumber domain where

$$Y_{air} = \frac{\begin{bmatrix} -k_x k_y & k_x^2 \\ -k_y^2 & k_x k_y \end{bmatrix}}{\omega\mu\sqrt{(j\omega^2\mu\varepsilon - k_x^2 - k_y^2)}} \tag{2.2.17}$$

The current sheet has zero thickness, so $E_s^- = E_s^+$. The magnetic field changes across the sheet, however. The

amount of change is given by

$$H_S^+ - H_S^- = \hat{i}_Z \times J_S \qquad (2.2.18)$$

We substitute in $H_S^+ = Y_{air} \cdot E_S^+$ and use the fact that $E_S^+ = E_S^-$ to get our surface condition (which combines both boundary and source conditions)

$$Y_{air} \cdot E_S^- - H_S^- = \hat{i}_Z \times J_S \qquad (2.2.19)$$

We know that E_S^- and H_S^- are some linear combination of the set of all possible solutions. The key is that the coefficients for E_S^- and H_S^- are the same set of constants we started with for H_B. We assume some H_B and an impedance relation to E_B, $E_B = Z_B H_B$. If we scale H_B by a scalar, A, then E_B is scaled by the same A because Z_B is linear. Equations (2.2.13) and (2.2.14) can be rewritten

$$E_S^+ = E_S^- + FH_S^- \qquad (2.2.20)$$

$$H_S^+ = H_S^- + GE_S^- \qquad (2.2.21)$$

where F and G are the linear operators in (2.2.13) and (2.2.14), respectively. Let us suppose we wish to continue the fields (AE_B, AH_B) at the bottom of a heterogeneous layer to the top (E_T, H_T). The fields at the top of the layer are

$$E_T = F_B + FH_B \qquad (2.2.22)$$

$$H_T = H_B + GE_B \qquad (2.2.23)$$

We substitute the scaled value of H_B and the expression for E_B into (2.2.22) and (2.2.23)

$$E_T = AZ_BH_B + AFH_B = A(E_B + FH_B) \qquad (2.2.24)$$

$$H_T = AH_B + AGZ_BH_B = A(H_B + GE_B) \qquad (2.2.25)$$

Notice that the fields at the top contain the same scalar constant, A, as the fields at the bottom. This
This coefficient is carried up through the heterogeneous structure without change because of the linearity of the operators. There is a unique, but undetermined, coefficient $A(k_x', k_y')$ for each trial value of H_B. The fields just below the current sheet can thus be written

$$E_S^- = \sum_{k_x'} \sum_{k_y'} A(k_x',k_y') \cdot E_S(k_x,k_y,k_x',k_y') \qquad (2.2.26)$$

$$H_S^- = \sum_{k_x'} \sum_{k_y'} A(k_x',k_y') \cdot H_S(k_x,k_y,k_x',k_y') \qquad (2.2.27)$$

We have used (k_x', k_y') to denote the original wavenumber pair chosen for H_B and (k_x, k_y) to denote the total wavenumber structure in the fields in (2.2.26) and (2.2.27). All wavenumber pairs will in general be present in the fields $E_S(k_x,k_y,k_x',k_y')$ and $H_S(k_x,k_y,k_x',k_y')$. We substi-

tute (2.2.26) and (2.2.27) into (2.2.18) to get a system of linear equations for the unknown coefficients, $A(k_x', k_y')$. Realizing that Y_{air} is a full operator with all wavenumber pairs present, the system is

$$\sum_{k_x'}' \sum_{k_y}' A(k_x', k_y') \left[\sum_{k_x} \sum_{k_y} \left(Y_{air}(k_x, k_y) E_s(k_x, k_y, k_x', k_y') - H_s(k_x, k_y, k_x', k_y') \right) \right] = i_z \times J_s \quad (2.2.28)$$

We choose a uniform current sheet in the x or y direction for a source and then solve for $A(k_x', k_y')$. These results are substituted back into (2.2.26) and (2.2.27) to compute the electric and magnetic fields at the surface.

Figure 2.2.1--Model with Coordinate System

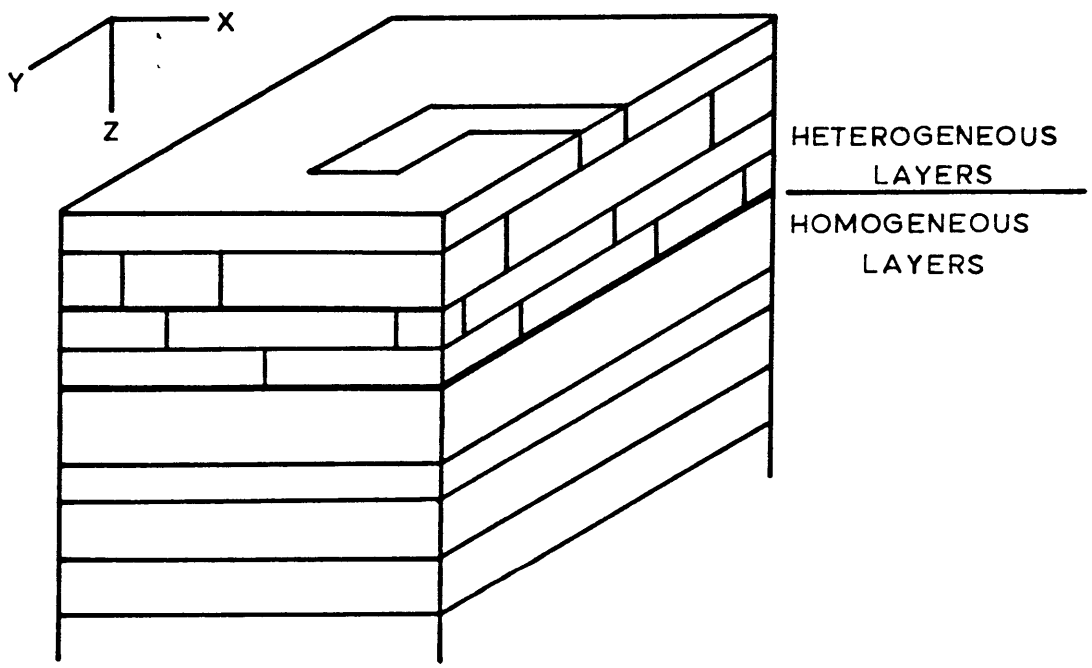


Figure 2.2.2-Repetition Assumption

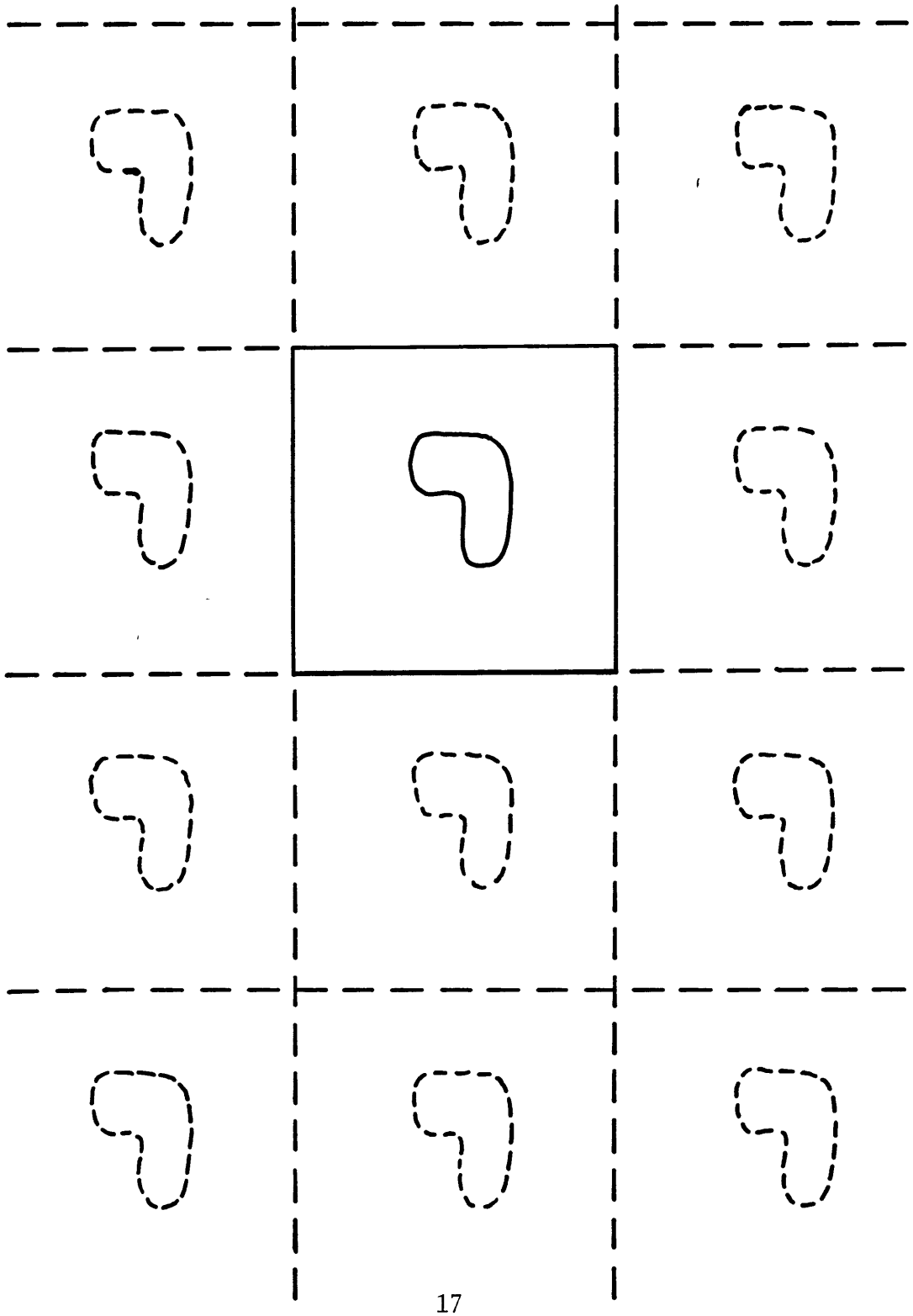
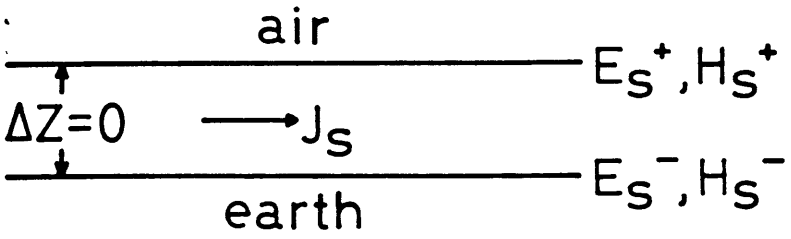


Figure 2.2.3--Source Condition



2.3 Three-Dimensional Field Behavior

We present MT sounding curves here for several 3-D models. These models have been chosen to illustrate certain aspects of field behavior around 3-D bodies. Large scale induction is responsible for regional electric fields. Mechanisms such as current gathering and local induction perturb these background fields near heterogeneities. These mechanisms produce different spatial and frequency behavior in the perturbed fields, so identification of the dominant effect is essential. Methods for estimating the contribution from each mechanism are presented in Appendix B. We use these methods to gain physical insight into why the fields behave the way they do. We also illustrate some pitfalls in the interpretation of MT data.

Magnetotelluric impedance tensors from the modelling program are rotated to their principal axes following the procedure outlined in Appendix C. Maximum and minimum apparent resistivities, phases, and rotation angles are computed. The rotation angles presented are measured with respect to the x axis (see Figure 2.3.1) and are positive in the clockwise direction. The rotation angle is the direction of maximum apparent resistivity. Three-dimensional structural indicators, the skew and ellipticity coefficients, are also presented. The skew and ellipticity are

$$SK = |(Z_{xx}'+Z_{yy}')/(Z_{xy}'-Z_{yx}')| \qquad (2.3.1)$$

$$EL = |(Z_{xx}'-Z_{yy}')/(Z_{xy}'+Z_{yx}')| \qquad (2.3.2)$$

if the rotated tensor is given by

$$Z' = \begin{bmatrix} Z_{xx}' & Z_{xy}' \\ Z_{yx}' & Z_{yy}' \end{bmatrix} \qquad (2.3.3)$$

The model results are presented in the following format: first, a map and cross-section for each model; and then sounding curves for each site. Apparent resistivities, phases, rotation angles, skews, and ellipticities are plotted for each site. A location map is provided in the upper right corner of the apparent resistivity plot. This map shows the site location with respect to the heterogeneity. The corresponding 1-D curve is plotted at each site. This is a sounding curve computed assuming the structure directly beneath the site extends laterally to infinity. We will use compass directions when discussing features of the models. East is the x axis, and south is the y axis in Figure 2.3.1. Each model consists of 4 to 7 heterogeneous layers over a halfspace with laterally homogeneous layers.

The first effect we discuss is only seen at the higher frequencies when the thickness of the heterogeneous region is larger than the skin depth. This effect is the insensitivity of fields to heterogeneities more than a few

electromagnetic skin depths away. This statement is not strictly true if anisotropic material is present, and this exception will be discussed later. The second effect is the ability of the conductive heterogeneity to gather current both laterally and vertically. A way of estimating vertical and horizontal current gathering is discussed in Appendix B, and is used here. The final effect we consider is local induction. These last two effects are seen at low frequencies where the skin depth is much larger that the thickness of the heterogeneous region.

High Frequency Insensitivity to Distant Heterogeneities

The first effect is seen at all the sites in Figures 2.3.2-2.3.5. The MT sounding curves and the local 1-D sounding curves merge at frequencies above 0.1 Hz in Figures 2.3.4 and 2.3.5. The skin depth within the heterogeneity is 5 km at 0.1 Hz. The nearest boundary is 25 km, or 5 skin depths, from the MT sites (which lie at the centers of the blocks). The secondary fields due to interactions with the boundary have decayed to a negligible fraction of the primary 1-D fields at these sites, so the structure 'sensed' is essentially one-dimensional above 0.1 Hz. This same effect can be seen in Figures 2.3.2 and 2.3.3 for sites outside the heterogeneity, but the sounding curves merge with the 1-D curves above 0.5 Hz. The skin depth at 0.5 Hz outside the conductive feature is 14 km., so the nearest boundary is about 1.5 skin depths away.

Current Gathering

Current gathering effects are seen below 0.01 Hz at the sites shown in Figures 2.3.2 - 2.3.5. Table 2.3.1 summarizes the relative contributions of the different mechanisms at 0.01 Hz both inside and outside the heterogeneity in Figure 2.3.1. We see that vertical current flow is the dominant mechanism within the conductor and equally important to horizontal current flow without. Local induction plays virtually no role in this first model. Ranganayaki and Madden (1980) have shown that variations in electric field strength due to vertical current flow are frequency-independent when the thickness of the heterogeneous region is much smaller than the skin depth. The amount of variation is only a function of position at low frequencies. The skin depths inside and outside the heterogeneity at 0.01 Hz are 16 km and 100 km , respectively. The thickness of the conductive feature is only 1 km, so variations in the apparent resistivity should be frequency-independent below 0.01 Hz. The change in electric field due to horizontal current gathering is also assumed to be frequency-independent at these low frequencies.

The current gathering effects seen at all sites (Figures 2.3.2-2.3.5) appear as parallel offsets of the sounding curves from the low frequency portions of the corresponding 1-D curves. The variation of apparent

resistivity, proportional to $(E/H)^2$, is a direct result of electric field strength variations. This correlation occurs because the secondary magnetic field is only a few percent of the source field. We have never seen a secondary field strength of more than 30% of the primary field in any of our test models.

Adjustment Distance

A parameter used to estimate the effect of the vertical current gathering is the 'adjustment distance'. The adjustment distance is the horizontal distance over which a surface conductor gathers enough current to decrease the current level perturbation to 1/e of its value at the boundary. This distance is a measure of how far away fields are perturbed by a heterogeneity, and is given by

$$D_A = \sqrt{[(\sigma \cdot \Delta Z1) \cdot (\rho \cdot \Delta Z2)]} \qquad (2.3.4)$$

where $(\sigma \cdot \Delta Z1)$ is the conductivity-thickness product for the conductive surface layer, and $(\rho \cdot \Delta Z2)$ is the integrated resistance of the resistive subsurface layers (Ranganayaki and Madden, 1980). The adjustment distance is a measure of how easily a surface conductor gathers vertical current, even though it is a measure of horizontal distance.

A good example of the adjustment distance effect is shown by comparison of the models shown in Figures 2.3.1 and 2.3.6. These models are identical, except that the 10000 Ω-m layer in Figure 2.3.1 is reduced to 1000 Ω-m in Figure 2.3.6.

The adjustment distance inside the conductive body thus changes from 191 km to 136 km. Table 2.3.1 again shows us vertical current is the dominant mechanism inside the feature. Comparison of Figures 2.3.4 and 2.3.5 to Figures 2.3.9 and 2.3.10, respectively, shows that the fields inside are higher for the conductor with the smaller adjustment distance. More vertical current has been gathered by the model in Figure 2.3.6 than in Figure 2.3.1.

The frequency-independent nature of the adjustment distance effect at low frequencies appears as parallel offsets in the sounding curves. The shape of the curve, however, is dictated by the structure beneath the heterogeneous layer. This structure is homogeneous in our models, so the low frequency portions of the sounding curves in Figures 2.3.4 and 2.3.5 resemble the outside 1-D curve. However, the inflection points seen near 0.1 Hz in the MT curves at sites 32 and 50 are no longer due to deep structure as in the 1-D case, but are rather due to surface heterogeneities. The resistivity contrast, thickness, and lateral extent of the heterogeneity control both the amount of shift and at what frequency the curves begin to merge with the inside 1-D curve. The net result is a set of sounding curves which merge with the local 1-D curve at high frequencies and resemble a shifted version of the outside 1-D curve at low frequencies.

Horizontal Current Gathering

Horizontal current gathering plays a role in the field behavior outside the heterogeneity. The mechanism is wholly responsible for field perturbations in the model in Figure 2.3.6 and is equally responsible in Figure 2.3.1. Comparison of Figures 2.3.2 and 2.3.7 shows that the enhancement of the maximum apparent resistivities and the reduction of the minimum apparent resistivities below 0.01 Hz are the same for both models. The adjustment distances outside for Figures 2.3.2 and 2.3.7 are 30 km and 22 km, respectively, so the sites are many e-folds away from the heterogeneity. The fields, however, are still substantially perturbed. This perturbation is due to horizontal current gathering. The similarity in offset for these two models with different adjustment distances supports this conclusion. The changes made in the model do not affect this mechanism. The effects seen in Figures 2.3.2 and 2.3.7 are twice the actual effects because of the repetition assumption we discussed in the previous section. The modelling algorithm assumes the conductive feature is repeated to the north, putting site 5 almost equidistant between the heterogeneity and its image. The effects of the image in Figure 2.3.3 are negligible because of the proximity of site 23 to the heterogeneity.

Local Induction

The first two models presented illustrate horizontal and vertical current gathering. The model in Figure 2.3.11

has been chosen because local induction is the dominant mechanism within the conductive body (see Tables 2.3.1 and 2.3.2). Examination of the inside apparent resistivity curves below 0.01 Hz shows that the curves in Figures 2.3.14 and 2.3.15 are not simply shifted versions of the outside 1-D curve (see Figure 2.3.12). Comparison of the inside estimates given in Tables 2.3.1 and 2.3.2 shows that, while the induction estimates are approximately equal for the N-S and E-W directions, the current gathering is much more important in the N-S direction. Current gathering and induction are of equal importance in the N-S direction, but the latter is more important in the E-W directon. The maximum curves, aligned N-S are thus much closer in slope to the outside 1-D curve than are the minimum curves. We see a much steeper slope on the minimum apparent resistivity curves in Figures 2.3.14 and 2.3.15. The slope expected from local induction effects would be 1 (Appendix B), so the slopes seen confirm that local induction is important.

Horizontal current gathering occurs outside the conductive body in this model (Table 2.3.1). We see effects from this mechanism in Figures 2.3.12 and 2.3.13. The maximum apparent resistivity curves, aligned N-S, show current enhancement compared to the 1-D curve. The minimum curves are much closer to the 1-D curve.

Apparent Isotropy

We infer from the almost isotropic character of the sounding curves in Figures 2.3.4 and 2.3.9 that these sites lie over a laterally homogeneous earth. The usual interpretation approach would be to invert these data assuming a 1-D model. Comparison of the local 1-D curves to the sounding curves in these figures shows that the derived resistivity structure would be quite erroneous in its estimates of the intermediate and deep resistivity structure. This problem arises because the sites in these figures lie at points of approximate symmetry for the heterogeneous structure. Isotropic-looking sounding curves may not be free of 3-D structural effects.

Conductor Interactions

Figure 2.3.16 illustrates a model with a thin, surface conductor and a deeper, thicker conductor. We present two sets of curves for this model--one with the shallow conductor and one without it. We use these curves to discuss how surficial heterogeneity affects MT sounding curves. We begin by computing the adjustment distance for the surface conductor.

The adjustment distance must be calculated using only the resistive layers between the feature and the nearest current sources. The shallower conductor can attract sufficient current from the deeper feature to raise current

levels at sites directly above the buried conductor. The mantle thus plays no role in this case. The adjustment distance for the shallow feature is determined using only the resistive layers between the two heterogeneities, and is 0.7 km. Every site over the deeper feature is thus at least 18 e-folds away from the nearest boundary.

The insensitivity of fields to heterogeneities more than a few skin depths away can be affected by anisotropic material. The adjustment distance for the shallow conductor is a good example of this. If the surface layers are highly anisotropic, then the adjustment distance could be larger than 0.7 km. The top layer is thin enough that the skin depth is much larger than its thickness up to frequencies of 10 Hz (the skin depth is 0.5 km inside). The thin sheet approximation, and its associated adjustment distance, is therefore valid up to this frequency. All boundaries are thus several skin depths away at these frequencies, but the surface heterogeneity could still affect the sounding curves if the adjustment distance was several kilometers long. This example again shows the importance of the adjustment distance.

Figures 2.3.17 and 2.3.18 show sounding curves for site 22 with and without the surface feature, respectively. These curves are identical. The surface conductor exhibits no influence upon the data at site 22. We infer from this

observation that both vertical and horizontal current gathering mechanisms are negligible outside the shallow conductor. Figures 2.3.19 and 2.3.20 are sounding curves for site 43 with and without the surface feature, respectively. The curves in Figure 2.3.19 are slightly lower than those in Figure 2.3.20, but the change is only 3% in the electric fields. Enough current has been drawn up from the deeper conductor to virtually compensate for the shallow feature in this case.

Sites not over the deeper feature exhibit different behavior, however. Figures 2.3.21 and 2.3.22 are used to compare sounding curves for site 44 with and without the surface conductor, respectively. The shallow feature decreases the electric field strength by about 10% (20% for apparent resistivities) at site 44. This decrease is frequency-independent at low frequencies, suggesting vertical current gathering. The adjustment distance here is larger than the 0.7 km we derived for the body earlier. The absence of the buried conductor beneath the site means vertical current must be gathered from deeper structures. The crust is conductive enough so that the conductance of the upper 500m (500*.01=5 mhos) is equal to that of the top layer (50*0.1=5 mhos). Hence, the body can gather current vertically from the layers immediately beneath it.

Summary

We have presented some insights into field behavior around 3-D structures in this section. The implications of vertical versus horizontal current gathering, and local induction must be considered when interpreting MT sounding curves. Each mechanism influences the sounding curves differently, and thus the dominant mechanism must be identified. We have also presented some examples of pitfalls in MT interpretation. Isotropic-looking sounding curves are not always due to 1-D structure. Effects on MT curves from variations in surficial conductivity are dependent upon the structure beneath the surface layer.

Table 2.3.1--N-S Field Contribution Estimates for 100 Second Periods

Electric Field Estimates Inside Heterogeneity
(Location at center of heterogeneity)

Model	Vertical Current Gathering	Horizontal Current Gathering	Local Induction
Fig. 2.3.1	1.0×10^{-3} 141°	2.6×10^{-4} 111°	2.0×10^{-5} 87°
	(Background* electric field= 9.8×10^{-5} 111°)		
Fig. 2.3.6	1.9×10^{-3} 143°	2.5×10^{-4} 116°	2.2×10^{-5} 83°
	(Background electric field= 9.3×10^{-5} 116°)		
Fig. 2.3.11	2.3×10^{-5} 159°	4.4×10^{-5} 115°	7.5×10^{-5} 97°
	(Background electric field= 1.5×10^{-5} 114°)		
Fig. 2.3.16	8.5×10^{-4} 142°	1.1×10^{-4} 113°	2.2×10^{-5} 87°
	(Background electric field= 9.5×10^{-5} 115°)		

Electric Field Estimates Outside Heterogeneity
(Location is 1.5 block lengths south of heterogeneity)

Model	Vertical Current Gathering	Horizontal Current Gathering	Local Induction
Fig. 2.3.1	4.7×10^{-4} 141°	2.5×10^{-4} 111°	--
	(Background* electric field= 3.9×10^{-3} 111°)		
Fig. 2.3.6	10^{-8}	2.4×10^{-4} 116°	--
	(Background electric field= 3.7×10^{-3} 116°)		
Fig. 2.3.11	1.4×10^{-4} 160°	4.4×10^{-3} 114°	--
	(Background electric field= 1.5×10^{-3} 114°)		
Fig. 2.3.16	4.5×10^{-4} 142°	9.1×10^{-4} 115°	--
	(Background electric field= 3.8×10^{-3} 115°)		

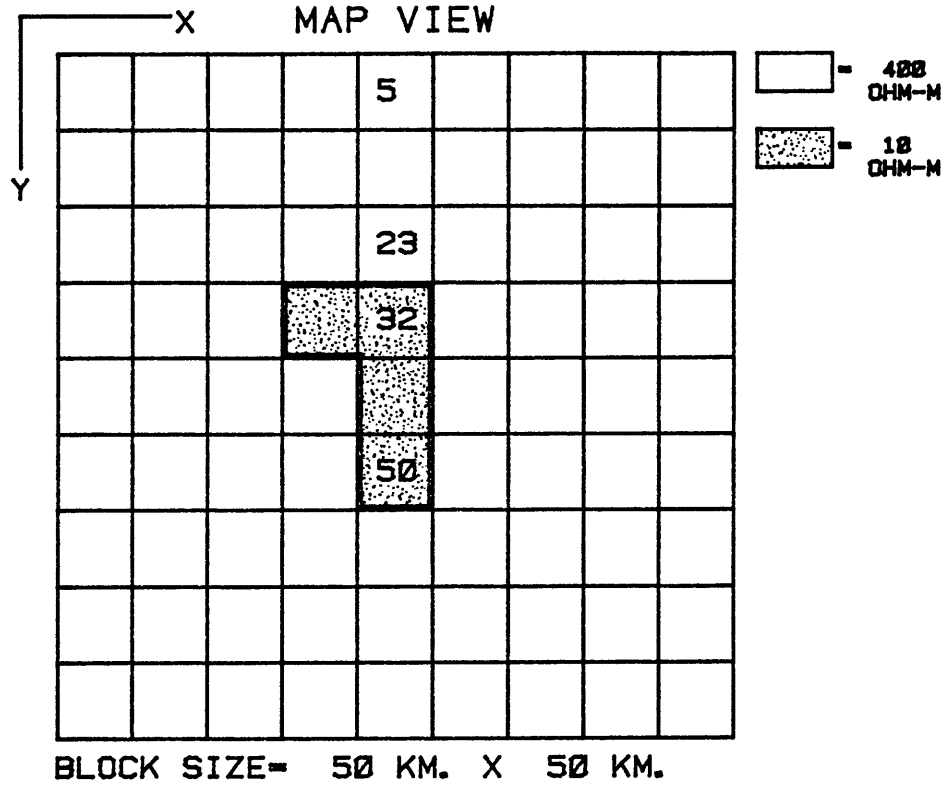
Background field inside=(σ_2/σ_1)(1-D field outside)
Background field outside= 1-D field outside

Table 2.3.2--E-W Field Contribution Estimates for 100 Second Periods

Electric Field Estimates Inside Heterogeneity
(Location at center of heterogeneity)

Model	Vertical Current Gathering	Horizontal Current Gathering	Local Induction
Fig. 2.3.1	4.1×10^{-4} 141°	3.1×10^{-5} 111°	2.0×10^{-5} 90°
	(Background electric field= 9.8×10^{-5} 111°)		
Fig. 2.3.6	1.0×10^{-3} 143°	3.0×10^{-5} 116°	2.0×10^{-5} 91°
	(Background electric field= 9.3×10^{-5} 116°)		
Fig. 2.3.11	8.2×10^{-6} 159°	5.0×10^{-6} 114°	8.0×10^{-5} 91°
	(Background electric field= 1.5×10^{-5} 114°)		
Fig. 2.3.16	7.3×10^{-4} 142°	7.3×10^{-5} 115°	2.1×10^{-5} 88°
	(Background electric field= 9.5×10^{-5} 115°)		

Figure 2.3.1--Current Gathering--Model 1



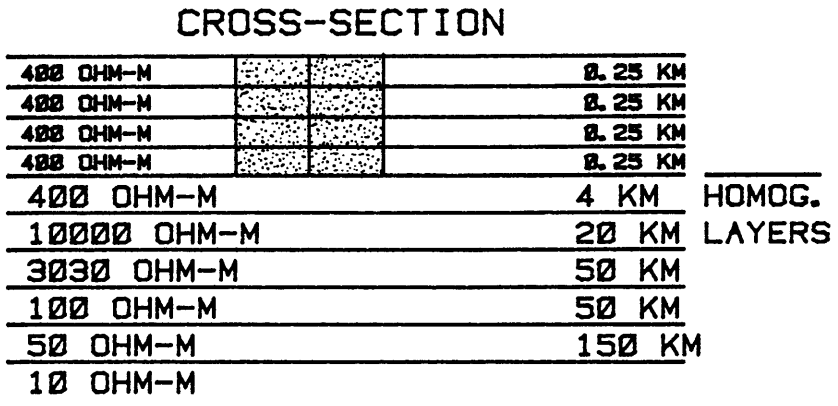


Figure 2.3.2--Site 5--Model 1

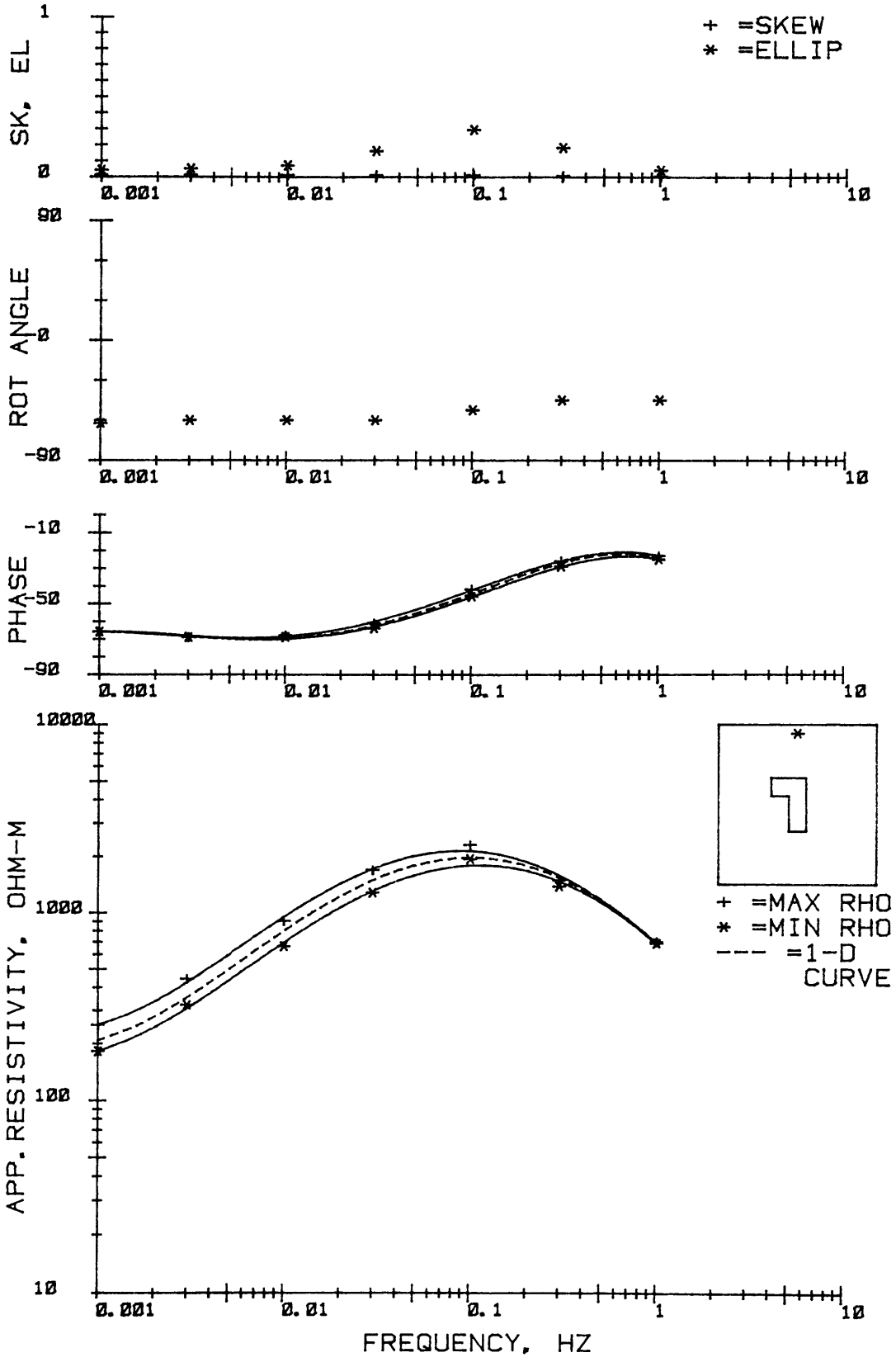


Figure 2.3.3--Site 23--Model 1

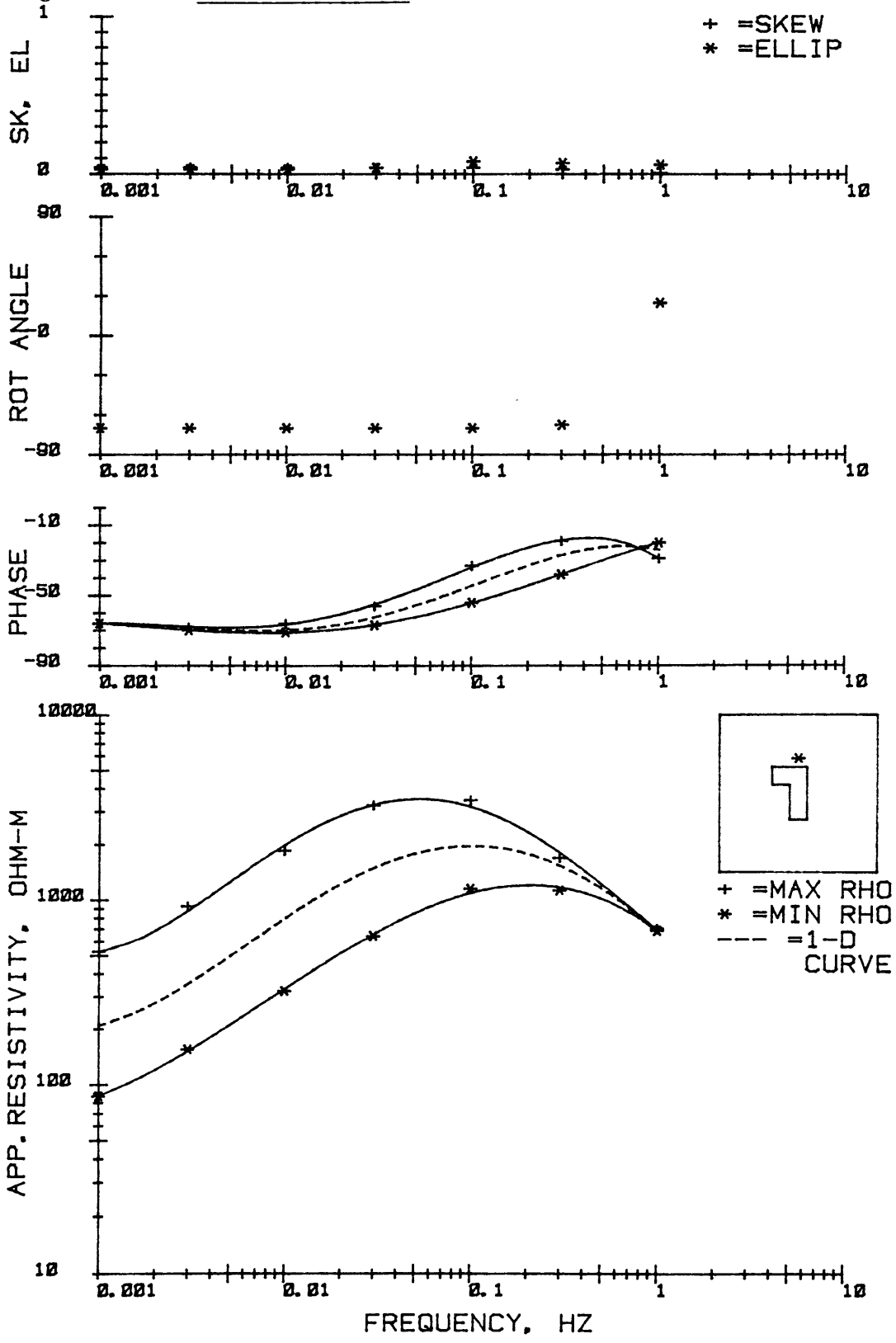


Figure 2.3.4--Site 32--Model 1

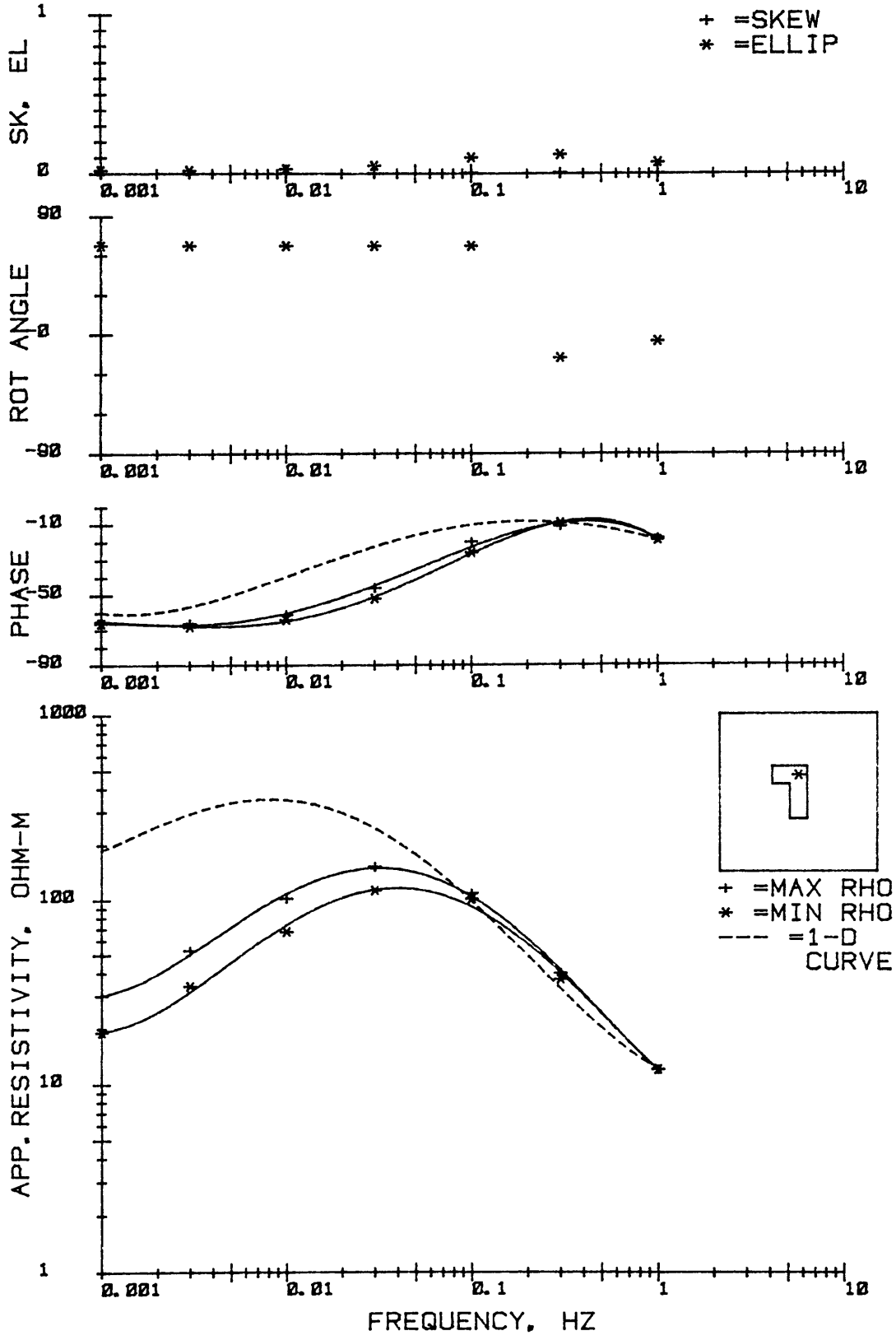


Figure 2.3.5--Site 50--Model 1

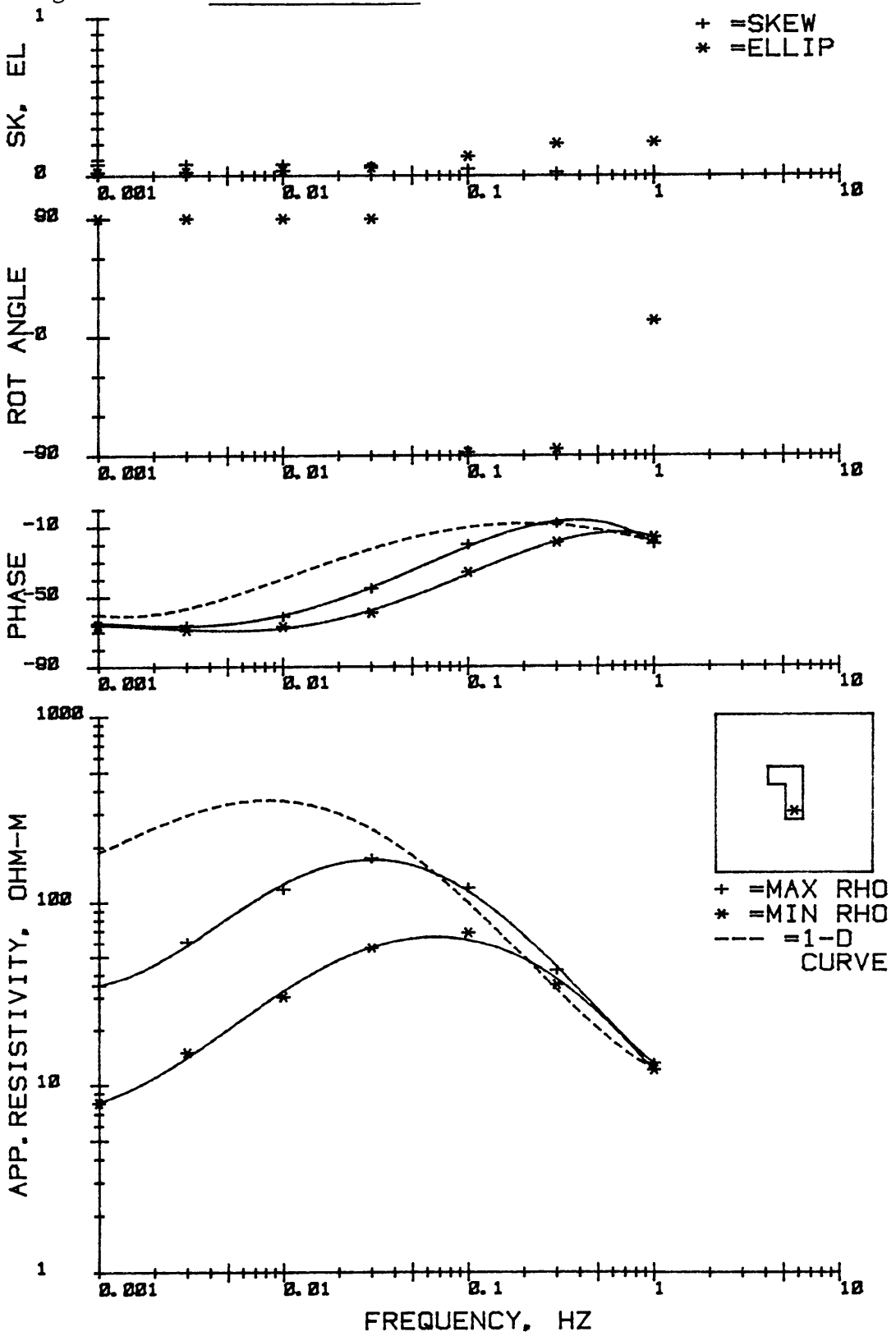
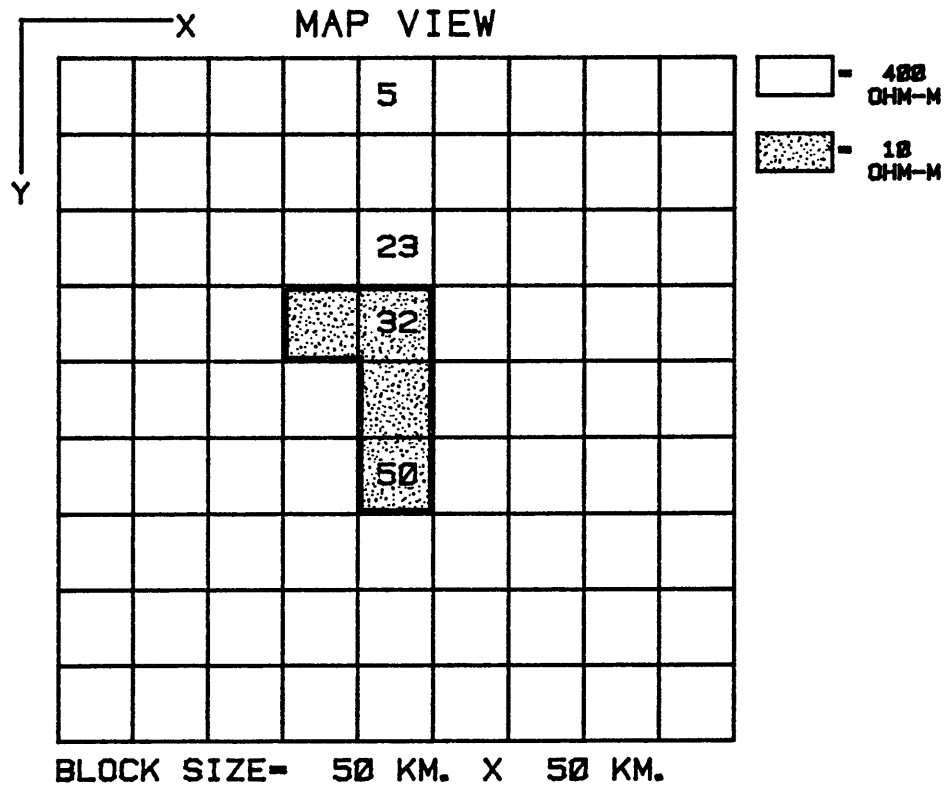


Figure 2.3.6--Current Gathering--Model 2



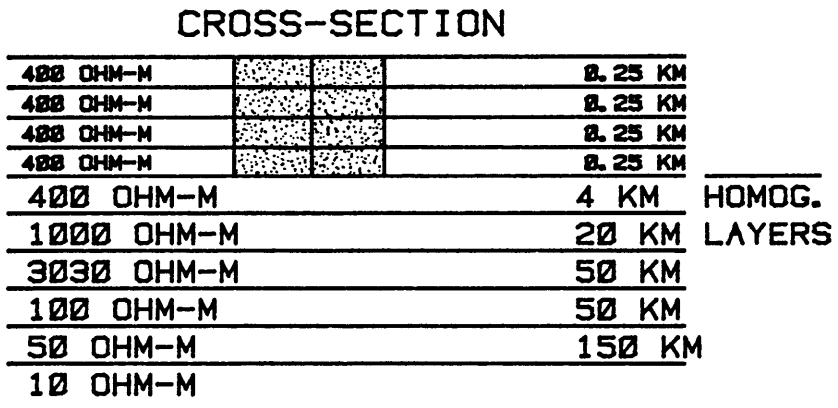


Figure 2.3.7--Site 5--Model 2

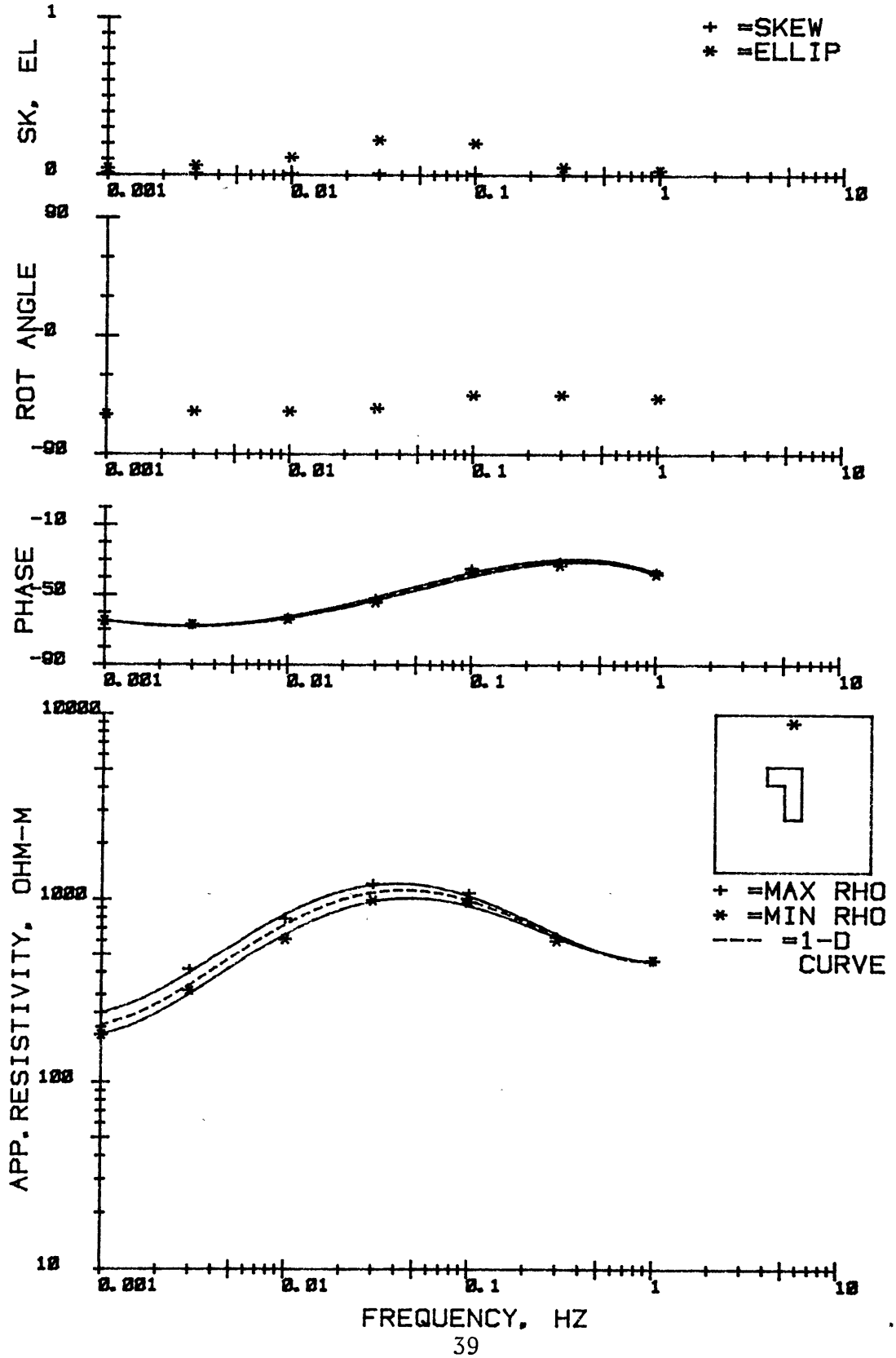


Figure 2.3.8--Site 23--Model 2

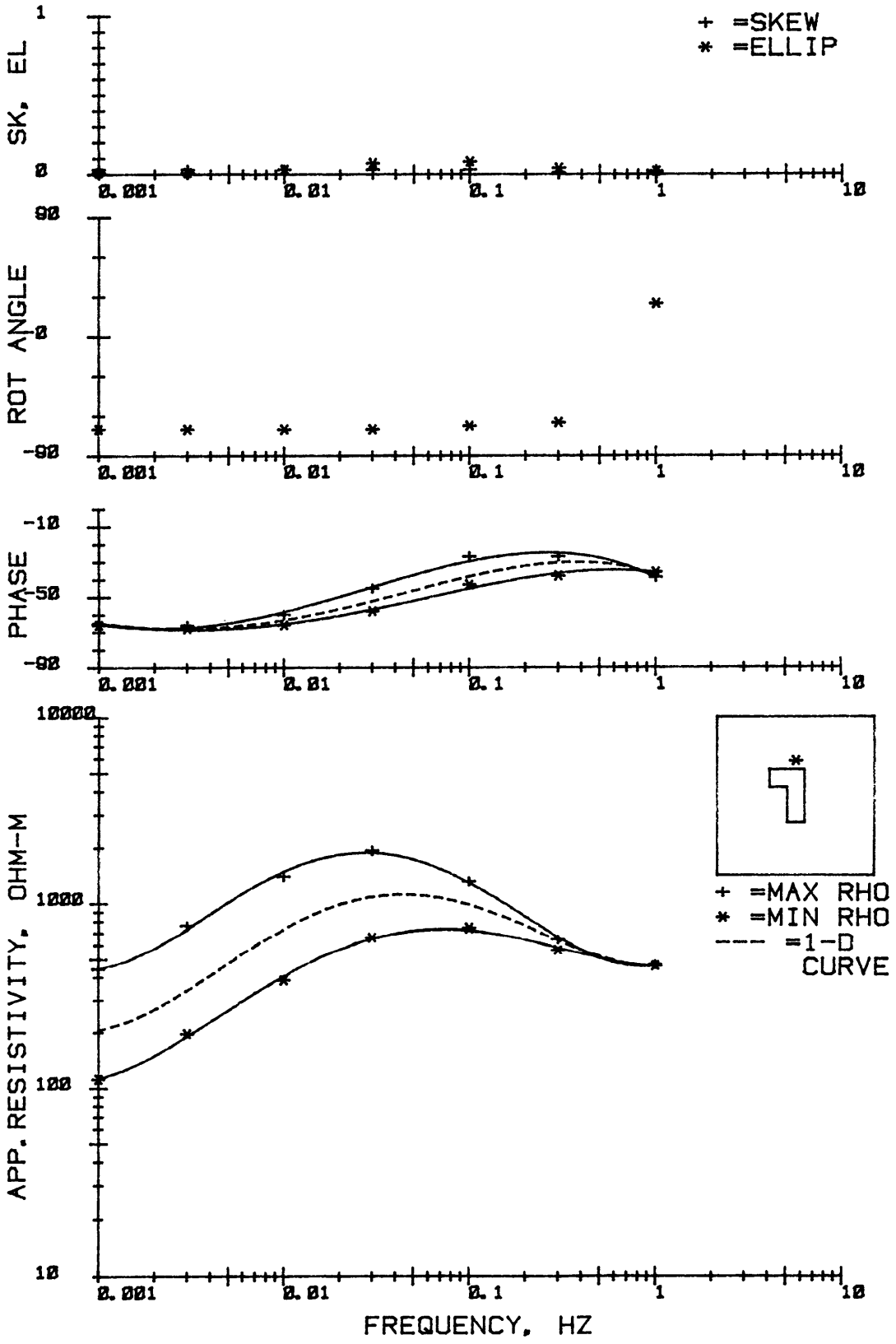


Figure 2.3.9--Site 32--Model 2

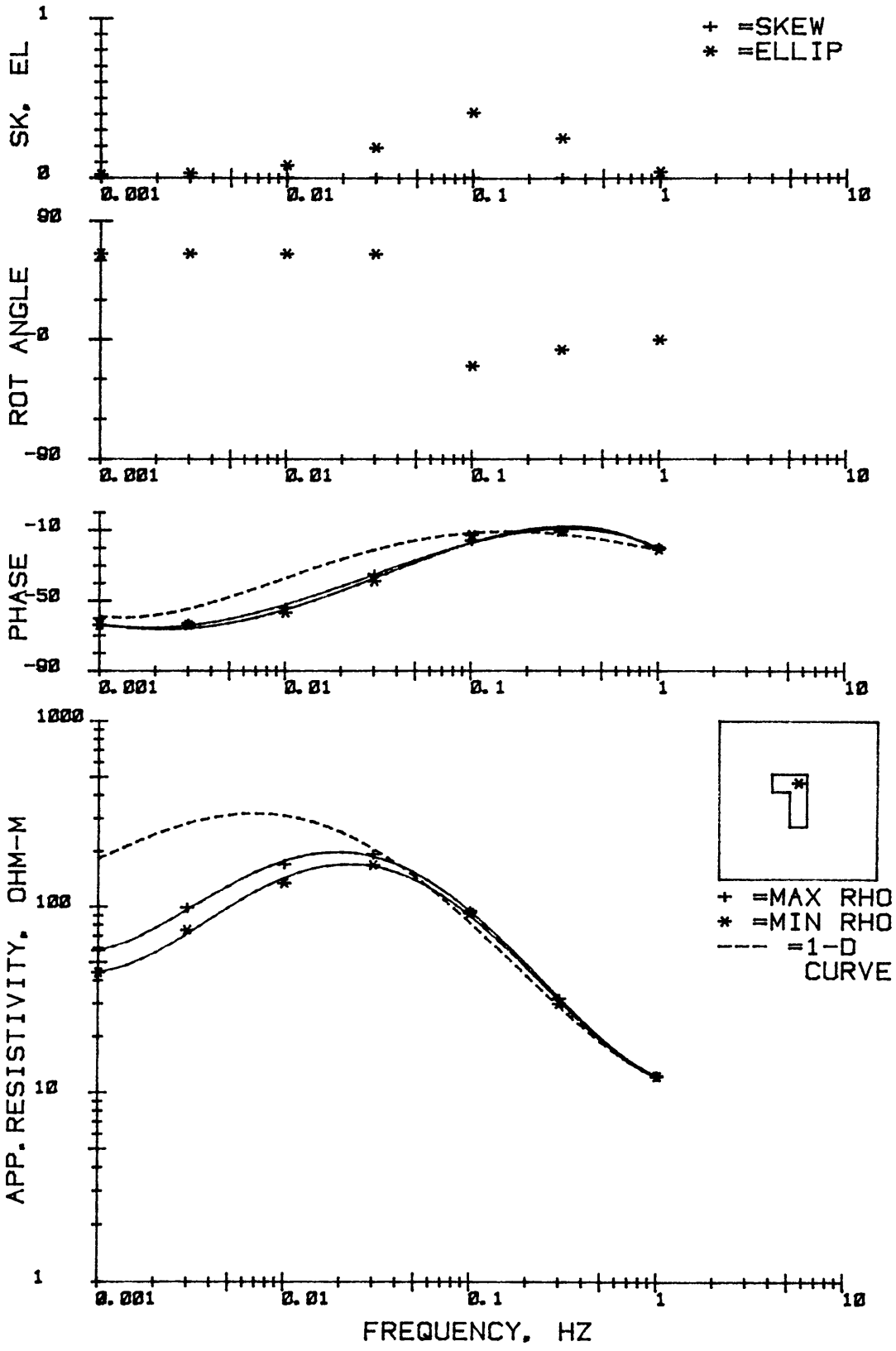


Figure 2.3.10--Site 50--Model 2

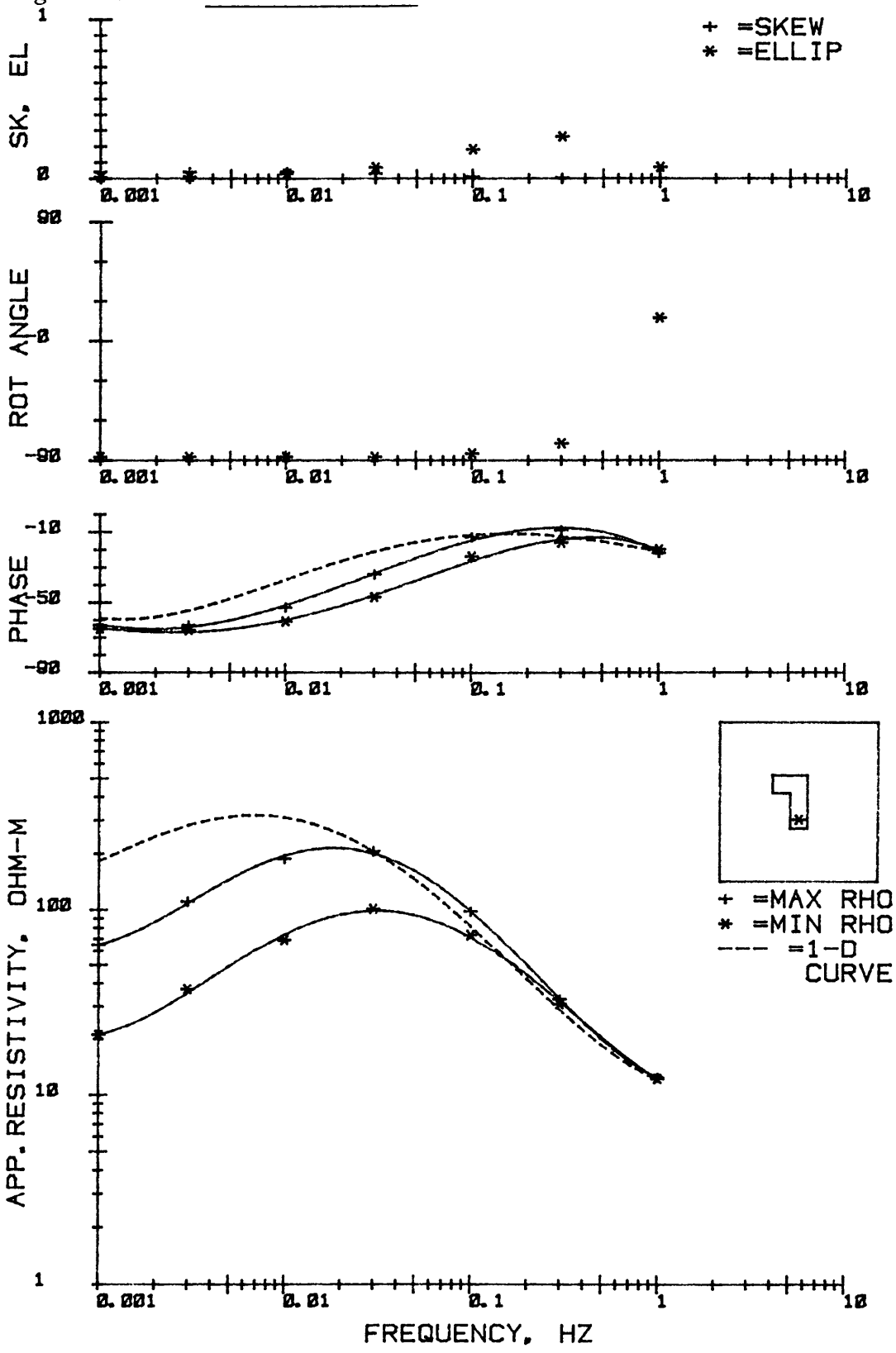


Figure 2.3.11--Induction--Model 3

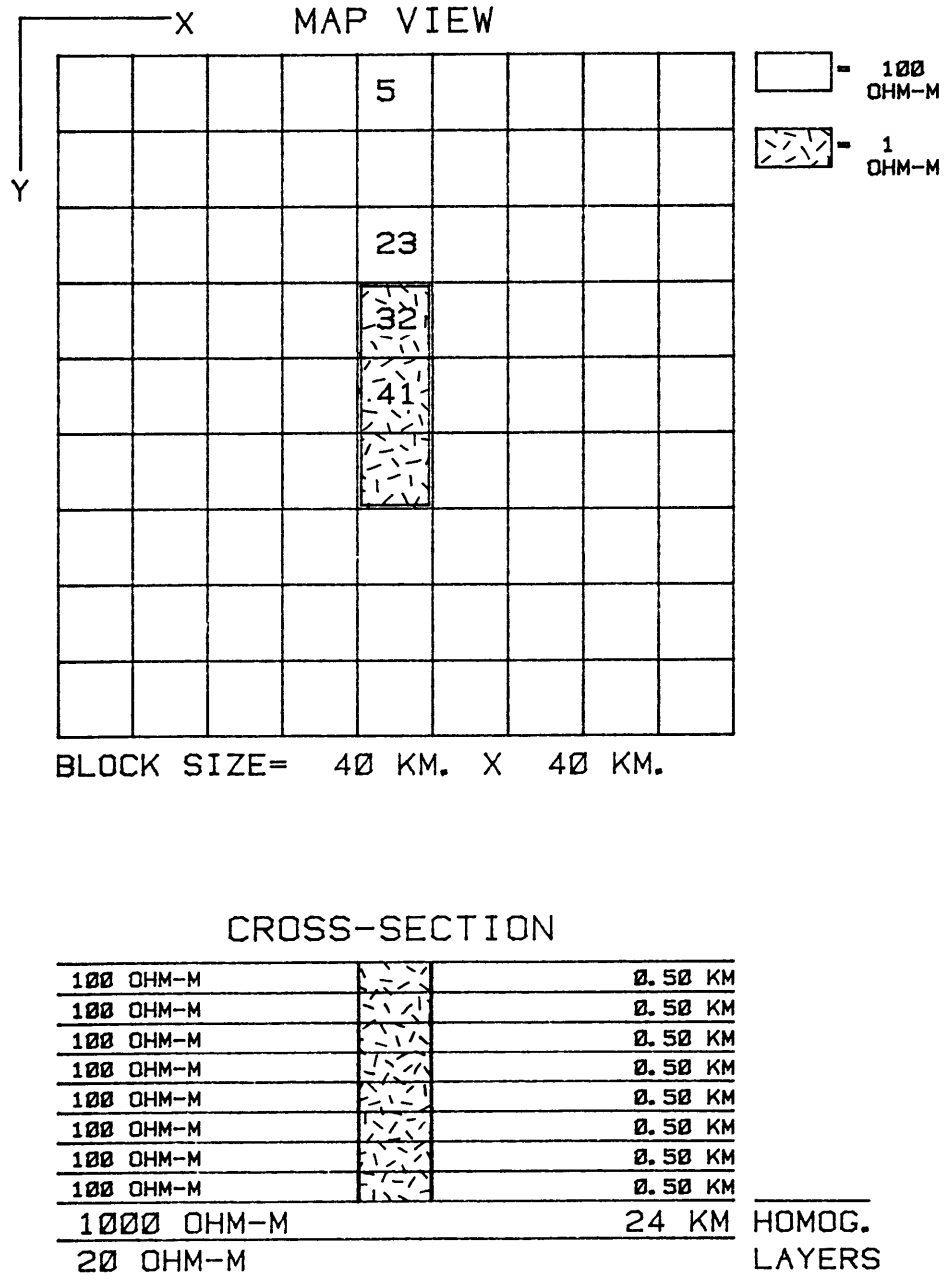


Figure 2.3.12--Site 5--Model 3

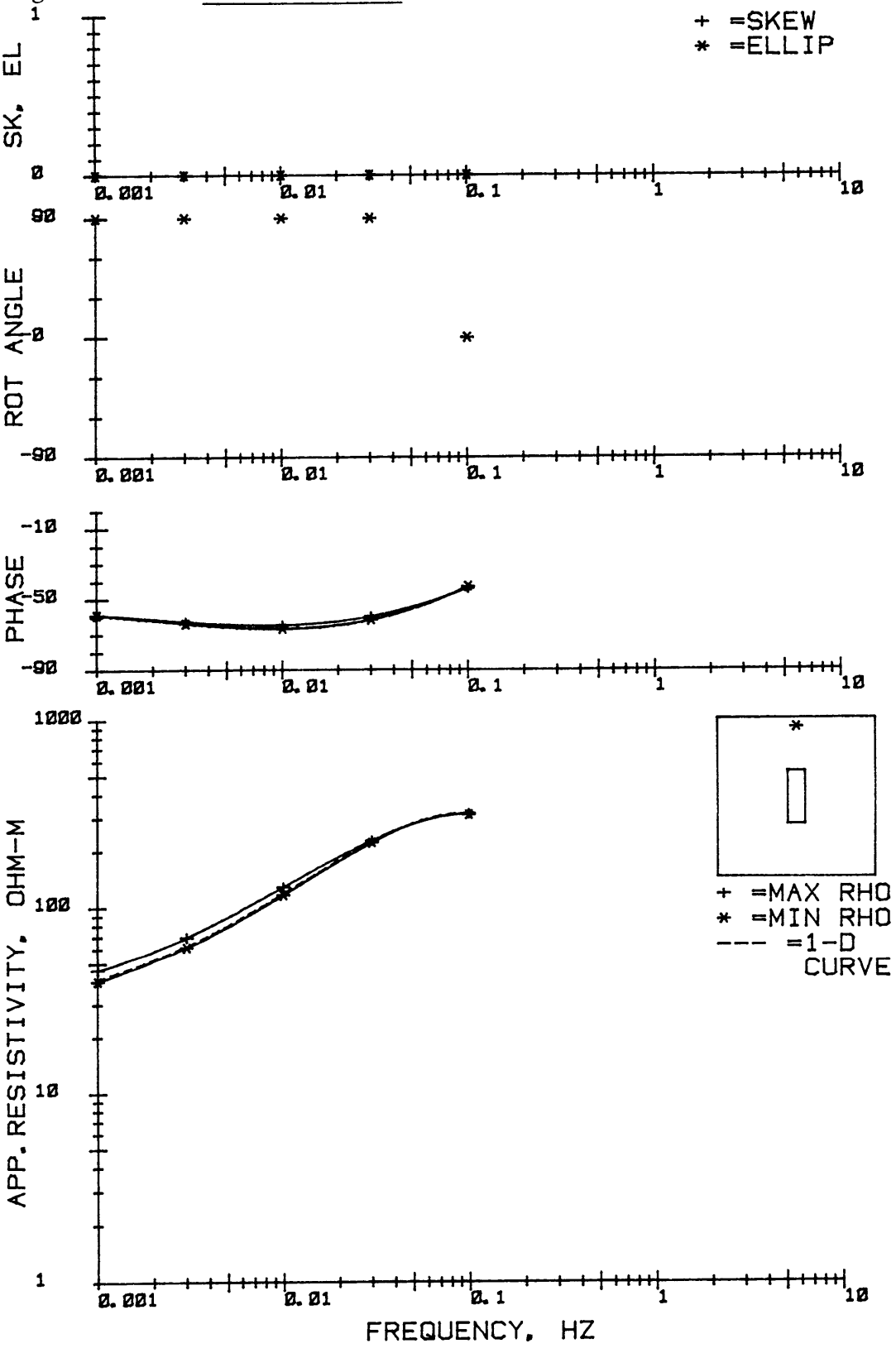


Figure 2.3.13--Site 5--Model 3

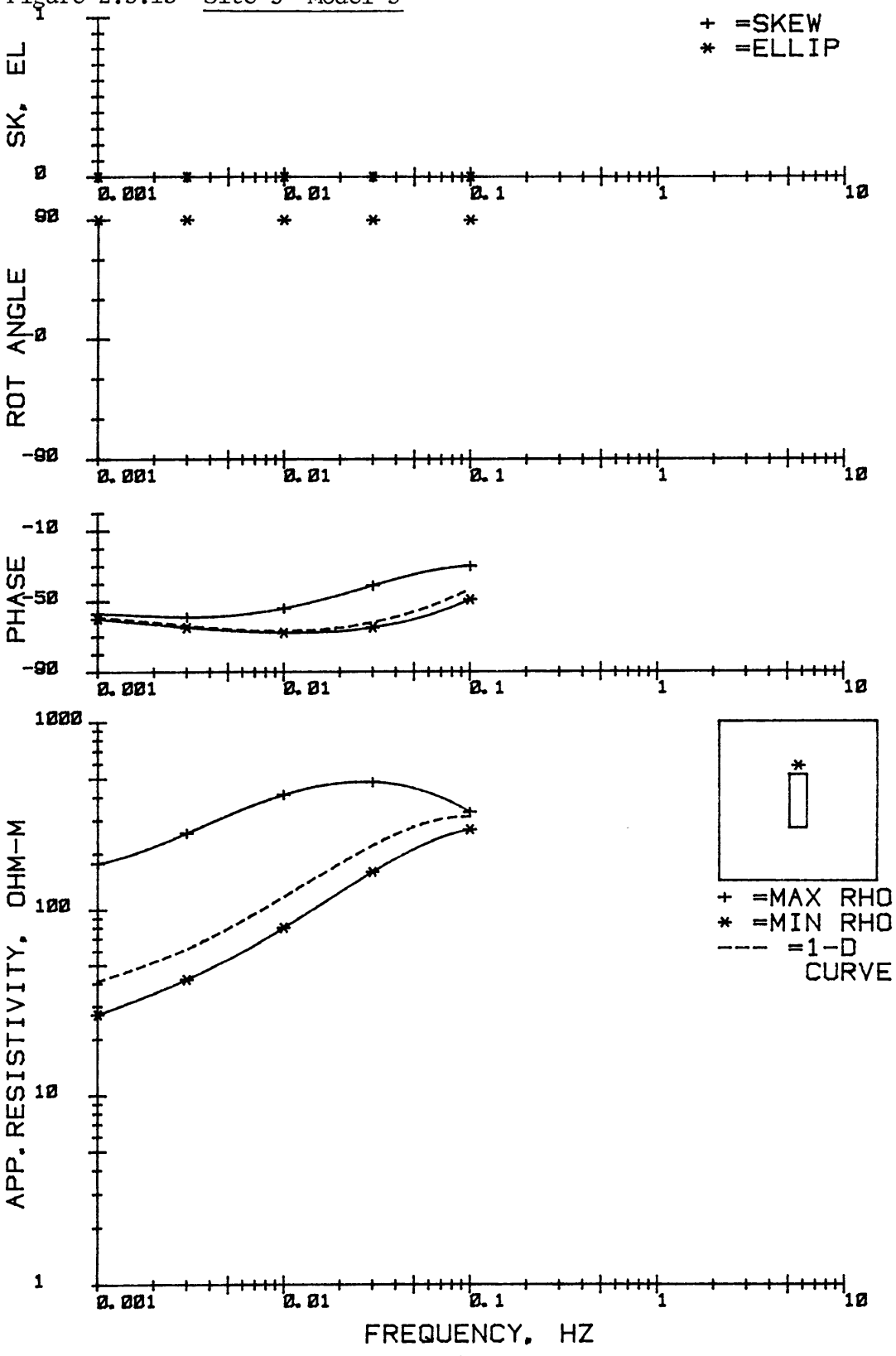


Figure 2.3.14--Site 32--Model 3

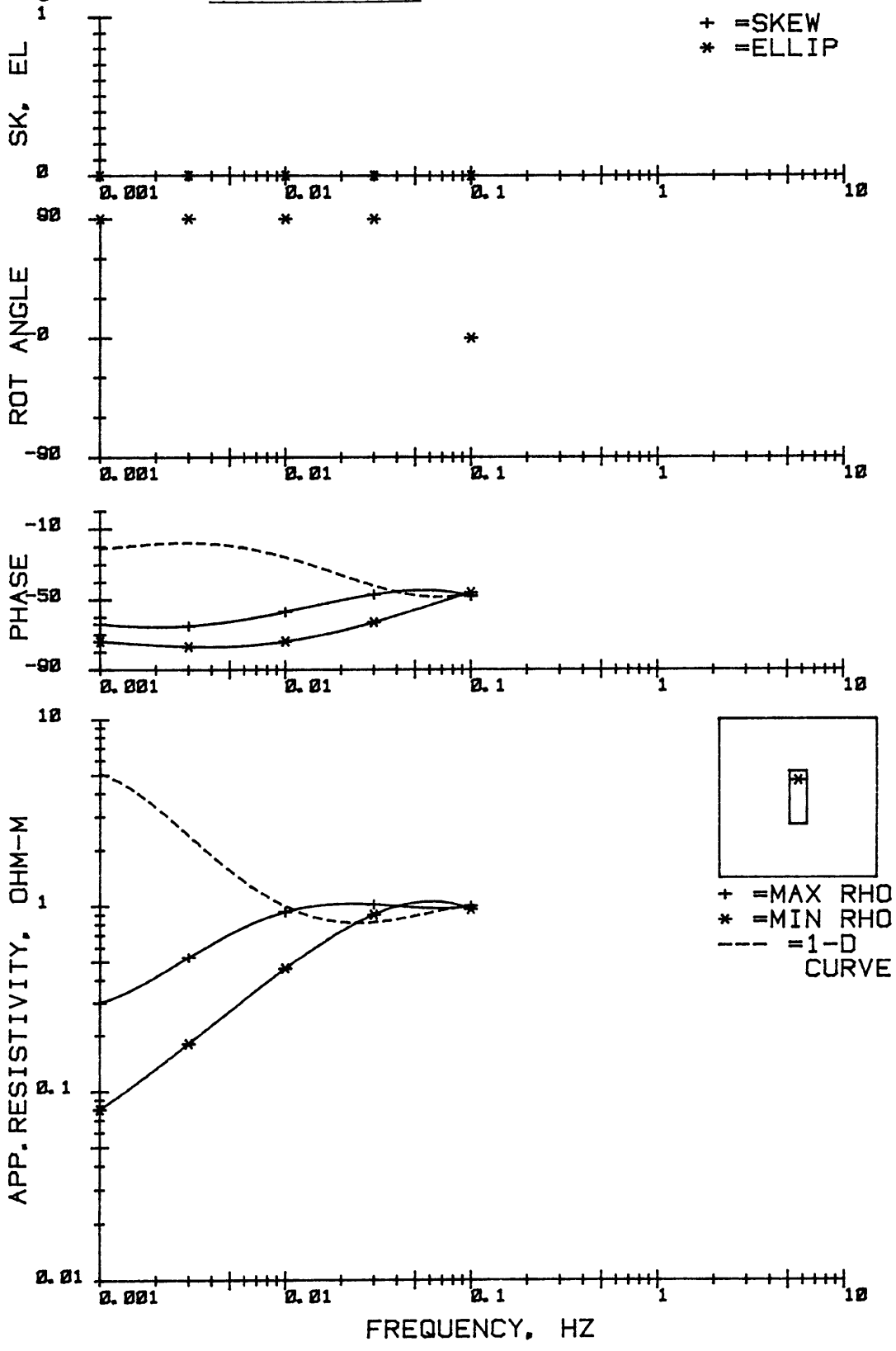


Figure 2.3.15--Site 41--Model 3

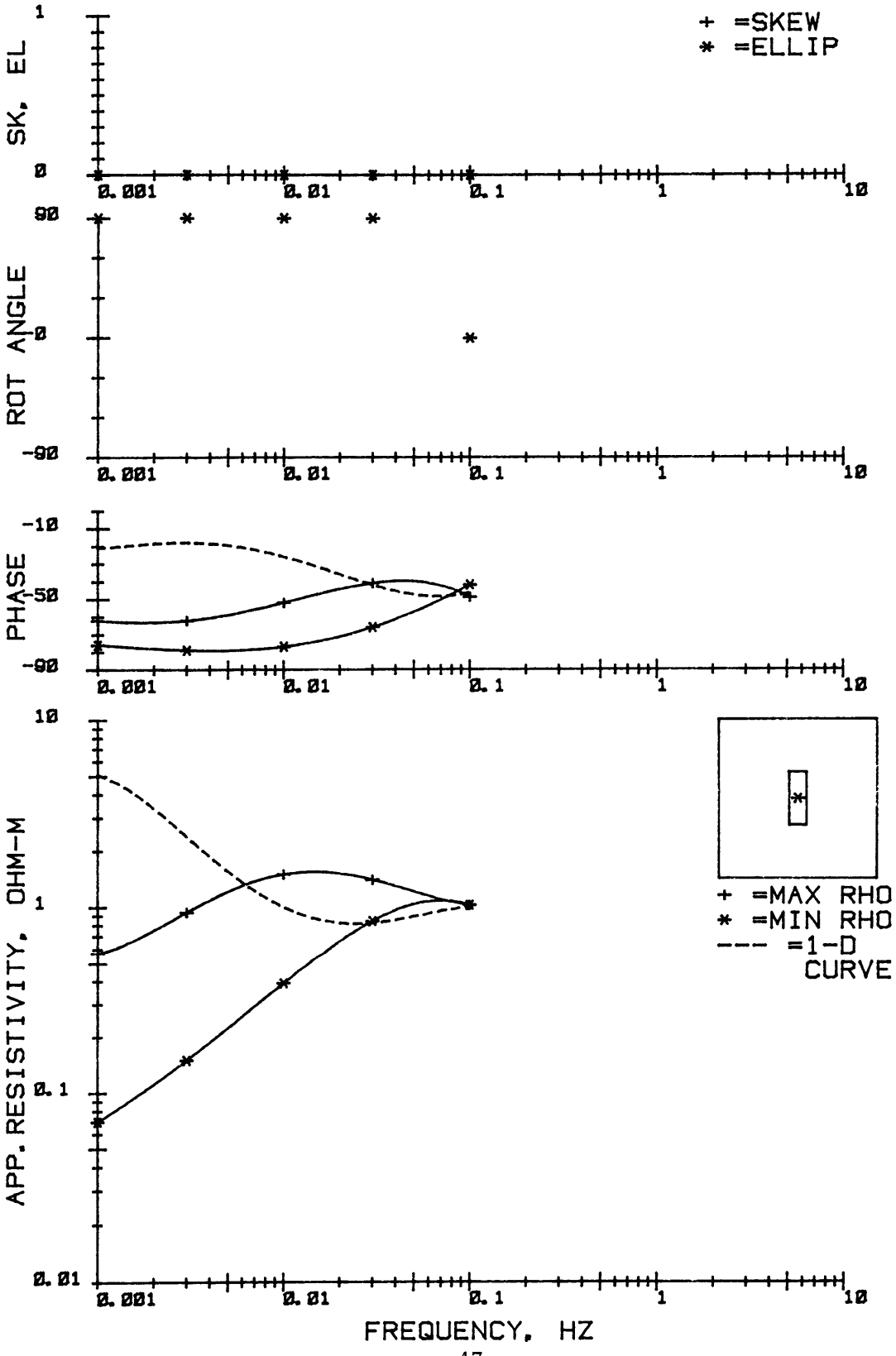
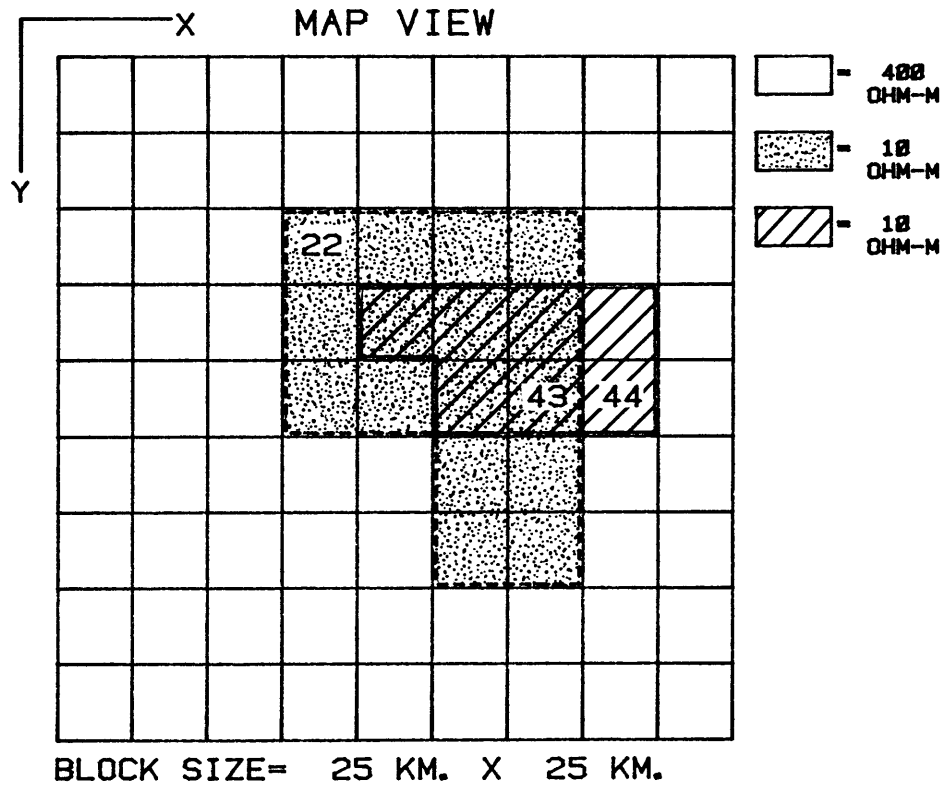


Figure 2.3.16--Conductor Interactions--Model 4



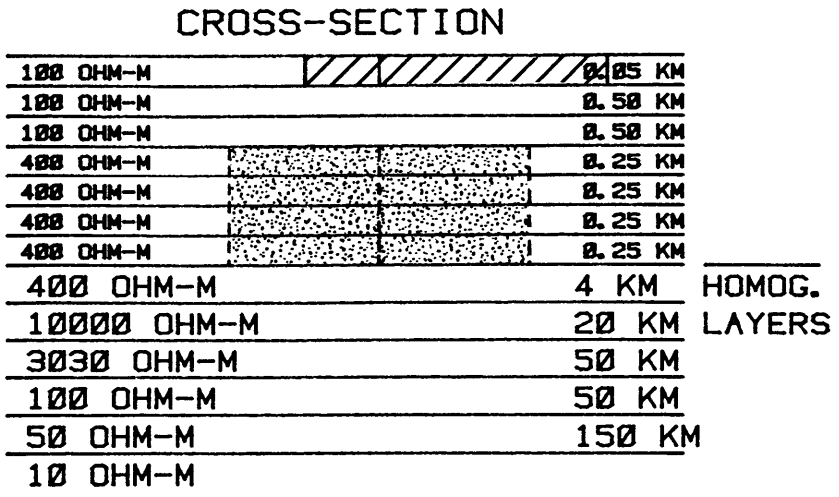


Figure 2.3.17--Site 22 with Surface Conductor--Model 4

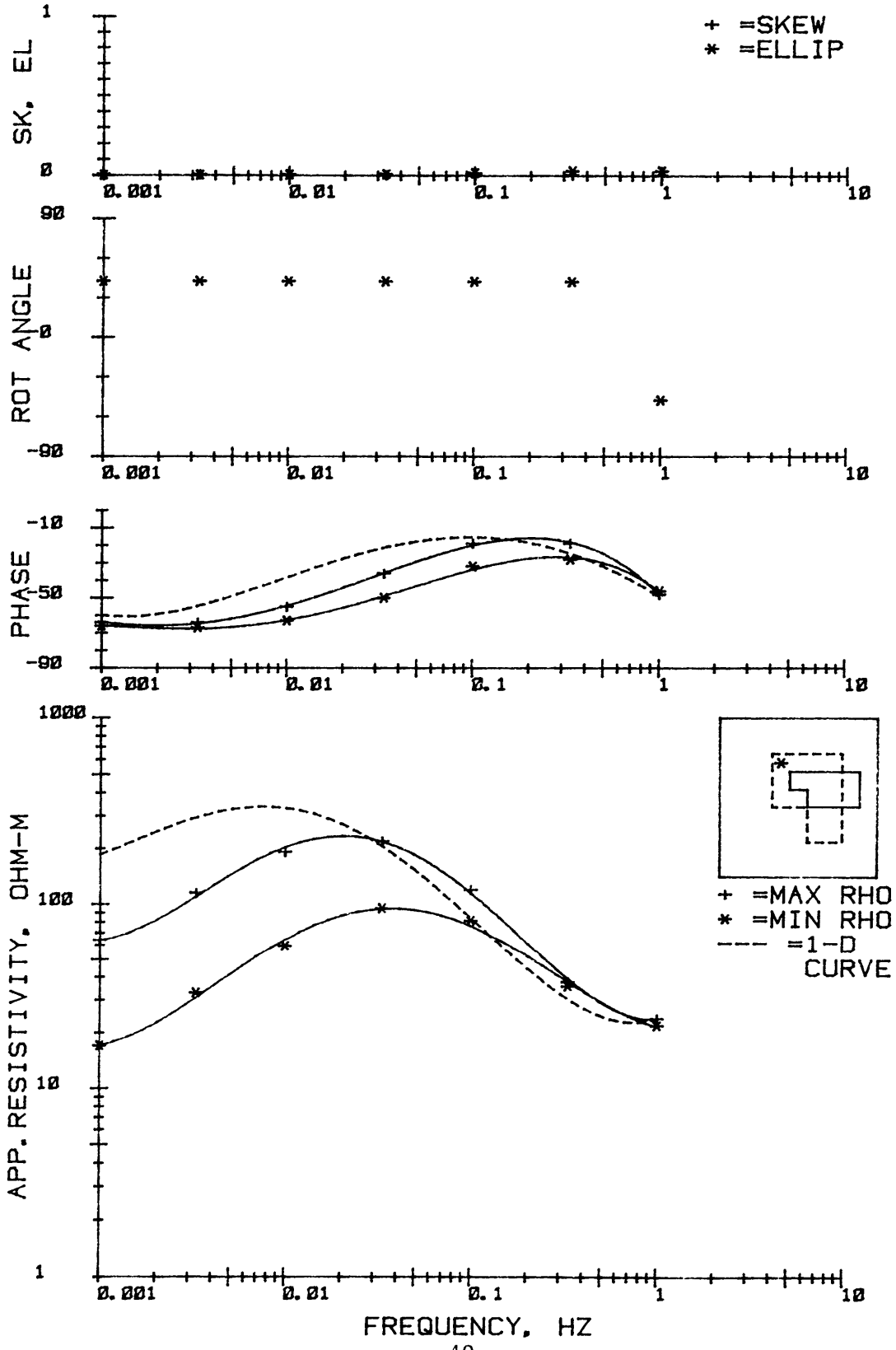


Figure 2.3.18--Site 22 without Surface Conductor--Model 4

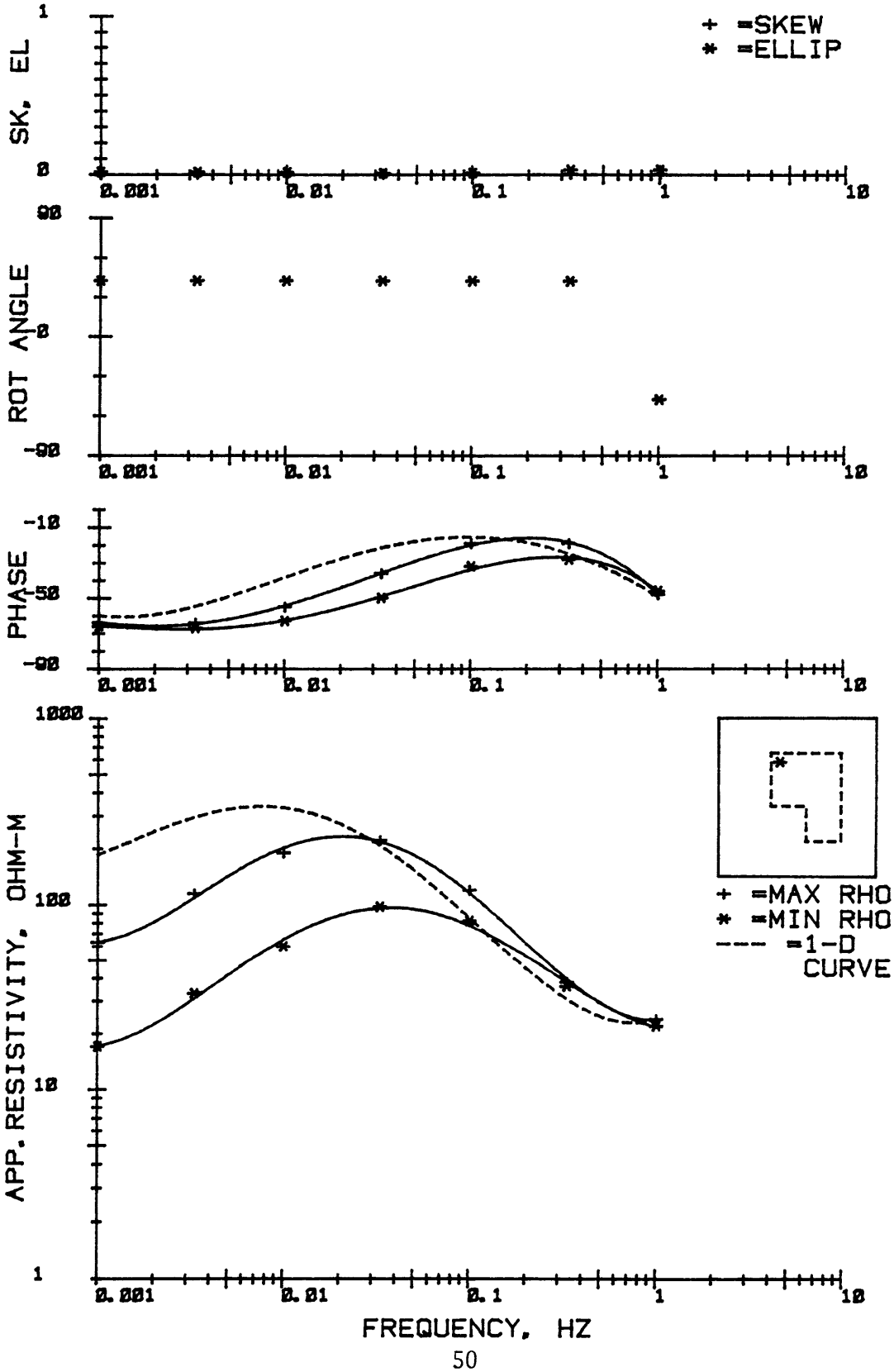


Figure 2.3.19--Site 43 with Surface Conductor--Model 4

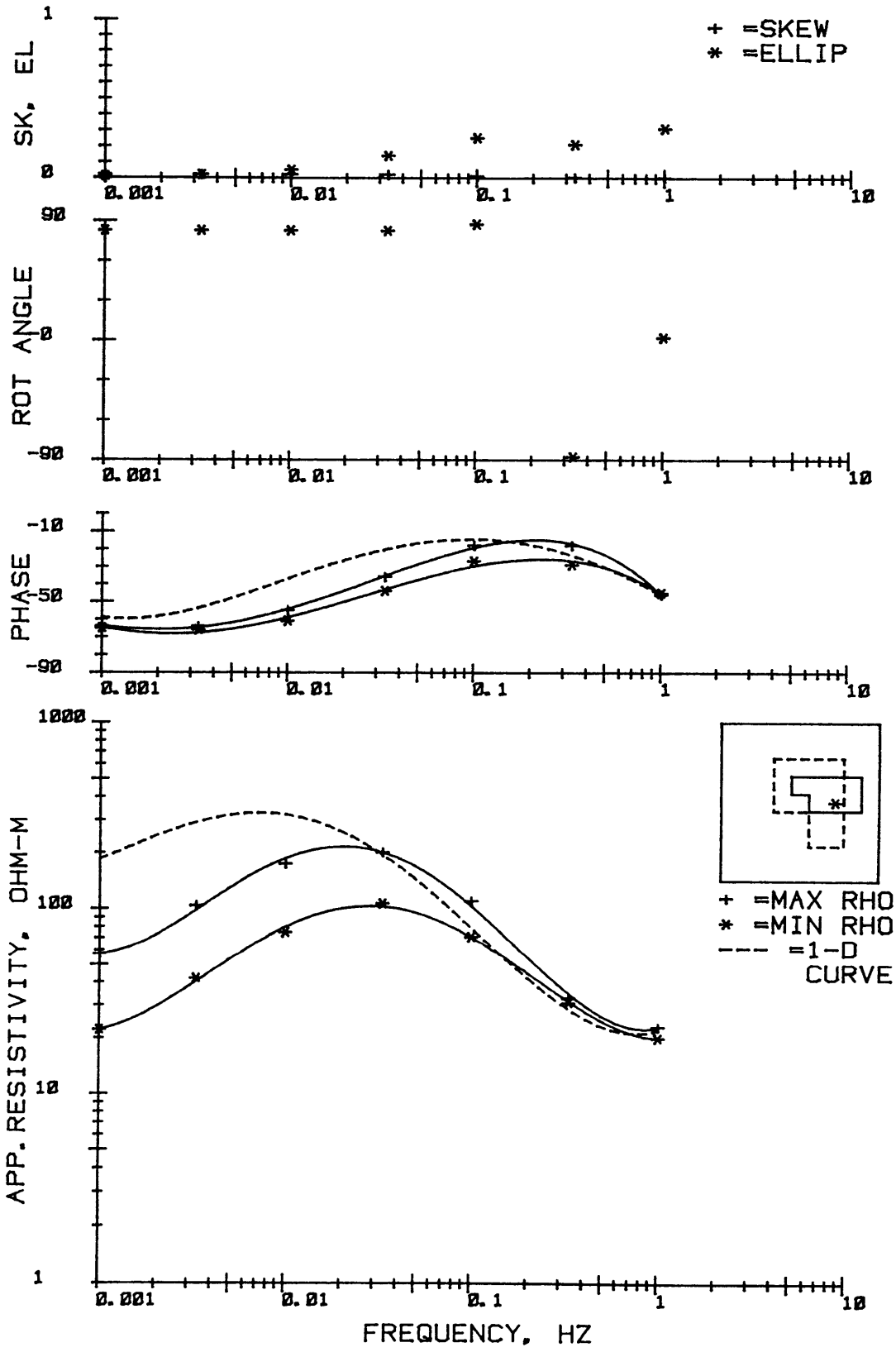


Figure 2.3.20--Site 43 without Surface Conductor--Model 4

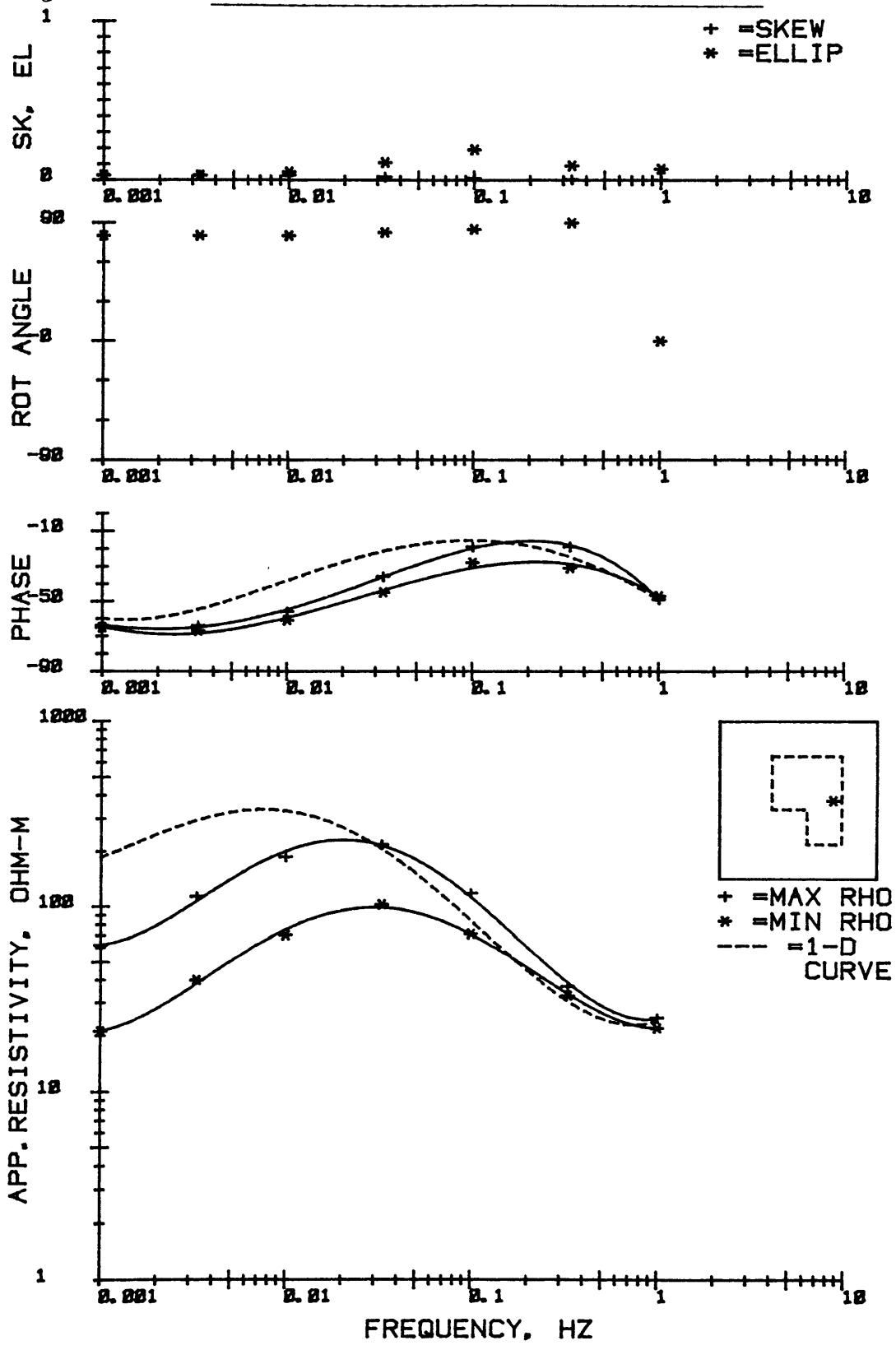


Figure 2.3.21--Site 44 with Surface Conductor--Model 4

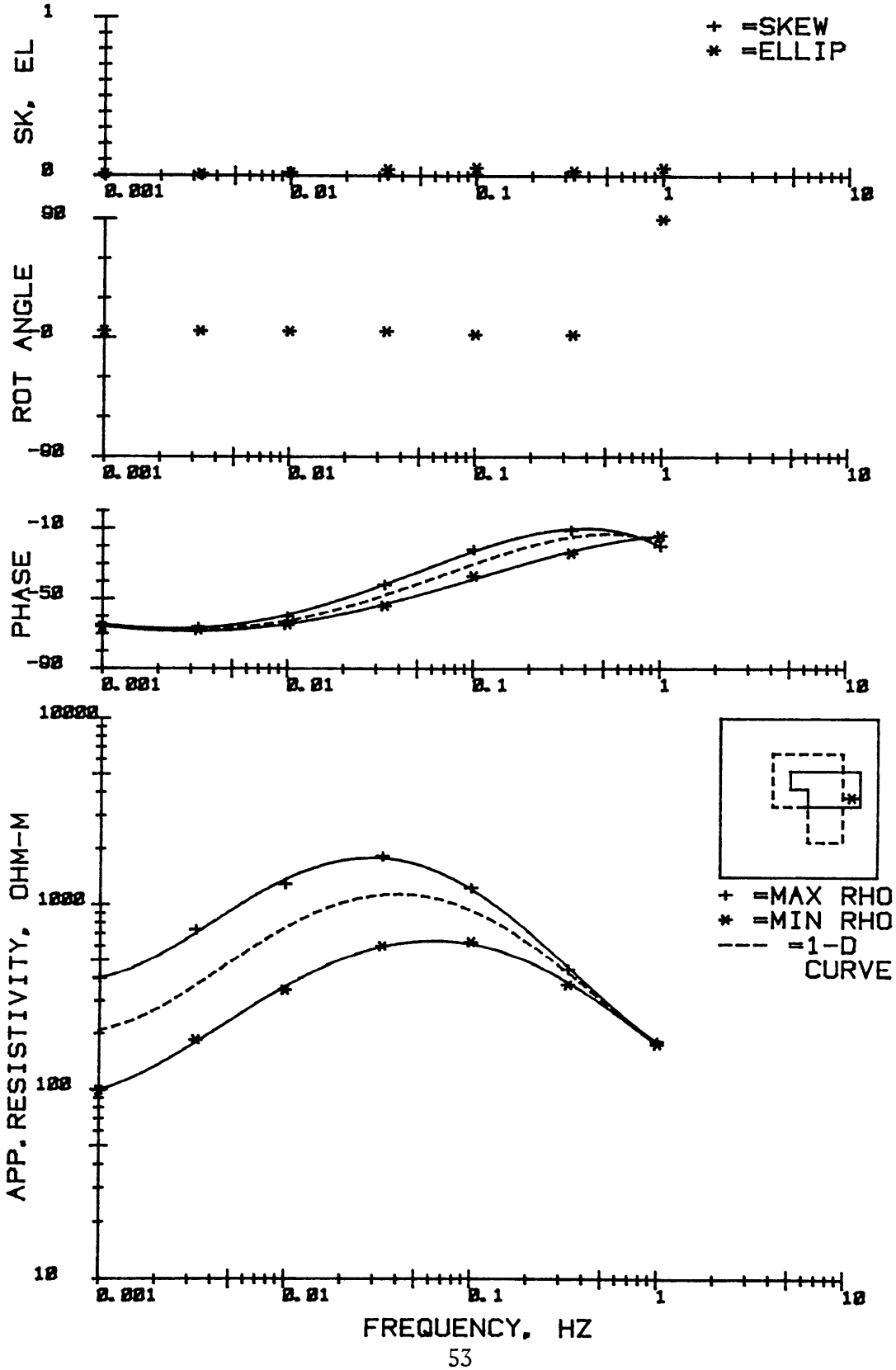
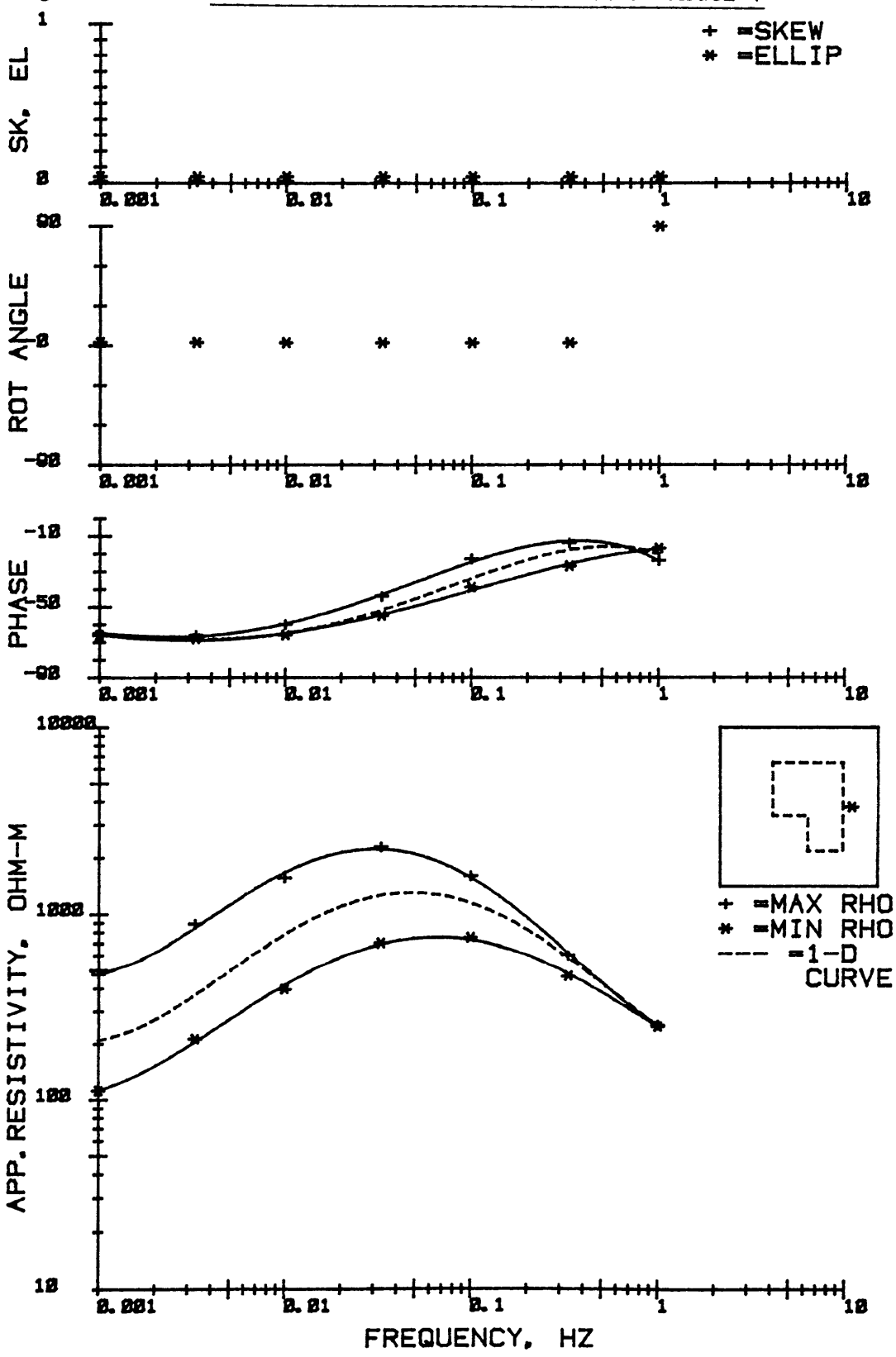


Figure 2.3.22--Site 44 without Surface Conductor--Model 4



2.4 Minimum Phase

One of the questions that can be examined now is whether MT responses from 3-D structures are minimum phase responses. Minimum phase responses are those responses in which the magnitude and phase are related. Given one, the other can be derived from it. Boehl, et. al. (1977) have discussed estimates of the MT tensor impedance using electric and magnetic field measurements. They concluded that the magnitudes of the tensor elements were susceptible to measurement noise, but the phases were not. They suggested using the phase estimates to smooth the magnitude estimates and thus eliminate some of the noise problems. Their work, however, was done under the assumption of 1-D or 2-D structures.

The Transverse Electric (TE) and Transverse Magnetic (TM) modes decouple for 1-D and 2-D structures along the principle axes of the medium, giving an impedance tensor

$$Z(\omega) = \begin{bmatrix} 0 & Z_{xy}(\omega) \\ Z_{yx}(\omega) & 0 \end{bmatrix} \qquad (2.4.1)$$

It is thus sufficient to look at the minimum phase properties of a scalar function, Z_{xy} or Z_{yx} (Boehl, et. al., 1977). There is no set of principal axes along which this

decoupling occurs for general 3-D bodies. We will always have a full tensor. It is therefore necessary to examine the minimum phase properties of a tensor function, Z. If we regard Z as a multichannel filter, then one property of a minimum phase filter is that its inverse is stable (i.e., its Fourier transform exists) and causal (Robinson, 1966). The inverse of $Z(\omega)$ is

$$Z^{-1}(\omega)=\frac{\begin{bmatrix} Z_{yy} & -Z_{xy} \\ -Z_{yx} & Z_{xx} \end{bmatrix}}{\det Z} \qquad (2.4.2)$$

We assume that $Z(\omega)$ is causal and stable, so Z_{xx}, Z_{xy}, Z_{yx}, and Z_{yy} are also. The questions of stability and causality for Z^{-1} are thus dependent upon the properties of 1/det Z (Robinson, 1966). We have now reduced the problem to the examination of a scalar function, 1/det Z. We assume for the moment that 1/det Z is stable and causal. This function is the inverse of a filter given by det Z, however. Det Z must be a minimum phase function for our assumption to be true. If det Z is a minimum phase function, then $Z(\omega)$ is also.

The magnitude and phase of det Z will be related through a Hilbert transform pair if the function is minimum phase (Oppenheim and Shaefer, 1975). This transform pair

is

$$\ln|\det Z(\omega)| = \frac{1}{\pi} \int \frac{\Phi \det Z\ (\omega')}{\omega-\omega'}\, d\omega' \qquad (2.4.3)$$

$$\Phi_{\det Z\ (\omega)} = \frac{1}{\pi} \int \frac{\ln|\det Z(\omega')|}{\omega-\omega'}\, d\omega' \qquad (2.4.4)$$

Boehl, et. al. (1977) show that these equations can be modified to give the following relationship

$$\left.\frac{d(\ln|\det Z|)}{d(\ln\omega)}\right|_{\ln\omega 0} = \frac{2}{\pi^2}\int\left[\left.\frac{d(\ln|\det Z|)}{d(\ln\omega)}\right|_{\ln\omega 0} - \left.\frac{d(\ln|\det Z|)}{d(\ln\omega)}\right|_{\ln\omega}\right] \cdot \ln\left[\coth\left(\frac{\ln\omega-\ln\omega 0}{2}\right)\right] d(\ln\omega) + \frac{2}{\pi}\,\Phi_{\det Z}(\ln\ \omega 0) \qquad (2.4.5)$$

We will use the method of Boehl, et. al. (1977) to test whether the phase and magnitude of det Z are related through (2.4.5).

The model used for this test is shown in Figure 2.3.16. The results of the test are shown in Figures 2.4.1 and 2.4.2.

An apparent 'resistivity' has been computed for plotting purposes and is

$$'\rho_A' = |\det Z|/(\omega\mu) \qquad (2.4.6)$$

The phase plotted is one-half of the phase of det Z. Figure 2.4.1 presents comparisons for two sites above the buried conductor, and Figure 2.4.2 shows comparisons for two sites outside. The phases shown in the top halves of Figures 2.4.1 and 2.4.2 are taken directly from the modelling program. We predict the magnitude of det Z from these phases using the Hilbert transform relation (equation (2.4.5)). The apparent 'resistivities' in the lower halves of the figures are the comparisons between the actual and predicted values. The curves represent the predicted values, while the symbols are the actual values. The agreement between the predicted and actual values of |det Z| is excellent. Many other sites were tested, and the maximum RMS error in apparent 'resistivity' was 4.6% (Site 33, Figure 2.4.2). A 1-D model was similarly tested, and the RMS error was 2.1%. Minimum phase responses were observed all sites tested, within the limits of numerical accuracy. The results of our test strongly suggest that the MT response from 3-D structures is a minimum phase response, although they do not conclusively prove it for all 3-D

bodies.

Figure 2.4.1--Predictions of Apparent 'Resistivity' from Phase inside Conductor

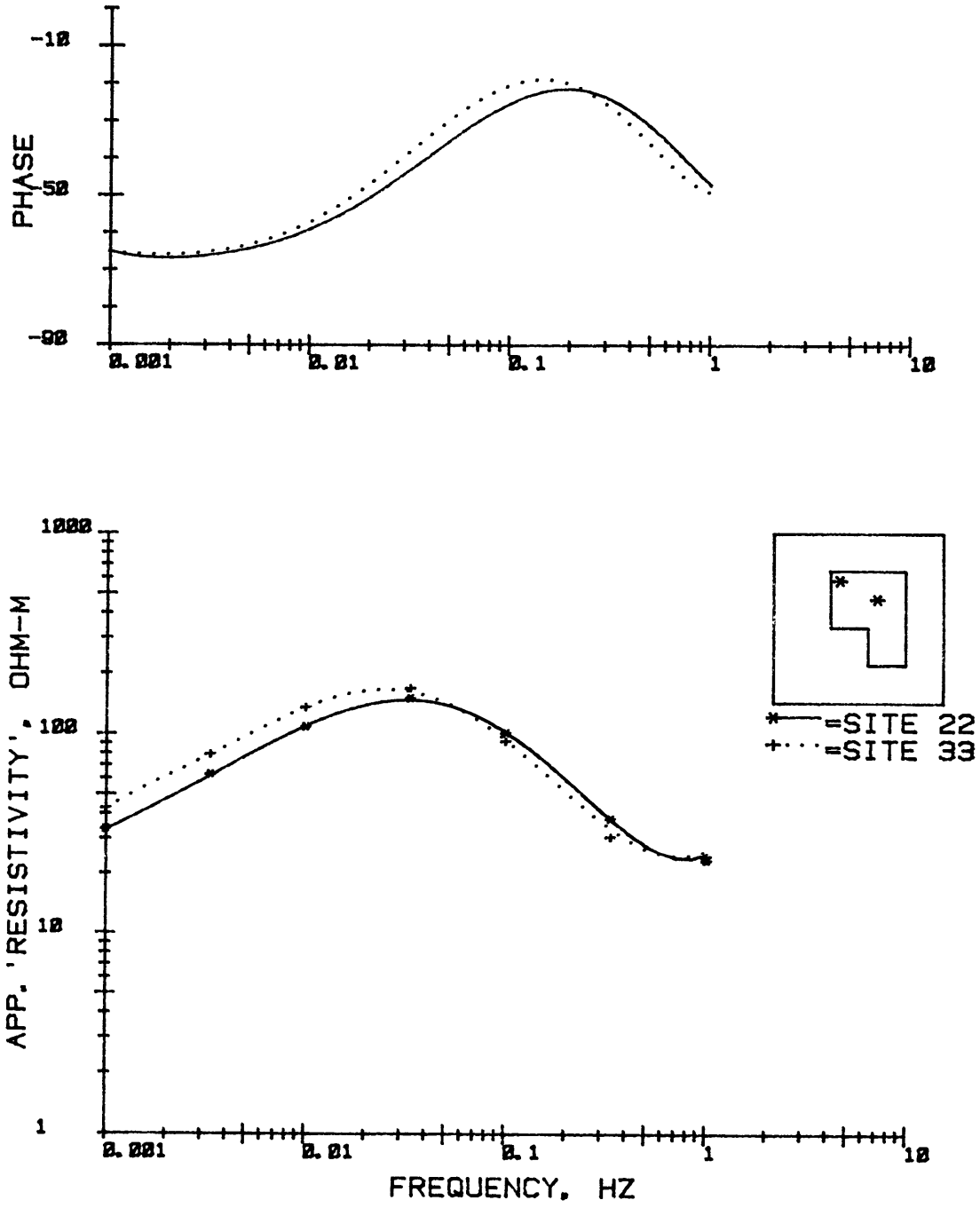
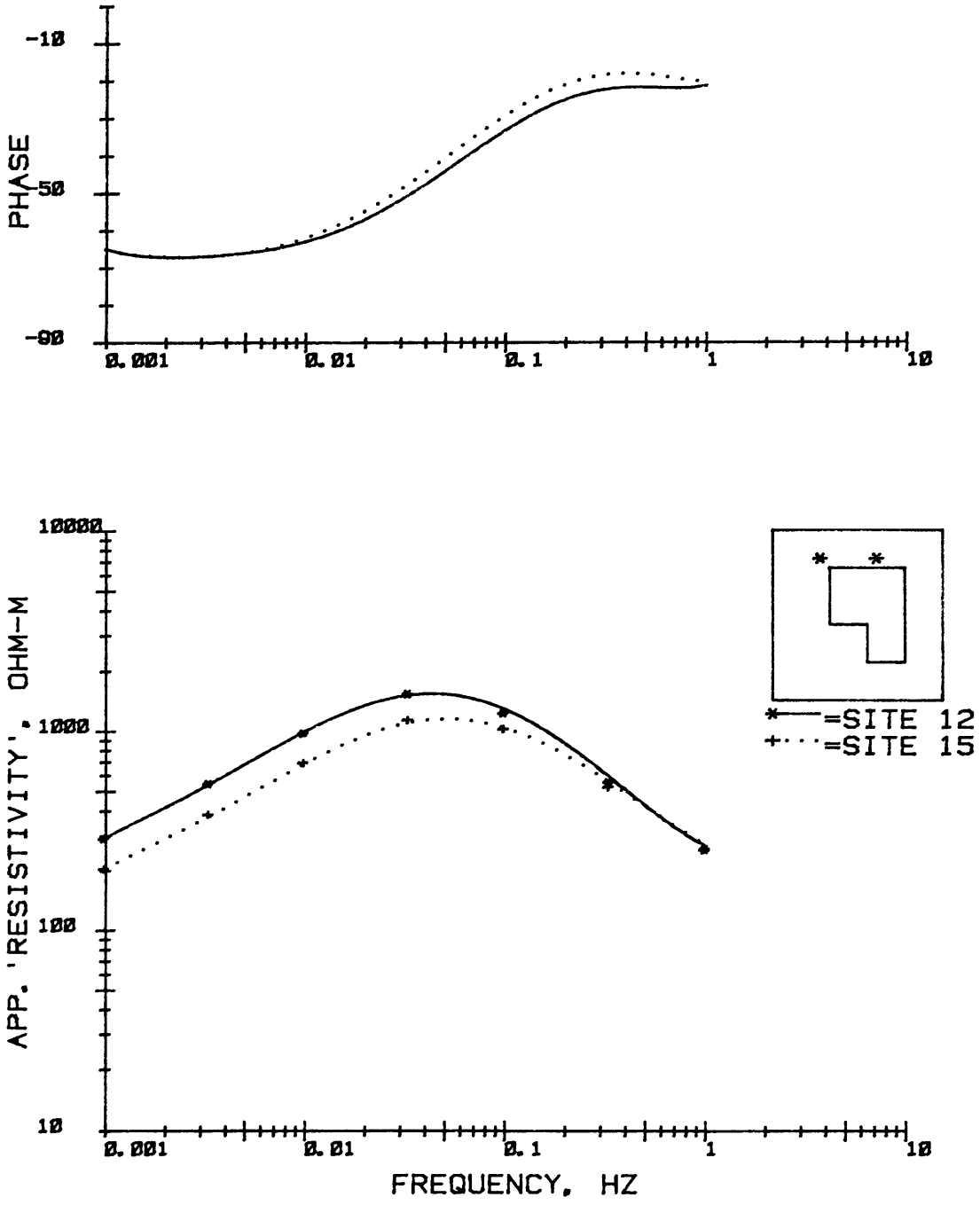


Figure 2.4.2--Predictions of Apparent 'Resistivity' from Phase outside Conductor



2.5 Summary

We have developed a practical 3-D modelling algorithm in this chapter and used it to gain insight into field behavior around complicated structures. We extend Ranganayaki's generalized thin sheet analysis (1978) to allow us to stack heterogeneous thin layers. Methods of Fourier analysis are used to formulate the solution, but this restricts us to spatially repeating models.

Electric fields near complicated structures are locally perturbed by three different mechanisms at low frequencies. Horizontal and vertical current gathering are important for heterogeneities with modest resistivity contrasts compared to the surrounding medium. These mechanisms perturb fields in a DC manner-- i.e., the effect has the same magnitude at any low frequency. Induction of current loops is the dominant mechanism in conductive heterogeneities (1 Ω•m). This mechanism is frequency-dependent, so it is an AC effect. Each of these mechanisms has a different spatial and frequency behavior so identification of the dominant contribution is important. Appendix B outlines procedures for this indentification.

We finally presented evidence, albeit empirical, that the phase and magnitude of the impedance tensor are related through a Hilbert transform pair. The earth response is minimum phase even though the conductivity structure is complicated.

'To stop at that which is beyond understanding is indeed a high attainment.'

Ancient Chinese Philosopher

CHAPTER 3

3.1 Introduction

We outline a method for setting up the inverse problem in this section. The inverse problem is derived for the type of model in Chapter 2, which includes the repetition assumption. We perform a perturbation analysis on the 'normal' problem (equations (2.2.9) and (2.2.10)) to get the relationship between field changes and conductivity perturbations. The conductivity perturbations appear as effective 'sources' for the normal problem. We can thus solve the problem with 'sources' if we find the associated Green's function. We want a Green's function relating field changes at the surface to 'sources' at depth. This desired Green's function for the normal problem ($Dv=\beta$) is related to the Green's function for the adjoint problem ($\tilde{D}u=\gamma$) through the generalized reciprocal relation (Lanczos, 1956). The reciprocity relation will be rederived here. Finally, we show how to compute the Green's function numerically for our problem.

This inverse problem was not programmed because of time limitations, but we show how this method agrees with linearized inverson theory for a 1-D model. Extensive work

is needed with this 3-D inversion and synthetic data to answer the questions of uniqueness and resolution. These tests must be performed before applying the inversion actual data.

3.2 Formulation of the Inverse Problem

The normal problem, Dv, was derived in Section 2.2 (equations 2.2.9 and 2.2.10) and is given by

$$Dv=\begin{bmatrix} -\frac{\partial}{\partial z} & 0 & -\frac{\partial}{\partial x}\left(\rho\frac{\partial}{\partial y}\cdot\right) & j\omega\mu+\frac{\partial}{\partial x}\left(\rho\frac{\partial}{\partial x}\cdot\right) \\ 0 & -\frac{\partial}{\partial z} & -j\omega\mu-\frac{\partial}{\partial y}\left(\rho\frac{\partial}{\partial y}\cdot\right) & \frac{\partial}{\partial y}\left(\rho\frac{\partial}{\partial x}\cdot\right) \\ \sigma_{yx}-\frac{1}{j\omega\mu}\frac{\partial^2}{\partial x\partial y} & \sigma_{yy}+\frac{1}{j\omega\mu}\frac{\partial^2}{\partial x^2} & -\frac{\partial}{\partial z} & 0 \\ -\sigma_{xx}-\frac{1}{j\omega\mu}\frac{\partial^2}{\partial y^2} & -\sigma_{xy}+\frac{1}{j\omega\mu}\frac{\partial^2}{\partial x\partial y} & 0 & -\frac{\partial}{\partial z} \end{bmatrix}\begin{bmatrix} E_x \\ E_y \\ H_x \\ H_y \end{bmatrix} \qquad (3.2.1)$$

We have Dv=0 in a source-free region. Perturbing D to D + δD results in a change in v to v + δv. This perturbation in D is achieved by perturbing the conductivity structure of the medium. We expand (D + δD)(v + δv) and neglect second order terms to get

$$D\delta v = -\delta D v \qquad (3.2.2)$$

Equation (3.2.2) relates field changes both at depth and at the surface to conductivity perturbations everywhere. The right-hand side of (3.2.2) is the effective 'source' term.

We want a relationship between conductivity perturbations at depth and field changes at the surface. Such a relationship is the integral of the appropriate Green's function over the 'sources' at depth. This Green's function must give the response at the surface to a source at depth and is $G_k(r,s)_j$ where r is the receiver location and s is the source location. The convention used for the Green's function notation is that the first variable denotes the response location and the second indicates the source location. The vector indices, k and j, have been added as a reminder that G is a dyad. All further discussion of Green's functions will use this notation. The final inverse problem is given by

$$\delta v_k = -\int_\tau G_k(r,s)_j [(\delta D v)(s)]_j \, d\tau \qquad (3.2.3)$$

We use the Einstein summation notation for repeated indices. The response at the surface to a source at depth will be difficult to compute directly, but the response at depth to a surface source is not. We will now show that these two responses are related through generalized reciprocity. This reciprocal relation is more general than the usual electromagnetic reciprocal relation because it holds for operators which are not self-adjoint.

The derivation for the generalized reciprocity relation is presented in Lanczos(1956), but will be rederived here

for completeness. The normal and adjoint problems are

$$Dv_k(x)=\beta_j(x) \tag{3.2.4}$$

$$\tilde{D}u_j(x)=\gamma_k(x) \tag{3.2.5}$$

where D is j×k and $\tilde{D}$ is k×j. The tilde denotes the Hermetian of D (complex conjugate transpose of D), following Lanczos (1956). We know the solution to the normal problem is given by

$$v_k(r) = \int_S \sum_{j=1}^{\nu} [G_k(r,s)_j \cdot \beta_j(s)] \, ds \tag{3.2.6}$$

where G is the solution to $DG=\delta_j$, and the integration is performed over all sources. We now derive an alternate expression for $v_k(r)$ through the bilinear identity. This identity is

$$\int_\tau (u^*Dv - v(\tilde{D}u)^*) \, d\tau = 0 \tag{3.2.7}$$

Introducing vector notation, (3.2.7) can be rewritten

$$\int_\tau \sum_{j=1}^{4} u_j^*(\tau) D v_k(\tau)\, d\tau = \int_\tau \sum_{k=1}^{4} v_k(\tau) [\tilde{D} u_j(\tau)]^*\, d\tau \quad (3.2.8)$$

becuase both D and $\tilde{D}$ are square, 4×4 operators. We define $\tilde{G}_j(x,s)_k$ to be the Green's function for the adjoint problem, $\tilde{D}_j u_j = \delta_k(x,s)$. $\tilde{G}^*_j(x,s)_k$ is <u>not</u> related to $G_j(r,s)_k$ through simple transpose and conjugation operations--it is a separate operator in general. We substitute $Dv_k(\tau) = \beta_j(\tau)$, $\tilde{D}u_j(\tau) = \delta_k(\tau,s)$, and $u_j^*(\tau) = \tilde{G}^*_j(\tau,s)_k$ into (3.2.8) and get

$$\int_\tau \sum_{j=1}^{4} [\tilde{G}^*_j(\tau,s)_k \beta_j(\tau)]\, d\tau = \int_\tau \sum_{k=1}^{4} v_k(\tau) \delta^*_k(\tau,s)\, d\tau \quad (3.2.9)$$

We integrate (3.2.9) through the delta function and get

$$v_k(s) = \int_\tau \sum_{j=1}^{4} [\tilde{G}^*_j(\tau,s)_k \beta_j(\tau)]\, d\tau \quad (3.2.10)$$

Making the variable substitutions $s \equiv r$ and $\tau \equiv s$ into (3.2.10),

we get another expression for $v_k(s)$ in terms of the Green's function for the adjoint problem

$$v_k(r) = \int_S \sum_{j=1}^{4} \hat{G}^*_j(s,r)_k \beta_j(s)\, ds \qquad (3.2.11)$$

We equate equations (3.2.6) and (3.2.11) term by term to get the generalized reciprocal relation

$$G_k(r,s)_j = \hat{G}^*_j(s,r)_k \qquad (3.2.12)$$

Let us put sources at depth and receivers at the surface. This reciprocal relation says that the kth response coefficient at the surface to the jth source component at depth in the normal problem is related to the jth response component at depth to the kth source component at the surface for the adjoint problem. The next step is to determine the Green's function for the adjoint problem. We will show that $\hat{G}^*$ is easily derived from the solution to the normal problem through a change of variables.

We now derive the adjoint operator and the associated boundary terms. The principle behind this exercise is to make the left-hand side of the bilinear identity (3.2.7) a perfect differential.

This perfect differential is

$$u^*Dv - v(\tilde{D}u)^* = \sum_{i=1}^{3} \partial F_i(u^*,v)/\partial x_i \qquad (3.2.13)$$

where $\tilde{D}$ is the adjoint operator and the right-hand side is the associated boundary term. Lanczos (1956) outlines the procedure for computing $\tilde{D}$ and the boundary term from D. We have three types of terms in Dv:

I. No derivative - Av (A is a scalar)

$$u^*Av - vAu^* = 0 \qquad (3.2.14)$$

so $\tilde{D}^* = A$ and $\partial F_i(u^*,v)/\partial x_i = 0$;

II. First Derivative - $A\frac{\partial v}{\partial x_i}$

$$u^*A\frac{\partial v}{\partial x_i} - \left(-v\frac{\partial}{\partial x_i}(Au^*)\right) = \frac{\partial}{\partial x_i}(u^*Av) \qquad (3.2.15)$$

so $\tilde{D}^* = -\frac{\partial}{\partial x_i}(A\,\cdot\,)$ and $F_i(u^*,v) = u^*Av$;

III. Second Derivative - $A\frac{\partial^2 v}{\partial x_i \partial x_j}$

$$u^*A\frac{\partial^2 v}{\partial x_i \partial x_j} - v\frac{\partial^2}{\partial x_i \partial x_j}(Au^*) = \frac{\partial}{\partial x_i}\left(u^*A\frac{\partial v}{\partial x_j}\right) - \frac{\partial}{\partial x_j}\left(v\frac{\partial}{\partial x_i}(Au^*)\right) \qquad (3.2.16)$$

so $\tilde{\tilde{D}}^* = \frac{\partial^2}{\partial x_i \partial x_j}(A\cdot\ )$, and the associated boundary term is $\frac{\partial}{\partial x_i}(u^* A \frac{\partial v}{\partial x_j}) - \frac{\partial}{\partial x_j}(v \frac{\partial}{\partial x_i}(Au^*))$.

These recipes give the following form for $-\tilde{\tilde{D}}^* u^*$

$$\begin{bmatrix} -\frac{\partial}{\partial z} & 0 & -\sigma_{yx} + \frac{1}{j\omega\mu}\frac{\partial^2}{\partial x \partial y} & \sigma_{xx} + \frac{1}{j\omega\mu}\frac{\partial^2}{\partial y^2} \\ 0 & -\frac{\partial}{\partial z} & -\sigma_{yy} - \frac{1}{j\omega\mu}\frac{\partial^2}{\partial x^2} & \sigma_{xy} - \frac{1}{j\omega\mu}\frac{\partial^2}{\partial x \partial y} \\ \frac{\partial}{\partial y}(\rho(\frac{\partial}{\partial x}\cdot\ )) & j\omega\mu + \frac{\partial}{\partial y}(\rho(\frac{\partial}{\partial y}\cdot\ )) & -\frac{\partial}{\partial z} & 0 \\ -j\omega\mu - \frac{\partial}{\partial x}(\rho(\frac{\partial}{\partial x}\cdot\ )) & -\frac{\partial}{\partial x}(\rho(\frac{\partial}{\partial y}\cdot\ )) & 0 & -\frac{\partial}{\partial z} \end{bmatrix} \begin{bmatrix} u_1^* \\ u_2^* \\ u_3^* \\ u_4^* \end{bmatrix}$$

(3.2.17)

with the associated boundary terms

$$\frac{\partial}{\partial x}(u_1^* \rho \frac{\partial v_4}{\partial x} - v_4 \rho \frac{\partial u_1^*}{\partial x}) - \frac{\partial}{\partial x}(\rho u_1^* \frac{\partial v_3}{\partial y}) + \frac{\partial}{\partial x}(u_2^* \frac{\partial}{\partial y}(\rho v_4)) +$$

$$\frac{1}{j\omega\mu}\frac{\partial}{\partial x}(u_3^* \frac{\partial v_2}{\partial x} - v_2 \frac{\partial u_3^*}{\partial x} - u_3^* \frac{\partial v_1}{\partial y}) + \frac{1}{j\omega\mu}\frac{\partial}{\partial x}(u_4^* \frac{\partial v_2}{\partial y}) +$$

$$\frac{\partial}{\partial y}[v_3 \rho \frac{\partial u_1^*}{\partial x} - v_4 \frac{\partial}{\partial x}(\rho u_2^*) + v_3 \rho \frac{\partial u_2^*}{\partial y} - u_2^* \rho \frac{\partial v_3}{\partial y}] +$$

$$\frac{1}{j\omega\mu}\frac{\partial}{\partial y}(v_1 \frac{\partial u_3^*}{\partial x} + v_1 \frac{\partial u_4^*}{\partial y} - u_4^* \frac{\partial v_1}{\partial y} - v_2 \frac{\partial u_4^*}{\partial x}) -$$

$$\frac{\partial}{\partial z}(u_1^* v_1 + u_2^* v_2 + u_3^* v_3 + u_4^* v_4) \tag{3.2.18}$$

We now choose $u^* = (H_y', -H_x', E_y', -E_x')$ and substitute this into (3.2.17) to get

$$-\mathfrak{H}^* u^* = \begin{bmatrix} -\frac{\partial H_y'}{\partial z} - \sigma_{yx} E_y' + \frac{1}{j\omega\mu} \frac{\partial^2 E_y'}{\partial x \partial y} - \sigma_{xx} E_x' - \frac{1}{j\omega\mu} \frac{\partial^2 E_x'}{\partial y^2} \\ \frac{\partial H_x'}{\partial z} - \sigma_{yy} E_y' - \frac{1}{j\omega\mu} \frac{\partial^2 E_y'}{\partial x^2} - \sigma_{xy} E_x' + \frac{1}{j\omega\mu} \frac{\partial^2 E_x'}{\partial x \partial y} \\ \frac{\partial}{\partial y}\left(\rho \frac{\partial H_y'}{\partial x}\right) - j\omega\mu H_x' - \frac{\partial}{\partial y}\left(\rho \frac{\partial H_x'}{\partial y}\right) - \frac{\partial E_y'}{\partial z} \\ -j\omega\mu H_y' - \frac{\partial}{\partial x}\left(\rho \frac{\partial H_y'}{\partial x}\right) + \frac{\partial}{\partial x}\left(\rho \frac{\partial H_x'}{\partial y}\right) + \frac{\partial E_x'}{\partial z} \end{bmatrix} \tag{3.2.19}$$

We recognize that (3.2.19) is just Maxwell's equations in the form of (2.2.9) and (2.2.10) because $\sigma_S = \sigma_S^T$ (see Appendix D for proof of this). We thus have the differential equation for the adjoint problem. The specification of the adjoint is not complete, however, because we have yet to discuss the boundary conditions for (E', H').

We determine the adjoint boundary conditions by requiring that the integral of the boundary term in the bilinear identity (equation (3.2.18)) vanish identically (Lanczos, 1956). We substitute $u^* = (H_y', -H_x', E_y', -E_x')$, $v = (E_x, E_y, H_x, H_y)$, and the appropriate definitions of E_z, H_z,

E_z', and H_z' into (3.2.18) to get

$$\int_\tau \sum_{i=1}^{3} \frac{\partial}{\partial x_i} F_i(u^*,v)\, d\tau = \int_\tau \nabla\cdot\left(E'\times H - E\times H'\right) d\tau \qquad (3.2.21)$$

Our goal, then, will be to determine the boundary conditions which force the integral in (3.2.21) to vanish. We also choose these boundary conditions so that the form of the adjoint problem is identical to that of the normal problem. We then have the adjoint solution if we solve the normal problem and reorder the normal solution vector (from v to u^*).

The volume integral in (3.2.21) can be transformed into an integral over the surface enclosing the volume via Gauss' law. The volume of interest encloses the current sheet at the surface, the heterogeneous crust, and the mantle structure beneath the crust. This volume is shown in Figure 3.2.1. We expand the surface integral into its six contributory integrals and consider each separately

$$\begin{aligned}\int_\tau \nabla\cdot(E'\times H - E\times H')\,d\tau = &\int\left((E'\times H - E\times H')\cdot\hat{z}\big|_{z-} + (E'\times H - E\times H')\cdot\hat{z}\big|_{z+}\right)dxdy \\ &+\int\left((E'\times H - E\times H')\cdot\hat{x}\big|_{x-} + (E'\times H - E\times H')\cdot\hat{x}\big|_{x+}\right)dydz \\ &+\int\left((E'\times H - E\times H')\cdot\hat{y}\big|_{y-} + (E'\times H - E\times H')\cdot\hat{y}\big|_{y+}\right)dxdz\end{aligned} \qquad (3.2.22)$$

The requirement of repetition beyond the boundaries shown in

Figure 3.2.1 forces the third and fourth integrals to cancel and the fifth and sixth integrals to cancel in (3.2.22). We show the first two integrals in (3.2.22) vanish separately by considering the volume above the region ($z \leq z-$) and the volume below the region ($z \geq z+$).

The integral for the volume beneath the heterogeneous region is again transformed into a surface integral using Gauss' law. The repetition requirement forces the integrals over the sides to cancel, and we are left with

$$\int_\tau \nabla\cdot(E'\times H - E\times H')d\tau = \int\left((E'\times H - E\times H')\cdot\hat{z}\Big|_\infty + (E'\times H - E\times H')\cdot\hat{z}\Big|_{z-}\right)dxdy \qquad (3.2.23)$$

The left-hand side of (3.2.23) vanishes because we apply Lorentz's lemma. This lemma is valid for anisotropic, heterogeneous media if $\sigma=\sigma^T$ (Kong, 1975). The two conditions imposed by Lorentz's lemma are that the volume contain no sources and that the medium for (E',H') be the same as that for (E,H). We thus have two more boundary conditions for the adjoint problem. First, we must use the same mantle structure for the adjoint problem. Second, the mantle must contain no sources.

The last requirement we impose on (E',H') is that they satisfy a radiation condition (Stratton, 1941). This condition means $E'\to 0$ and $H'\to 0$ at $z\to\infty$, and the first integral in (3.2.23) vanishes. Equation (3.2.23) thus reduces to

$$\int (E' \times H - E \times H') \cdot \hat{z}|_{z-} dxdy = 0 \qquad (3.2.24)$$

We can use the same arguments for the volume above the heterogeneous region to show that

$$\int (E' \times H - E \times H') \cdot \hat{z}|_{z+} dxdy = 0 \qquad (3.2.25)$$

These arguments require that there be no sources in the air, that the air have some conductivity (so that the radiation condition is satisfied), and that the air for the adjoint problem be identical to that for the normal problem. We substitute (3.2.24) and (3.2.25) into (3.2.22) and get

$$\int_\tau \nabla \cdot (E' \times H - E \times H') \, d\tau = 0 \qquad (3.2.26)$$

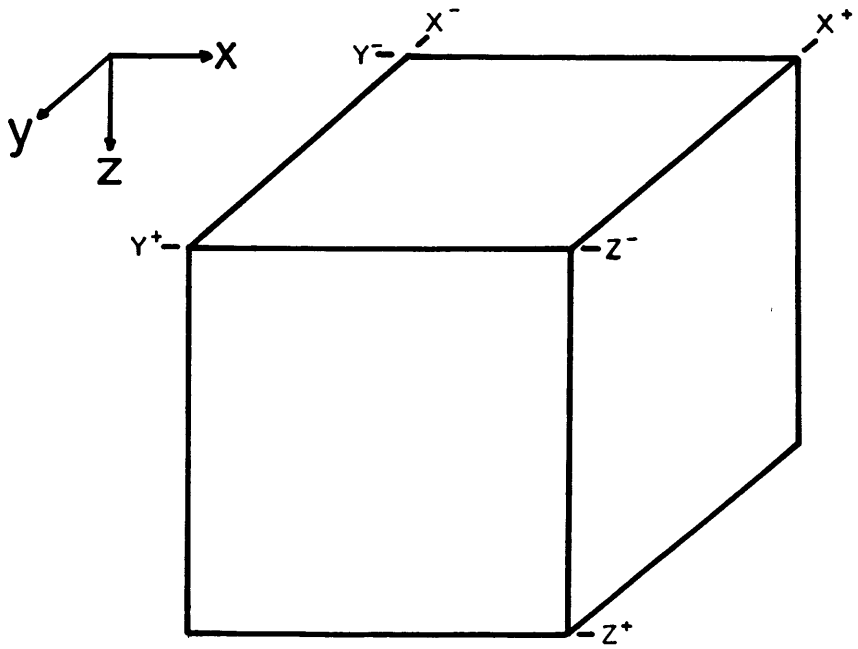
as was desired.

We have derived the adjoint boundary conditions by requiring that (3.2.22) vanish. The boundary conditions are as follows: the media above and below the heterogeneous region are the same as for the normal problem; the model repeats itself; the only sources are within the heterogeneous region; and that the adjoint solution satisfy radiation conditions. We further require that the sources be located in a current sheet at the surface. This last

specification completes the process of making the adjoint problem identical to the normal one.

We have now shown that we can get the adjoint solution from the normal solution merely by reordering the solution terms. Our numerical method for solving $Dv=\beta$ generates basis vectors from which all possible solutions may be generated. We can put delta function sources at the surface receiver points, solve for the surface fields, and downward continue those fields to depth at the source (= conductivity perturbation) locations. The Green's function for the normal problem giving the response at depth due to a surface point source is thus generated. We rearrange terms to get the adjoint operator's Green's function for the response at depth to a surface point source. This function is equal to the Green's function for the normal problem giving the response at the surface due to a source at depth by generalized reciprocity. The desired Green's function for the inverse problem can thus be derived.

Figure 3.2.1--Integration Volume



3.3 Comparison to a Simple 1-D Inversion

We now apply this inverse technique to a simple problem to show that it does indeed work. The problem is a 1-D problem consisting of a layer over a halfspace (see Figure 3.3.1). We have chosen this example because we can compare analytical results for the two different approaches to the inverse problem and show that they are identical.

The two possible polarizations (E_x-H_y and E_y-H_x) decouple for the 1-D problem if we assume no x or y dependence in the fields and use uniform current sheet sources. We will work with just the E_y-H_x polarization. The decoupled 1-D equations for E_y and H_x are

$$\frac{\partial E_y}{\partial z} = j\omega\mu H_x \qquad (3.3.1)$$

$$\frac{\partial H_x}{\partial z} = -\sigma E_y \qquad (3.3.2)$$

We use the continuity of tangential fields at the interfaces at z=0 and z=d as a boundary condition, and our source at the surface is a uniform current sheet in the y direction. The source condition is thus $H_x=J_y$ at z=0. The fields in the layer and the halfspace are given by

$$E_{y1}(z) = -\frac{J_y\left(1+\frac{k_2}{k_1}\right)\exp(-jk_1d)\cos(k_1z)}{\frac{jk_1}{\omega\mu}\sin(k_1d) - \frac{k_2}{\omega\mu}\cos(k_1d)} + J_y\frac{\omega\mu}{k_1}\exp(-jk_1z) \tag{3.3.3}$$

$$H_{x1}(z) = -\frac{J_y\left(1+\frac{k_2}{k_1}\right)j\exp(-jk_1d)\sin(k_1z)}{j\sin(k_1d) - \frac{k_2}{k_1}\cos(k_1d)} - J_y\exp(-jk_1z) \tag{3.3.4}$$

$$E_{y2}(z) = -\frac{\left(1+\frac{k_2}{k_1}\right)J_y\cos(k_1d)\exp(-jk_1d-jk_2d)}{\frac{jk_1}{\omega\mu}\sin(k_1d) - \frac{k_2}{\omega\mu}\cos(k_1d)}\exp(jk_2z)$$

$$+ J_y\frac{\omega\mu}{k_1}\exp(jk_2z-jk_1d-jk_2d) \tag{3.3.5}$$

$$H_{x2}(z) = \frac{k_2}{\omega\mu}E_{y2}(z) \tag{3.3.6}$$

where $k_1 = (1+j)\cdot\sqrt{(\omega\mu\sigma_1/2)}$ and $k_2 = (1+j)\cdot\sqrt{(\omega\mu\sigma_2/2)}$.

We are interested in the sensitivity of E_y at the surface to changes in the halfspace conductivity, σ_2. Specifically, what is the change in E_{y1} due to a change in σ_2? We will first derive this sensitivity using our generalized reciprocity approach in the previous section and then compare it to the result from linearized inversion.

Dv and $\hat{D}^*u^*$ for this problem are

$$Dv = \begin{bmatrix} -\frac{\partial}{\partial z} & 0 & 0 & j\omega\mu \\ 0 & -\frac{\partial}{\partial z} & -j\omega\mu & 0 \\ 0 & \sigma & -\frac{\partial}{\partial z} & 0 \\ -\sigma & 0 & 0 & -\frac{\partial}{\partial z} \end{bmatrix} \begin{bmatrix} E_x \\ E_y \\ H_x \\ H_y \end{bmatrix} \tag{3.3.7}$$

$$\hat{D}^*u^* = \begin{bmatrix} -\frac{\partial}{\partial z} & 0 & 0 & \sigma \\ 0 & -\frac{\partial}{\partial z} & -\sigma & 0 \\ 0 & j\omega\mu & -\frac{\partial}{\partial z} & 0 \\ -j\omega\mu & 0 & 0 & -\frac{\partial}{\partial z} \end{bmatrix} \begin{bmatrix} H_y' \\ -H_x' \\ E_y' \\ -E_x' \end{bmatrix} \tag{3.3.8}$$

Perturbation analysis (equation (3.2.2)) gives

$$D\begin{bmatrix} \Delta E \\ \Delta H \end{bmatrix} = \begin{bmatrix} 0 \\ 0 \\ E_y \Delta\sigma \\ -E_x \Delta\sigma \end{bmatrix} \tag{3.3.9}$$

We now consider the bilinear identity for $D\Delta v$ to give us the source for the adjoint problem. This identity is

$$\int_\tau \left[u^* D\Delta v - (\Delta v)\cdot(\hat{D}u)^*\right] d\tau = 0 \qquad (3.3.10)$$

We want to consider the surface ΔE_y component of Δv only, so $(\hat{D}u)^*$ must be $(0, -J_y\delta(z-0), 0, 0)$. Note that we choose the same source as in the normal problem. The Green's function for this problem is given by $\hat{G}^*_j(r,0)_2$, and (3.3.10) reduces to

$$\iint(-J_y\Delta E_y)\, dxdy = \iint dxdy \int \hat{G}^*_j(r,0)_2(D\Delta v)\, dz \qquad (3.3.11)$$

If we just equate the kernels of the surface integrals, then (3.3.11) becomes

$$-J_y\Delta E_y = \int \hat{G}^*_j(r,0)_2(D\Delta v)\, dz \qquad (3.3.12)$$

We know $D\Delta v$ from (3.3.9), so

$$-J_y\Delta E_y = \int[\hat{G}^*_3(r,0)_2(E_y(z)\Delta\sigma(z)) - \hat{G}^*_4(r,0)_2(E_x(z)\Delta\sigma(z))]dz \qquad (3.3.13)$$

$E_x(z)$ is zero if the source is J_y because there is no cross-coupling in the 1-D problem. Equation (3.3.13) is thus

$$-J_y\Delta E_y = \int \hat{G}^*_3(r,0)_2 E_y(z)\Delta\sigma(z)\, dz \qquad (3.3.14)$$

$\underset{\sim}{G}^*_{3(r,0)_2}$ is the third response component at depth (r) to the second source component at the surface. We know from the previous section (equation (3.2.21)) that the third response component is E_y, and the second source component is a current sheet in the y direction at the surface. Thus, $\underset{\sim}{G}^*_{3(r,0)_2} = E_y(z)$. Substitution of this result into (3.3.14) yields

$$-J_y \Delta E_y = \int E_y(z) E_y'(z) \Delta\sigma(z)\, dz \qquad (3.3.15)$$

The source for E_y' is the same source as for Ey for the 1-D problem, so $E_y' = E_y$. We also only want the sensitivity of E_y at the surface to changes in the halfspace conductivity, so $\Delta\sigma(z) = \Delta\sigma_2 U_1(z-d)$, where U_1 is the unit step function. The sensitivity is thus given by

$$-J_y \Delta E_{y_{surface}} = \Delta\sigma_2 \int_d^\infty E_{y2}^2(z)\, dz \qquad (3.3.16)$$

We substitute the expression for $E_{y2}(z)$ given by (3.3.5) into (3.3.16) and integrate to get

$$\Delta Ey_{surface} = \frac{-\frac{J_y k_2 \omega\mu}{2\sigma_2 k_1^2}}{\left(j\sin(k_1 d) - \frac{k_2}{k_1}\cos(k_1 d)\right)^2} \Delta\sigma_2 \qquad (3.3.17)$$

We now derive the same result using linearized inversion theory. This method assumes that

$$\Delta E_y \cong \left(\frac{\partial E_y}{\partial \sigma_2}\right)_{z=0} \cdot \Delta\sigma_2 \qquad (3.3.18)$$

where $\partial E_y/\partial\sigma 2$ is the partial derivative of (3.3.3) with respect to $\sigma 2$. This derivative is

$$\left(\frac{\partial E_y}{\partial \sigma 2}\right)_{z=0} = \frac{-\frac{Jyk_2\omega\mu}{2\sigma_2 k_1^2}}{\left(j\sin(k_1 d)-\frac{k_2}{k_1}\cos(k_2 d)\right)^2} \qquad (3.3.19)$$

We substitute (3.3.19) into (3.3.18) and compare this result to (3.3.17). These two expressions are identical, thus showing that the 3-D inversion scheme reduces to a known result in the case of a 1-D structure.

3.4 Source Terms for 3-D Inversion

We show that conductivity perturbations are equivalent to current sources at depth and perform the sensitivity analysis here. The sensitivity derived in this section is the surface electric field change due to a conductivity perturbation at depth. Point sources must be used for 3-D inversion because fields vary in both the x and y directions at the surface. This situation is contrasted with that of the 1-D inversion in the previous section in which uniform current sheets were used. The analysis of the 3-D problem cannot be compared to an analytic result because of the problem's complexity, however.

We begin with the integral form of the bilinear identity, as in the last section. We see that Du must be $(\beta_1,0,0,0)$ or $(0,\beta_2,0,0)$ in order to analyze the changes in surface electric fields (because $\Delta v=(\Delta E_x, \Delta E_y, \Delta H_x, \Delta H_y)$). We expand $\tilde{D}^* u^* = \beta^*$ into its component equations to determine what kinds of sources are β_1 and β_2. $\tilde{D}^* u^* = \beta^*$ is

$$\begin{bmatrix} \frac{\partial}{\partial z} & 0 & \sigma_{yx}-\frac{1}{j\omega\mu}\frac{\partial^2}{\partial x\partial y} & -\sigma_{xx}-\frac{1}{j\omega\mu}\frac{\partial^2}{\partial y^2} \\ 0 & \frac{\partial}{\partial z} & \sigma_{yy}+\frac{1}{j\omega\mu}\frac{\partial^2}{\partial x^2} & -\sigma_{xy}+\frac{1}{j\omega\mu}\frac{\partial^2}{\partial x\partial y} \\ -\frac{\partial}{\partial y}\left(\rho\left(\frac{\partial}{\partial x}\bullet\right)\right) & -j\omega\mu-\frac{\partial}{\partial y}\left(\rho\left(\frac{\partial}{\partial y}\bullet\right)\right) & \frac{\partial}{\partial z} & 0 \\ j\omega\mu+\frac{\partial}{\partial x}\left(\rho\left(\frac{\partial}{\partial x}\bullet\right)\right) & \frac{\partial}{\partial x}\left(\rho\left(\frac{\partial}{\partial y}\bullet\right)\right) & 0 & \frac{\partial}{\partial z} \end{bmatrix} * \begin{bmatrix} H_y' \\ -H_x' \\ E_y' \\ -E_x' \end{bmatrix} = \begin{bmatrix} \beta_1 \\ \beta_2 \\ 0 \\ 0 \end{bmatrix}$$

(3.4.1)

We simplify this equation and rearrange it into the two component equations

$$\frac{\partial E_S'}{\partial z}+j\omega\mu(i_z\times H_S')+\nabla_S(\rho_{zz}(\nabla_S\times H_S')\cdot i_z) = 0 \qquad (3.4.2)$$

$$\frac{\partial H_S'}{\partial z}+i_z\times(\sigma_S E_S')-\nabla_S((\nabla_S\times E_S')\cdot i_z/(j\omega\mu)) = i_z\times\begin{bmatrix}\beta_1\\ \beta_2\end{bmatrix} \qquad (3.4.3)$$

We recognize through comparison to $\nabla\times H=\sigma E+J_S$ that (β_1,β_2) acts as a surface current source. A J_x current source (β_1) thus must be used for changes in E_x, and a J_y current source must be used for changes in E_y.

We make some simplifying assumptions at this point in the analysis. We use an isotropic conductivity tensor $(\sigma_{xx}=\sigma_{yy}=\sigma=1/\rho)$ and consider only a current source in the x direction. This means we will only look at changes in E_x.

$$\int_\tau u^* D\Delta v \, d\tau = \int_\tau (\Delta v)\beta^* \, d\tau \qquad (3.4.4)$$

Given that $\beta^* = (\beta_1,0,0,0)$ and $\Delta v=(\Delta E_x, \Delta E_y, \Delta H_x, \Delta H_y)$, equation (3.4.4) reduces to

$$\int_\tau u^* D\Delta v \, d\tau = \int_\tau \Delta E_x \beta_1 \, d\tau \qquad (3.4.5)$$

We want the field change at one point at the surface, $\beta_1 = J_x \delta(z)\delta(x-x_0)\delta(y-y_0)$. Equation (3.4.5) thus becomes

$$J_x \Delta E_x(x_0,y_0,0) = \int_\tau u^* D\Delta v \, d\tau \qquad (3.4.6)$$

where $u^*=(H_y', -H_x', E_y', -E_x')$ due to a point current source at the surface in the x direction. The next step is to compute $D\Delta v$ through the use of the identity, $D\Delta v = -\Delta Dv$.

We use our assumption of conductivity isotropy and equation (3.2.1) to get

$$\Delta Dv = \begin{bmatrix} 0 & 0 & -\frac{\partial}{\partial x}\left(\delta\rho\frac{\partial}{\partial y}\bullet\right) & \frac{\partial}{\partial x}\left(\delta\rho\frac{\partial}{\partial x}\bullet\right) \\ 0 & 0 & -\frac{\partial}{\partial y}\left(\delta\rho\frac{\partial}{\partial y}\bullet\right) & \frac{\partial}{\partial y}\left(\delta\rho\frac{\partial}{\partial y}\bullet\right) \\ 0 & \delta\sigma & 0 & 0 \\ -\delta\sigma & 0 & 0 & 0 \end{bmatrix} \begin{bmatrix} E_x \\ E_y \\ H_x \\ H_y \end{bmatrix} \qquad (3.4.7)$$

We perform this matrix multiplication and make use of the identity from Maxwell's equations that $E_z=(\nabla_s \times H_s)\cdot\hat{i}_z$. Equation (3.4.7) reduces, with these steps, to

$$\Gamma\Delta v = -\begin{bmatrix} \frac{\partial}{\partial x}(\delta\rho\sigma E_z) \\ \frac{\partial}{\partial y}(\delta\rho\sigma E_z) \\ \delta\sigma E_y \\ -\delta\sigma E_x \end{bmatrix} \qquad (3.4.8)$$

We substitute this expression into (3.4.5) and make use of the fact that $u^*= (H_y', -H_x', E_y', -E_x')$ to arrive at the change in a surface E_x due to a conductivity perturbation at depth

$$J_x \Delta E_x(x_0,y_0,0) = -\int_\tau \left[H_y' \frac{\partial}{\partial x}(\delta\rho\sigma E_z) - H_x' \frac{\partial}{\partial y}(\delta\rho\sigma E_z)\right] d\tau \; -$$

$$\int_\tau \delta\sigma(E_x E_x' + E_y E_y') \, d\tau \qquad (3.4.9)$$

The first integral in (3.4.9) is somewhat confusing, since it involves derivatives of perturbations. We will thus reduce this term to a recognizable quantity without any loss of generality. We use the following identities

$$H_y' \frac{\partial}{\partial x}(\delta\rho\sigma E_z) = \frac{\partial}{\partial x}(H_y' \delta\rho\sigma E_z) - \delta\rho\sigma E_z \frac{\partial H_y'}{\partial x} \qquad (3.4.10)$$

$$H_x' \frac{\partial}{\partial y}(\delta\rho\sigma E_z) = \frac{\partial}{\partial y}(H_x' \delta\rho\sigma E_z) - \delta\rho\sigma E_z \frac{\partial H_x'}{\partial y} \qquad (3.4.11)$$

We substitute (3.4.10) and (3.4.11) into (3.4.9), and the first integral in (3.4.9) becomes

$$\int_\tau \left[\frac{\partial}{\partial x}(H_y' \delta\rho\sigma E_z) - \frac{\partial}{\partial y}(H_x' \delta\rho\sigma E_z)\right] d\tau - \int_\tau \delta\rho\sigma E_z \left(\frac{\partial H_y'}{\partial x} - \frac{\partial H_x'}{\partial y}\right) d\tau \qquad (3.4.12)$$

We expand the volume, τ, to include an outer region where there are no conductivity perturbations. The first integral in (3.4.12) is an integral over the volume of perfect differentials. This first term will reduce to a surface integral over surfaces bounding the volume. The volume has been expanded to include the outer region, however, so $\delta\rho=0$ on the surface bounding the volume. The first integral in (3.4.12) is therefore zero. We again make use of the identity $E_z = (\nabla_s \times H_s)\cdot\hat{i}_z$ and simplify the second integral of (3.4.12). Equation (3.4.9) thus reduces to

$$J_x \Delta E_x(x_0, y_0, 0) = -\int_\tau \delta\sigma (E_x E_x' + E_y E_y') \, d\tau + \int_\tau \delta\rho\sigma^2 E_z E_z' \, d\tau \qquad (3.4.13)$$

We have one integral involving $\delta\sigma$ and one involving $\delta\rho$ in (3.4.13). The relationship between $\delta\rho$ and $\delta\sigma$ can be

derived by expanding $1/(\sigma+\delta\sigma)$ and equating to $\rho+\delta\rho$. This procedure yields

$$\delta\rho \approx -\delta\sigma/\sigma^2 \qquad (3.4.14)$$

We substitute (3.4.14) into (3.4.13) to get the total change in E_x due to conductivity perturbations

$$J_x \Delta E_x(x_0,y_0,0) = -\int_\tau \delta\sigma(E\cdot E')\, d\tau \qquad (3.4.15)$$

The sensitivity of E_x to a given conductivity perturbation is

$$\frac{\partial E_x(x_0,y_0,0)}{\partial\sigma(x,y,z)} = -\frac{E(x,y,z)\cdot E'(x,y,z)}{J_x} \qquad (3.4.16)$$

Note that E' is the solution to the normal problem with a delta function source in the x direction at $(x_0,y_0,0)$, while E is the solution to the normal problem with a uniform current sheet.

We see a logical progression in the source complexity as we move from the 1-D inversion to the 3-D inversion. Fields vary as a function of depth only in the 1-D problem, so sources were uniform current sheets. Fields vary as a function of depth and one horizontal coordinate in the 2-D problem, so line sources are needed. Point sources are necessary in the 3-D case because fields are functions of all three spatial coordinates.

3.5 Summary

We have presented the theoretical groundwork for the 3-D inversion problem in this chapter. The inversion procedure is based upon the method of forward modelling in Chapter 2. We used the adjoint problem solution and generalized reciprocity theorem (Lanczos, 1956) to determine the surface field perturbation due to a conductivity change at some point in the subsurface. We demonstrated that these conductivity changes at depth in the normal problem are equivalent to surface current sources for the adjoint problem. Finally, we compared the 3-D inversion to an analytic 1-D linearized inversion scheme and shown they are equivalent.

'But do the data fit with our preconceived notion of what is going on?'

Geophysics Field Teaching Assistant

CHAPTER 4

4.1 Introduction

We present in this section an interpretation of magnetotelluric data from a geothermal area. We use the insights developed in Chapter 2 to guide our interpretation of these data. We also use 3-D modelling to examine the effect of truncating a 2-D body along its strike. We finally make some recommendations regarding the planning of an MT survey.

4.2 Geology and Previous Geophysics

The magnetotelluric data were collected in Whirlwind Valley by Geotronics Corporation for Chevron Resources Company. These data were released under a joint industry-Department of Energy exploration program for geothermal energy. Whirlwind Valley is located in north central Nevada approximately 30 kilometers due east of Battle Mountain. Whirlwind Valley is the site of the Beowawe Known Geothermal Resource Area (KGRA).

Figure 4.2.1 is a generalized geologic map compiled from Roberts, et. al. (1967) and from Stewart, et. al. (1977). The following discussion of the geology is also taken from these two references, unless otherwise indicated. Nevada was the site of a north-south geosyncline during the early Paleozoic era. Most of the rocks deposited in central Nevada were carbonate rocks, while a siliceous and volcanic assemblage was deposited in western Nevada. The siliceous assemblage, which included chert, shale, siltstone, and some volcanic beds, was thrust eastward over the carbonate assemblage during the Antler orogeny in the late Paleozoic era. Rocks forming the siliceous assemblage are shown in Figure 4.2.1 as Paleozoic sediments. The easternmost evidence of this thrust plate is about 50 kilometers east of Whilrwind Valley.

The next major geologic activity in this area occurred in the Cenozoic era. The Basin and Range structure now

present began developing in the Miocene or Pliocene period. Concurrently, a NNW trending rift zone developed in the area (Stewart, et. al., 1975). The eastern edge of this rift zone is the Dunphy Pass fault zone, which is the NNW trending fault bisecting Whirlwind Valley (Smith, 1979). The rift zone is characterized by numerous diabase dikes and basaltic andesite flows (Stewart, et. al., 1975). The andesite flows are shown in Figure 4.2.1 as Tertiary volcanic rocks.

The andesite flows which crop out around Whirlwind Valley thicken from west to east until the eastern edge of the rift zone is reached (Smith, 1979). The flows thin dramatically across the fault to about 100 meters thick (Smith, 1979). Outcrops of the underlying Paleozoic sediments can be seen along the southern edge of Whirlwind Valley east of the Dunphy Pass fault zone. A well drilled near MT Site 3 (Figure 4.2.2) shows 50 meters of valley fill over 1.3 kilometers of volcanic rocks (Chevron Resources Company, 1975). At least 1.5 kilometers of Paleozoic sediments underly the volcanic flows. The ENE trending fault bounding Whirlwind Valley to the south forms the Malpais rim scarp (Smith, 1979). The valley has been dropped down relative to the outcrops south of Malpais rim. Smith (1979) proposes that the Geysers (Figure 4.2.2) occur near the intersection of the Malpais rim fault and the Dunphy Pass fault zone because this intersection provides a

conduit for hot water to reach the surface.

The Beowawe KGRA has been the subject of many geophysical investigations, so we will only discuss those surveys relevant to our interpretation. Figure 4.2.2 is a location map for two of these surveys. The gravity contours are taken from Erwin (1974), and represent the complete Bouguer anomaly. The resistivity lines are from Smith (1979) and consist of dipole-dipole soundings using 600m dipoles. The 11 MT sites shown comprise the survey we interpret here.

The gravity data are needed to estimate the basin depths in Boulder, Whirlwind, and Crescent Valleys. Erwin (1974) estimates 500 meters of Cenozoic sediments are needed to explain the gravity anomaly in Boulder Valley. This assumes a density contrast of 0.4 g/cc. We estimate Whirlwind Valley has a maximum thickness of 150 meters of Cenozoic sediments assuming this same density contrast, and Crescent Valley has sediments 300-500 meters thick.

The resistivity data collected by Smith (1979) shows several striking features. A 10-15 Ω-m conductive body can be seen at depths from 300 meters to 1500 meters which follows the Malpais rim fault. This feature extends eastward from the Dunphy Pass fault for 12 kilometers, and is 2 kilometers wide. The background resistivity is 50-100 Ω-m. Further, the resistivities of the sediments filling Whirlwind Valley and the outcropping Tertiary volcanic

rocks are the same.

The final geophysical survey with applications to this interpretation is an aeromagnetic survey of north central Nevada. This map, presented by Stewart, et. al. (1975), shows a very prominent magnetic anomaly with a NNW strike direction. This feature is approximately 120 kilometers long and is about 18 kilometers wide where it crosses Whirlwind Valley. The anomaly's northeastern edge corresponds with the Dunphy Pass fault zone. Stewart, et. al. (1975) attribute this anomaly to highly magnetic, vertically emplaced diabase dikes associated with the rift zone and andesite flows.

Figure 4.2.1--Geologic Map of Beowawe, Nevada

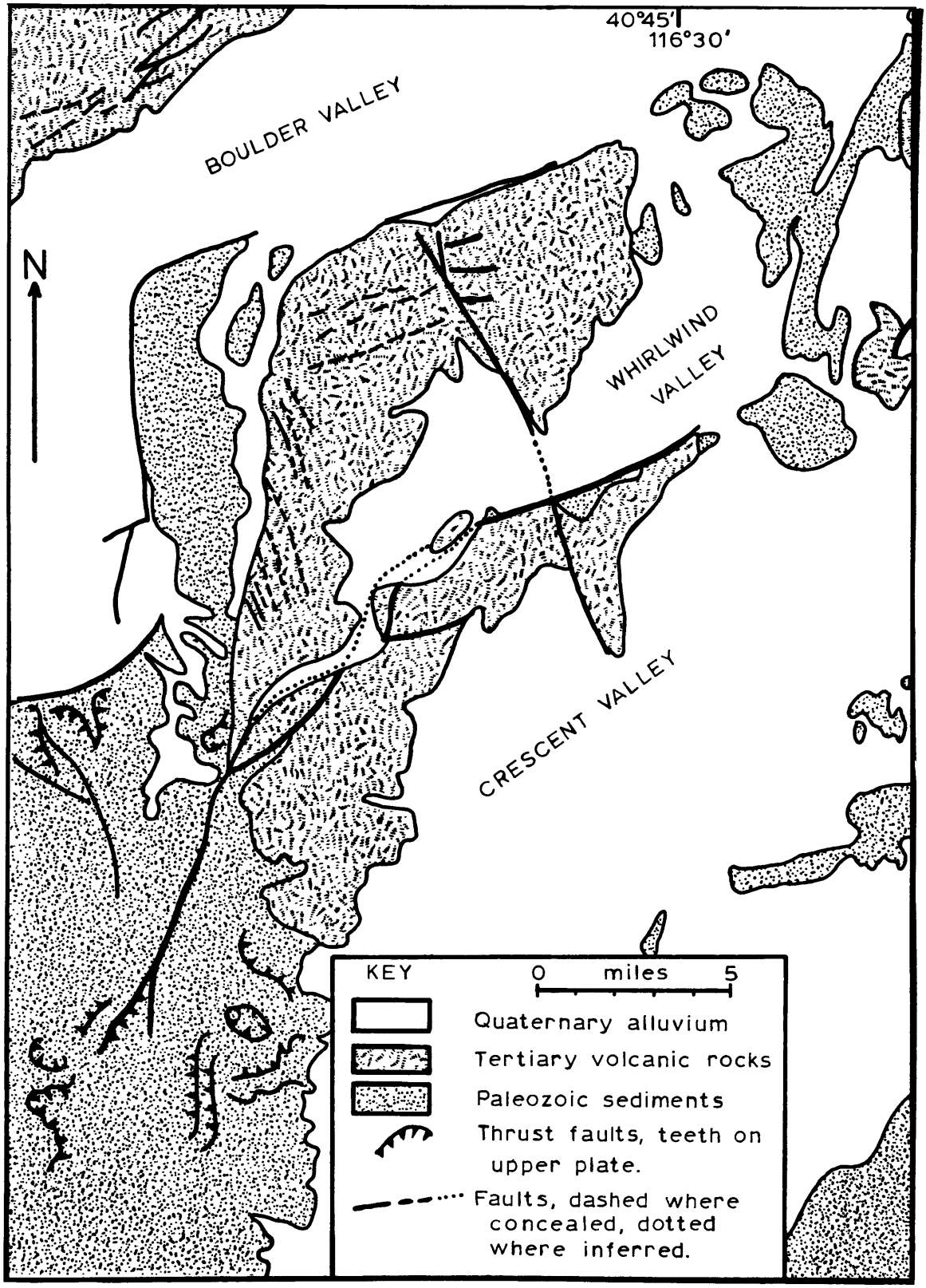
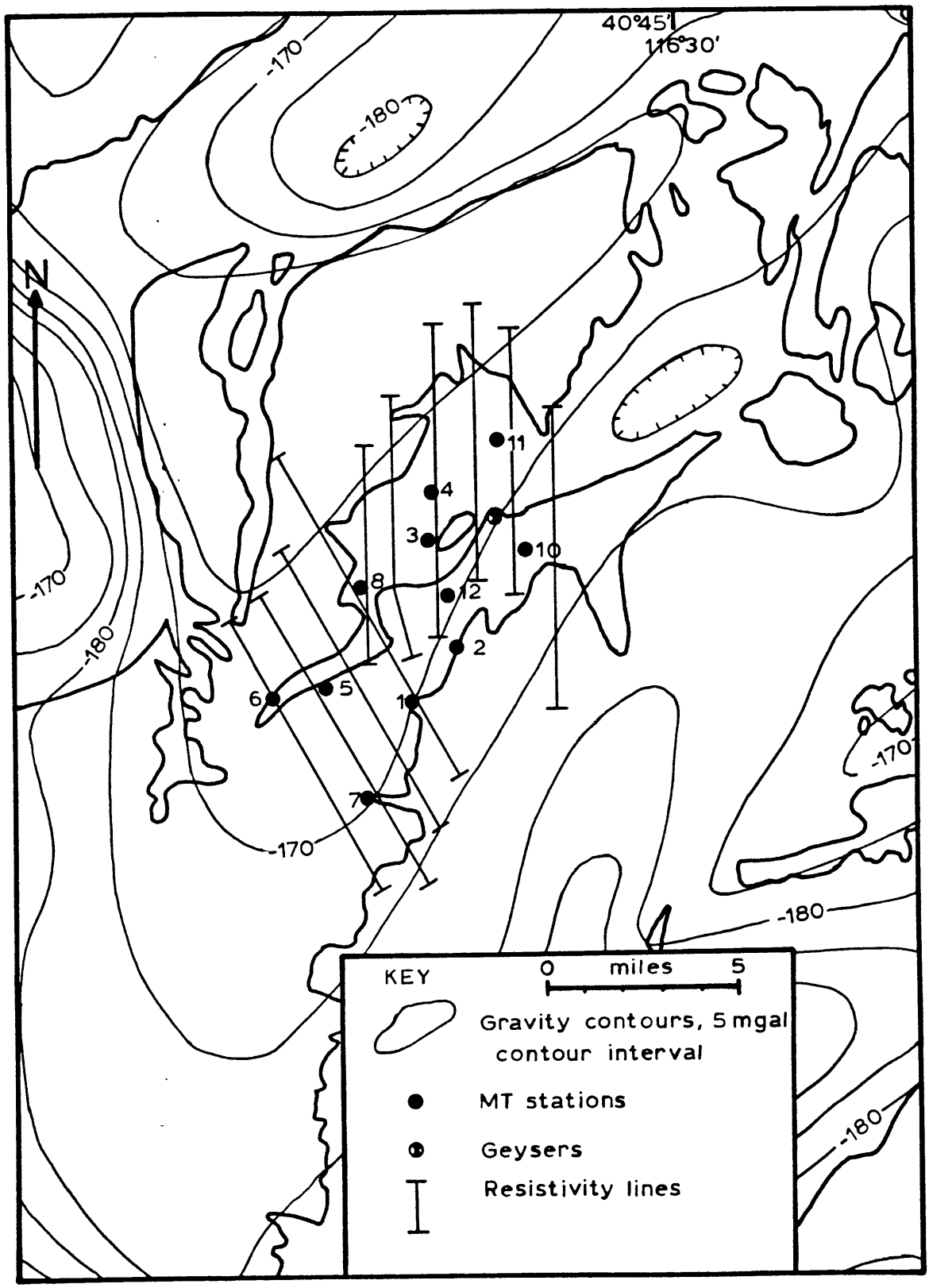


Figure 4.2.2--Geophysical Investigations of Beowawe, Nevada



4.3 MT Interpretation

The locations of the 11 MT sites in this survey are shown in Figure 4.2.2. Site 9 was not used because of errrors in the raw power spectra. Raw power spectra were processed using the method in Appendix C to produce the sounding curves for Sites 1 through 12 (Figures 4.3.1 to 4.3.11, respectively). Rotation angles for these sites are presented in Figures 4.3.12 through 4.3.15. The rotation angle is measured from north towards east, and all of the sites show that the maximum apparent resistivities lie in the NE direction. The data presented here are results from reprocessing the survey. The original processing also yielded tipper directions. The tipper direction is an indicator of the regional current flow, and is derived from measurements of the vertical magnetic field. The tipper directions at these sites show a consistent NW trend for the current flow. Maximum skews and ellipticities for these sites are less than 0.3 (out of 1.0), and typical values are 0.1 or less. The variation in skews and ellipticities appear to be a function of data quality rather than of structure.

Proprietary MT data (Chevron Resources Company) in Crescent Valley resemble our data quite closely. The structure responsible for the low frequency split in the apparent resistivity curves thus appears to extend southeast into Crescent Valley. We infer from this observation, the

aeromagnetic anomaly, and the low skews and ellipticities that the structure beneath Whirlwind Valley is essentially two-dimensional. We will later address the question of how 2-D the stucture must be. This conclusion, and the following qualitative interpretation, was also reached by Swift (1979).

We have an apparent contradiction presented by these data. The tipper directions indicate the current flow is NW-SE, but the maximum apparent resistivity is NE-SW. This resistivity is really just a measure of electric field strength, so the maximum resistivity direction usually indicates the maximum current flow direction. These two direction indicators thus should agree, if the body has isotropic conductivity. We infer from this discrepancy in directions that the body has anisotropic conductivity. The observed behavior can be explained with a structure that is conductive in the NW direction and resistive in the NE direction. This anisotropy is not an intrinsic material property-- it is a result of inhomogeneous structure on a 'fine' scale. Further, it is reasonable if we consider the geologic structure at depth. We have vertically emplaced resistive dikes intruding into conductive sediments. The dike swarm has a NNW strike direction. Current flow along strike would not be impeded because channels of conductive sediment would exist. Across strike however, the structure would appear resistive because the dikes would block

current flow.

Evidence of current entrapment in the upper crust is also present in the data. The maximum apparent resistivity increases as the frequency decreases at Sites 5, 6, 7, and 8 in the frequency range .01-1 Hertz. This increase is approximately proportional to 1/f. The apparent resitivity is

$$\rho_a \propto |Z|^2/f \qquad (4.3.1)$$

We see immediately that this 1/f proportionality in ρ_a implies $|Z|$, or $|E/H|$, is roughly constant in this frequency band. The current is not escaping into the mantle at the lower frequencies, or the impedance would decrease. We infer from this observation that the lower crust must be resistive in order to trap the current in the upper crust. This conclusion differs with that of Swift (1979) about the lower crust.

Our model should qualitatively consist of a buried sturcture with a NW to NNW strike direction underlain by a resistive lower crust. The structure should be conductive along strike and resistive across strike. All sites show that the near-surface is resistive, but that a conductive layer exists between the top layer and the anisotropic body. This structure is indicated by the decrease of both maximum and minimum apparent resistivities as frequency decreases in the range 1-100 Hertz.

Several sites, such as Sites 1 and 2, show significant anisotropy in the surface resistivity structure. This anisotropy is indicated by the separation of the maximum and minimum apparent resistivity curves at the highest frequencies. This anisotropy is again not intrinsic, but rather is due to heterogeneous structure. We know from the results in Chapter 2 that variations in surface resistivity produce parallel shifts of the whole sounding curve. We can thus correct for these surface variations by shifting the high frequency portions of the sounding curves to some 'standard' curve. This 'standard' curve was chosen using Sites 3, 4, and 12. These sites show little to no surface anisotropy and have very similar high frequency behavior. This 'standard' curve represents the average structure at the surface over the whole survey.

Figure 4.3.16 shows all the sounding curves after the high frequency portions of the curves have been shifted to the 'standard' curve. This has the effect of stripping off the surface heterogeneities and allowing us to look at variations at depth. We have plotted the sites together to emphasize their similarities. Sites 5 and 7 have a different surface resistivity structure--the surface resistor is missing. These two sites thus could not be shifted to the 'standard' curve.

Several features are visible in Figure 4.3.16. The minimum apparent resistivity curves are all within a factor

of 3 of one another. Maximum apparent resistivity curves for Sites 1, 2, 3, 4, 10, 11, and 12 all cluster within a factor of 3 also. Maximum apparent resistivity curves for Sites 5, 6, 7, and 8 are almost identical, although Sites 5 and 7 are suspect because of the different surface structure. We see from Figure 4.2.2 that these two clusters of sites lie in different geographic locations. Sites 1, 2, 3, 4, 10, 11, and 12 lie close to the Dunphy Pass fault zone, while Sites 5, 6, 7, and 8 lie about 7 kilometers southeast of the first group. We basically have just two generalized MT sites in this survey because of the lack of areal distribution. The first is located 3 kilometers from the Dunphy Pass fault zone, and the second is about 10 kilometers from the zone. These two sites are shown in Figure 4.3.17 and labelled Sites 1 and 2. These are the sites we will interpret. The actual data sites will require small perturbations in the structure derived from the generalized sites.

We use both 2-D and 3-D modelling programs with a 2-D structure to fit the generalized sites shown in Figure 4.3.17. The vertical resistivity in our dike model is identical to the horizontal resistivity along strike. We used the 2-D program to model the anisotropy simply by assigning different resistivities for the parallel and perpendicular polarization cases. This method unfortunately varies the vertical resistivity for the two polarizations,

which is incorrect. The vertical resistivity is only important at frequencies where current flow from the mantle is significant, however. Errors will only occur, then, at the lower frequencies. We use the 3-D program at the lower frequencies because it uses anisotropic conductivities. The sounding curves from the 2-D program, valid at intermediate to high frequencies, are merged with those from the 3-D program at low frequencies. The fits to the data curves shown in Figure 4.3.17 and Figures 4.3.19-4.3.21 have been generated in this manner.

Figure 4.3.17 shows an example of a good fit. The cross-section of the 2-D model used to produce this fit is presented in Figure 4.3.18. We see all the essential elements of our qualitative interpretation present in Figure 4.3.18. The resistivity of the body is highly anisotropic, but this may be reasonable. The highest degree of anisotropy is seen where the resistivity along strike is .3 Ω•m and the resistivity across strike is 200 Ω•m. This anisotropy can be produced by mixing dikes with an intrinsic resistivity of 1000 Ω•m with conductive sediments with an intrinsic resistivity of .25 Ω•m. The required mix consists of 20% dikes and 80% sediments.

Figures 4.3.19-4.3.22 represent a crude sensitivity analysis of the model shown in Figure 4.3.18. We observe changes in the apparent resistivity curves as various parameters in the model are perturbed. Figure 4.3.19

contains examples of perturbations in the near-surface resistivity structure. None of these curves have the inflection point at 5 Hertz that the data curves show, although increasing the resistivity of the second layer to 20 Ω•m is close. Overall, the response is very sensitive to the surface resistivity structure, so that little variation may occur.

Figure 4.3.20 shows how variations in the resistive lower crust change the sounding curves. The most striking change occurs when varying the thickness of the lower crust. Thinning the crust by 30% shifts the inflection point on the maximum apparent resistivity curve for Generalized Site 2 by 1/3 frequency decade. Thickening the lower crust by 30% also shifts the inflection point, but by much less. However, the level of the maximum curve at Generalized Site 2 is too low for the thicker crust. The thickness of 24 kilometers for the lower crust is thus probably good to within 10%. Increasing the resistivity by one order of magnitude has a negligible effect on the sounding curves. We can only conclude that the lower crust is resistive (greater than 1000 Ω•m), but cannot say how resistive.

Figure 4.3.21 presents the effects of changing the resistivities of the 2-D body across strike. Only the maximum curves for the generalized sites are shown. We again see the maximum sounding curves are relatively

sensitive to changes in these resistivities. Note that varying the resistivity beneath generalized site 2 does not greatly affect the maximum curve at generalized site 1, and vice versa. These parameters are independent of one another. We conclude that the 23 Ω•m value is good to within 50% and the 200 Ω•m value is good to within 30%. Figure 4.2.22 illustrates the effect of varying the resistivity of the 2-D body along strike. Only the minimum curves for the generalized sites are shown in this figure. We conclude from Figure 4.2.22 that the resistivity along strike is less than 1 Ω•m in the most conductive portion of the body.

Figure 4.3.1--Beowawe MT Site 1

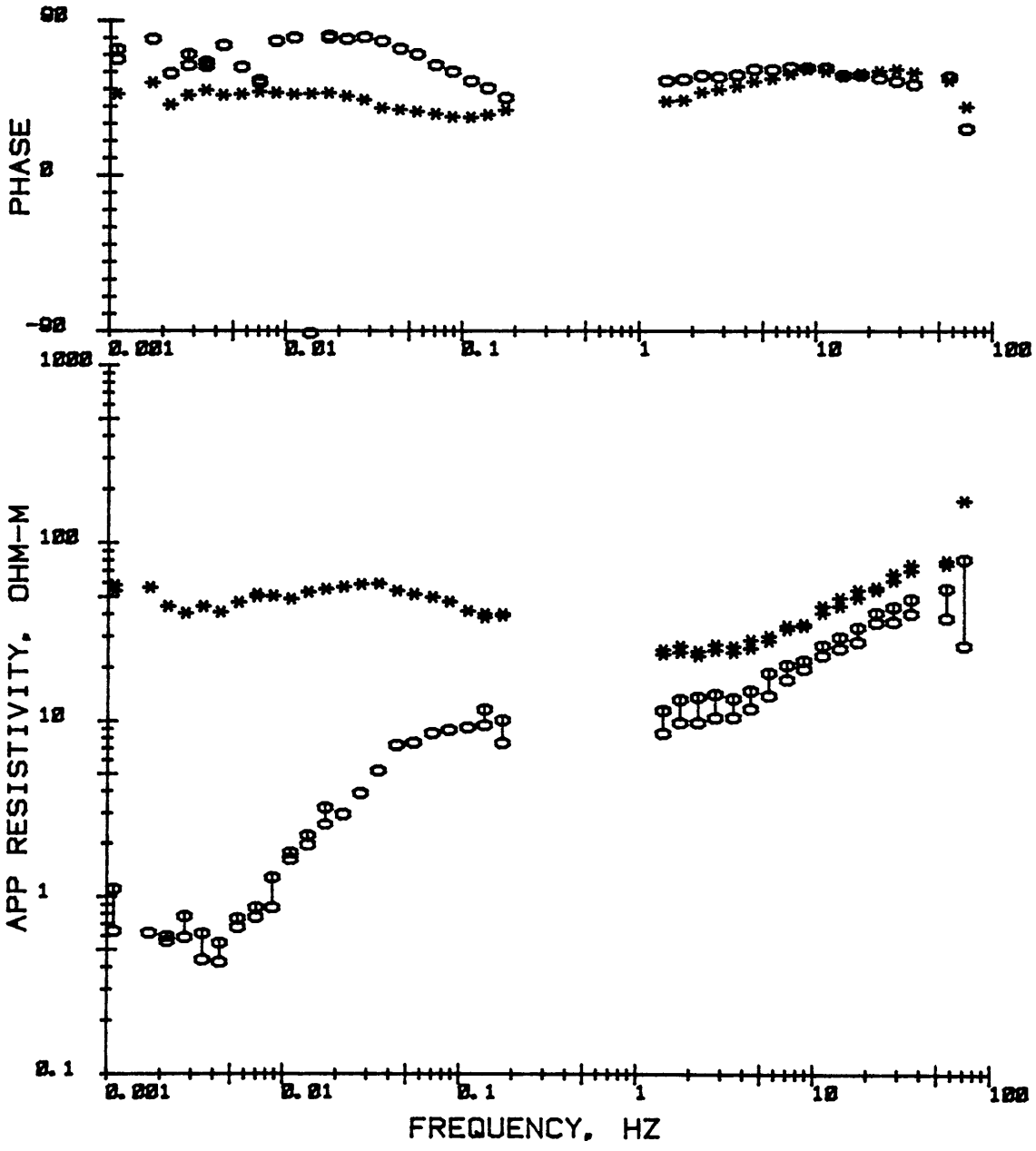


Figure 4.3.2--Beowawe MT Site 2

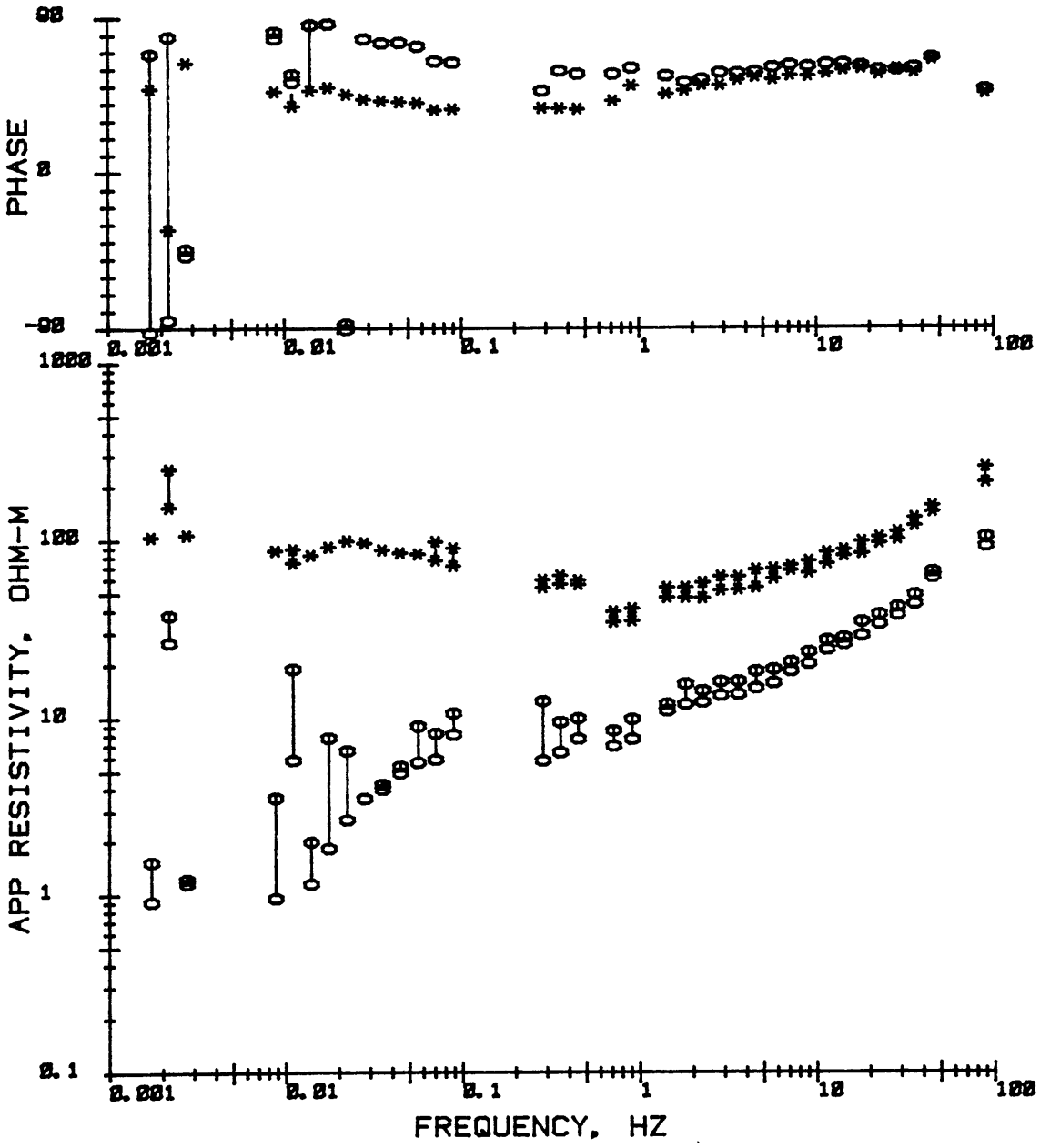


Figure 4.3.3--Beowawe MT Site 3

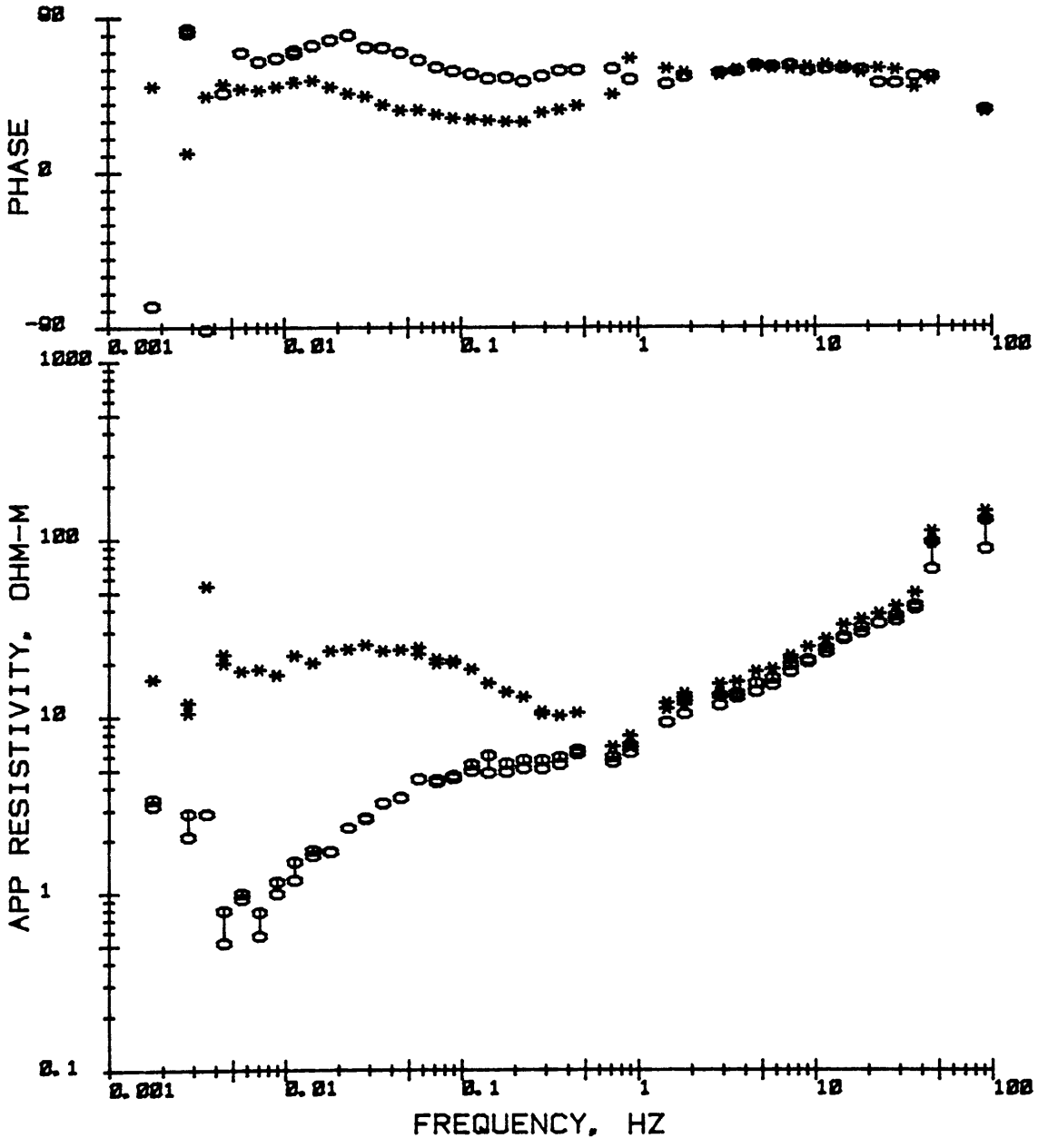


Figure 4.3.4--Beowawe MT Site 4

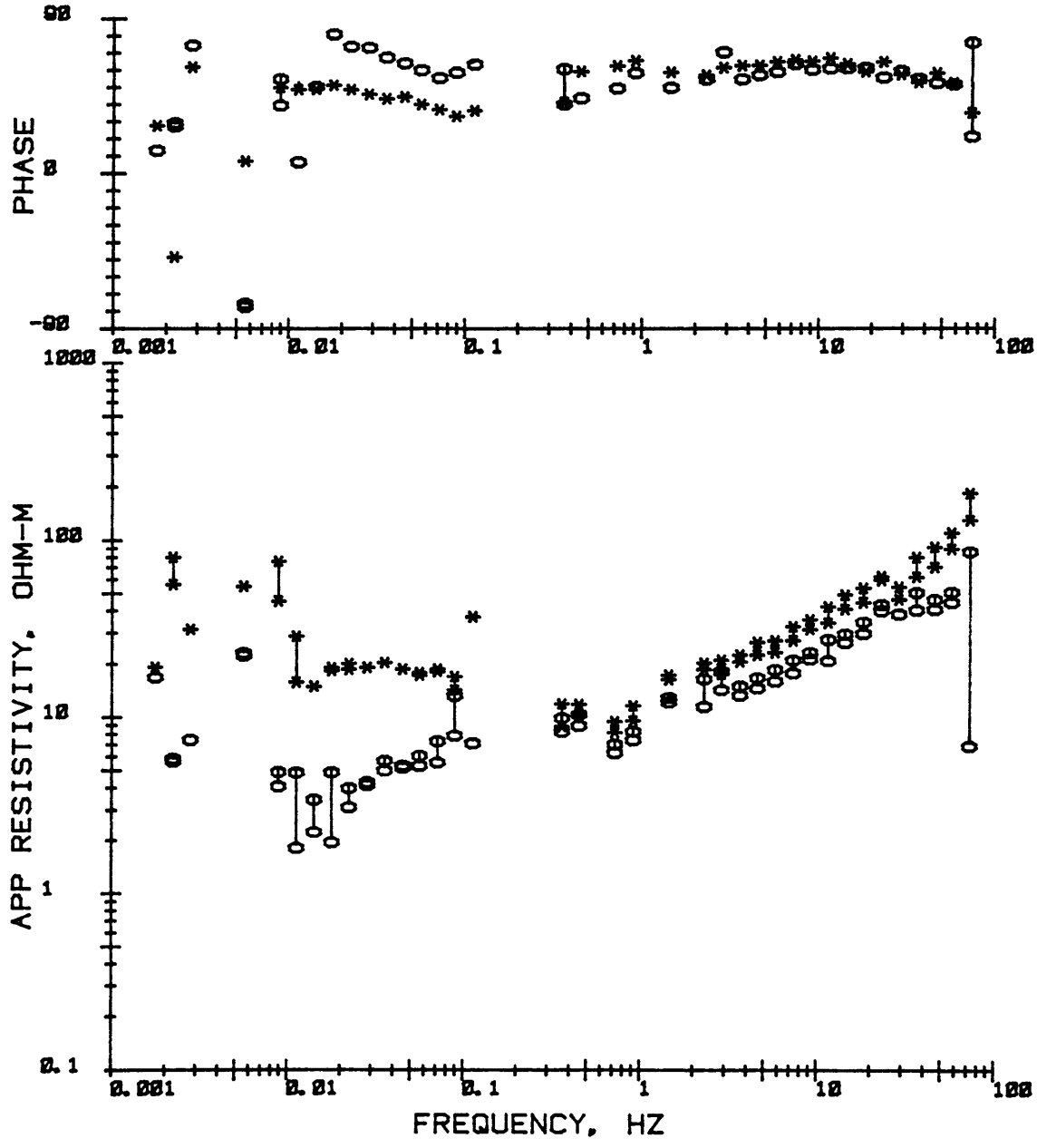


Figure 4.3.5--Beowawe MT Site 5

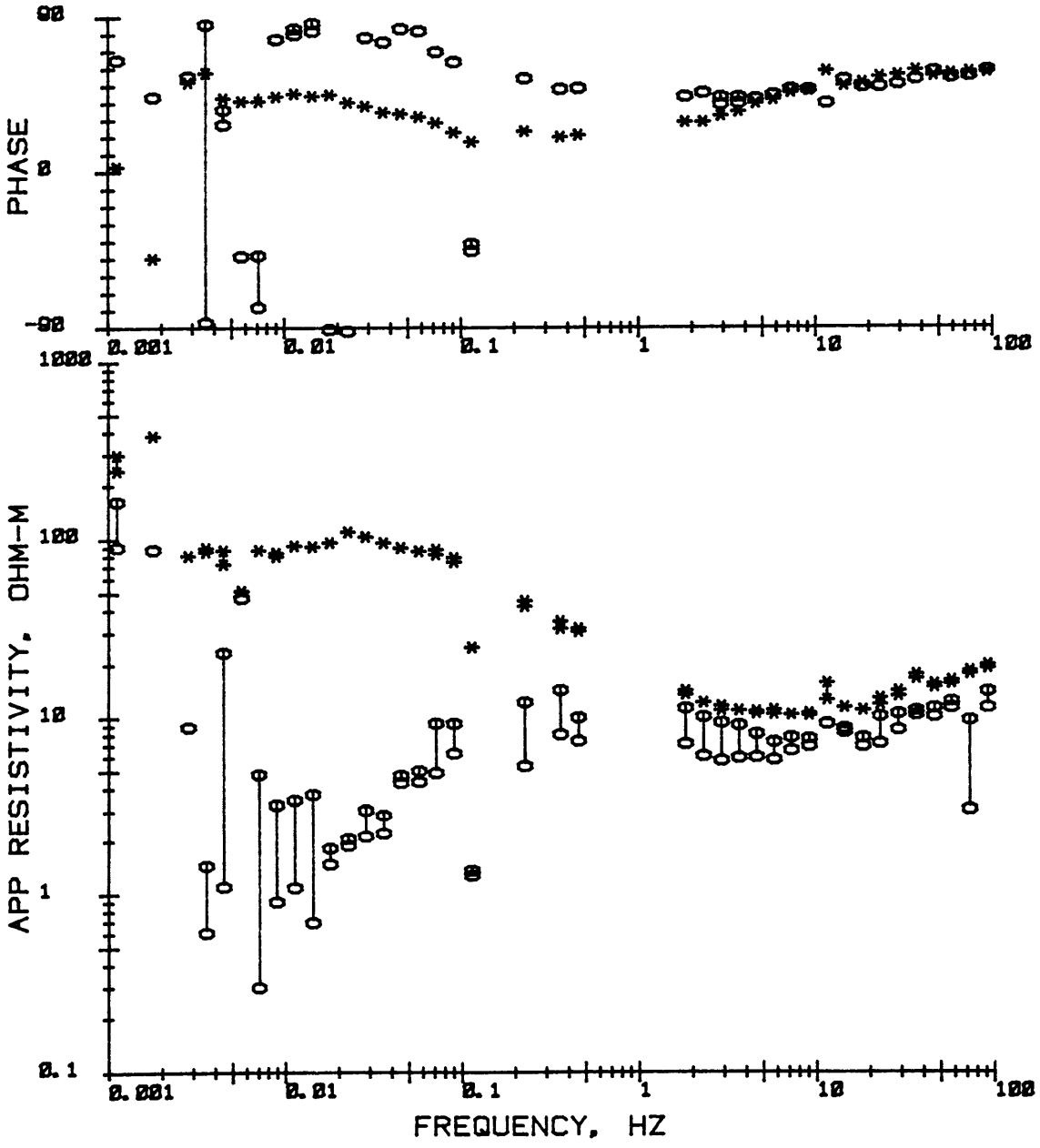


Figure 4.3.6--Beowawe MT Site 6

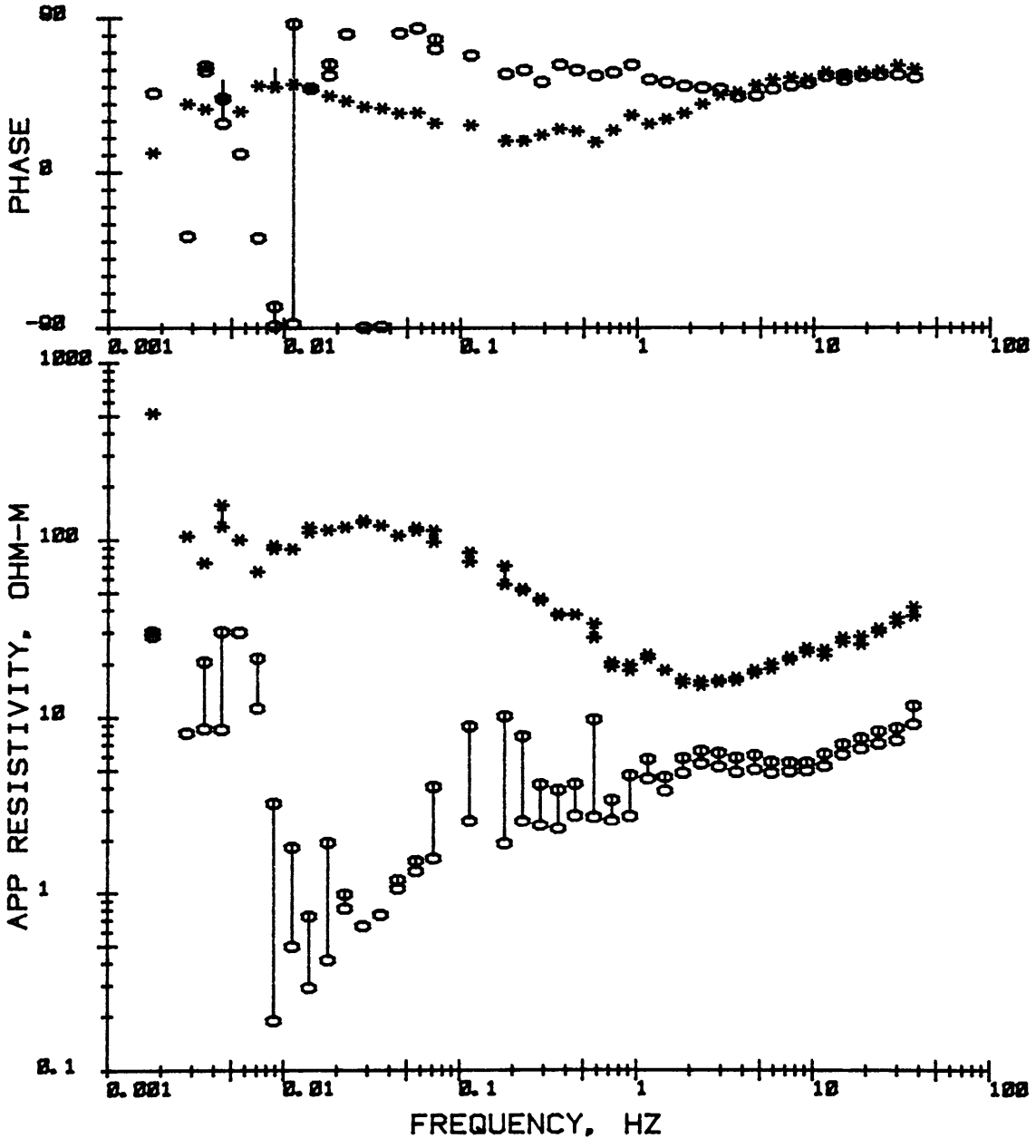


Figure 4.3.7--Beowawe MT Site 7

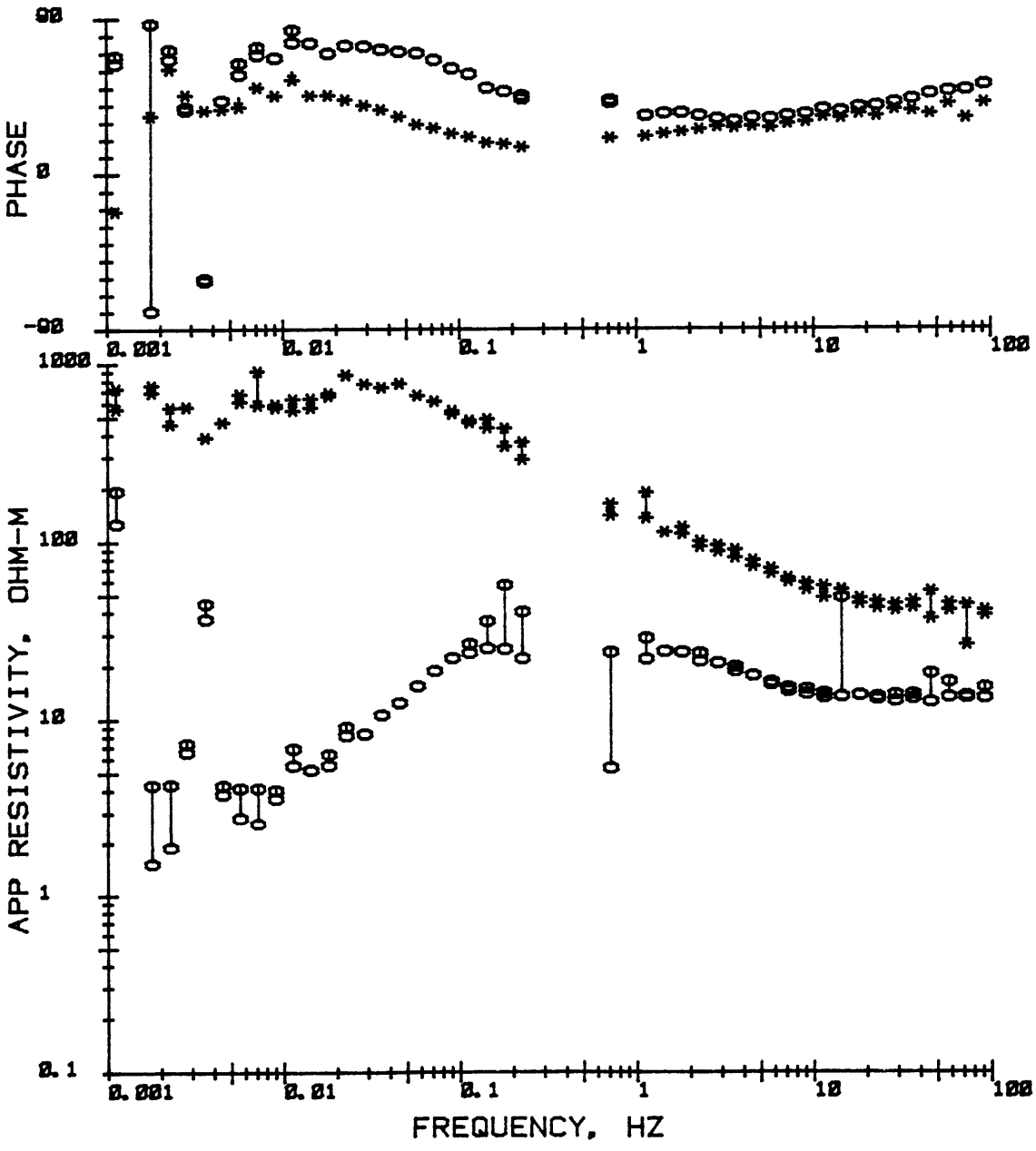


Figure 4.3.8--Beowawe MT Site 8

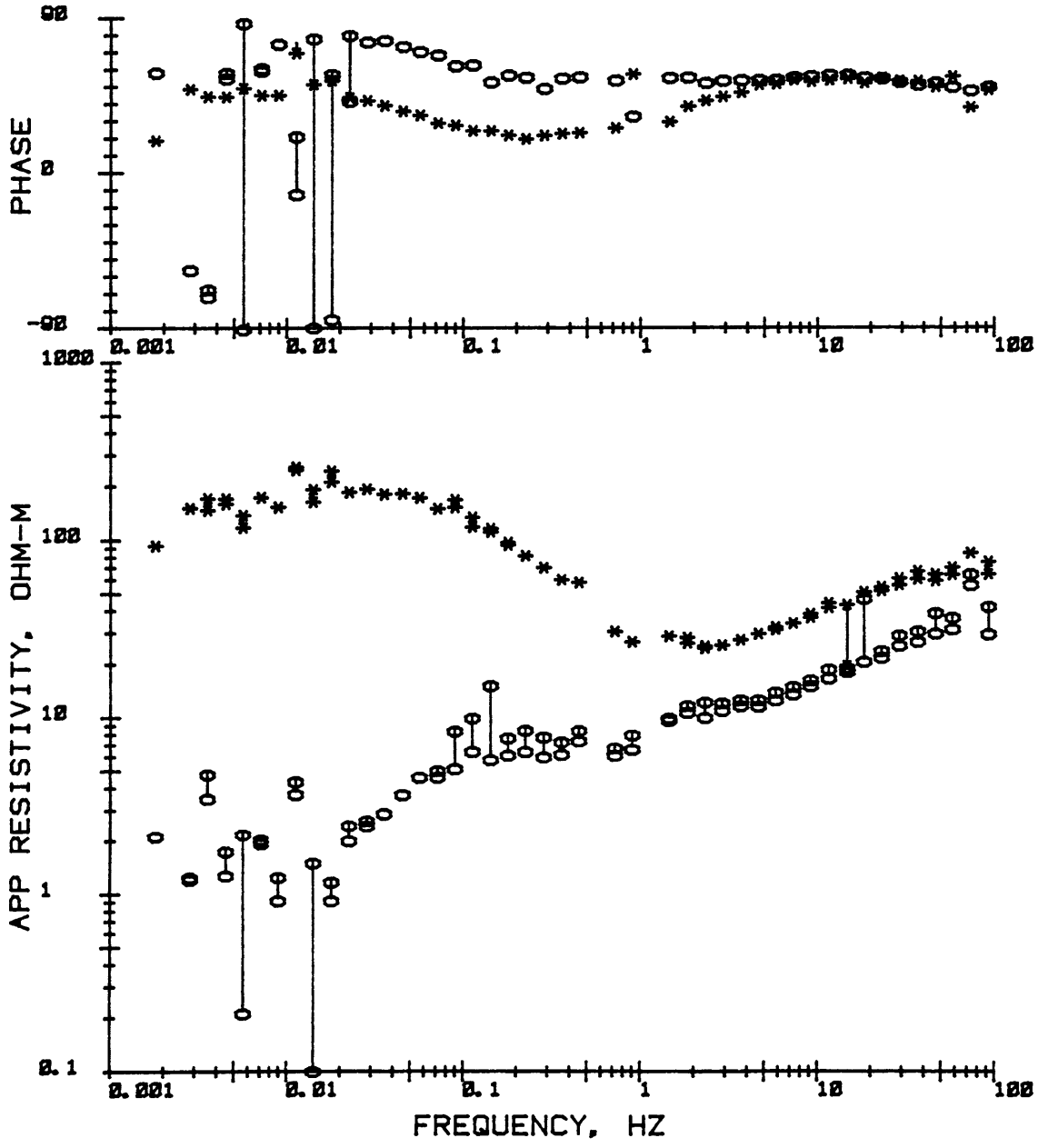


Figure 4.3.9--Beowawe MT Site 10

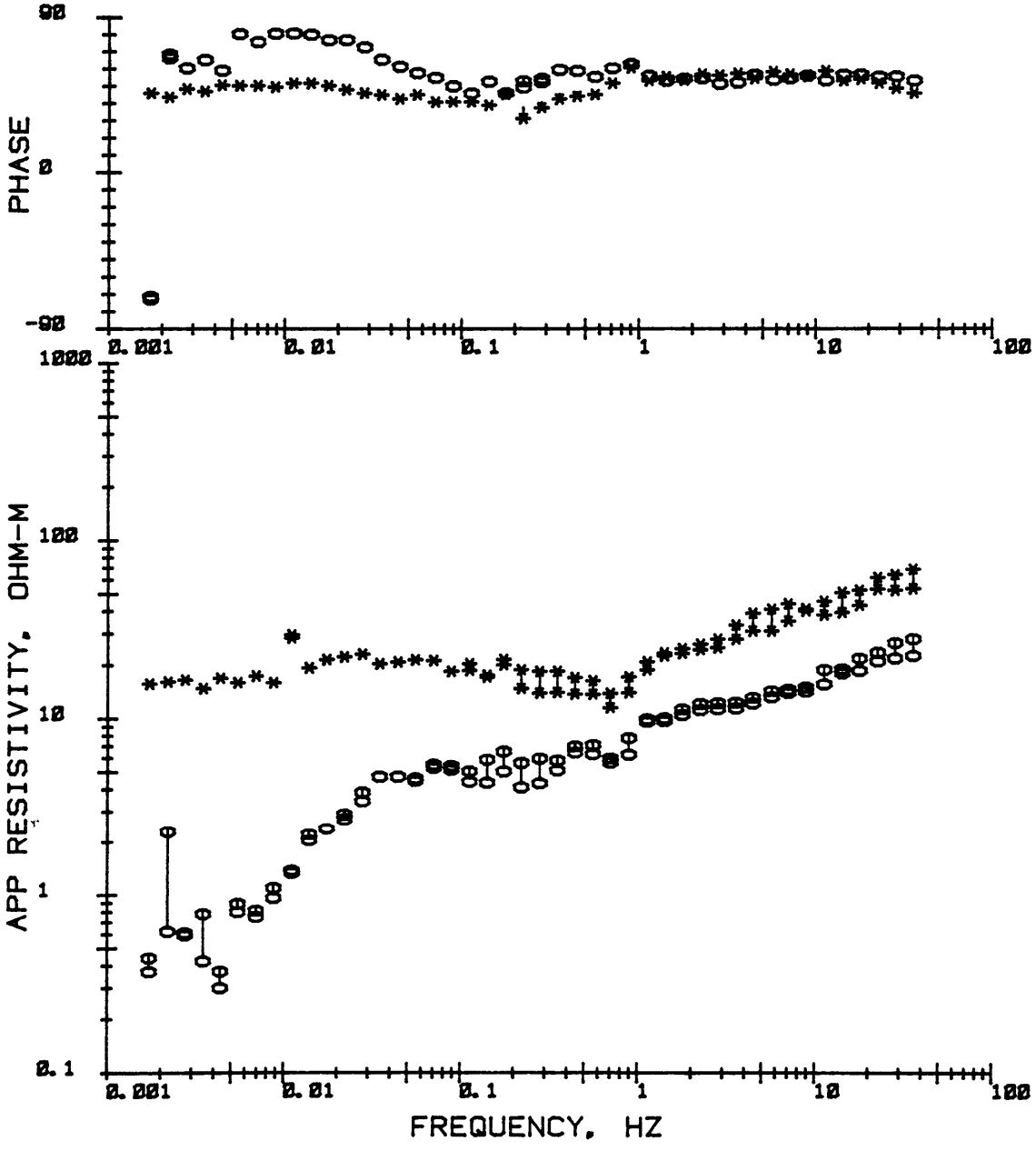


Figure 4.3.10--Beowawe MT Site 11

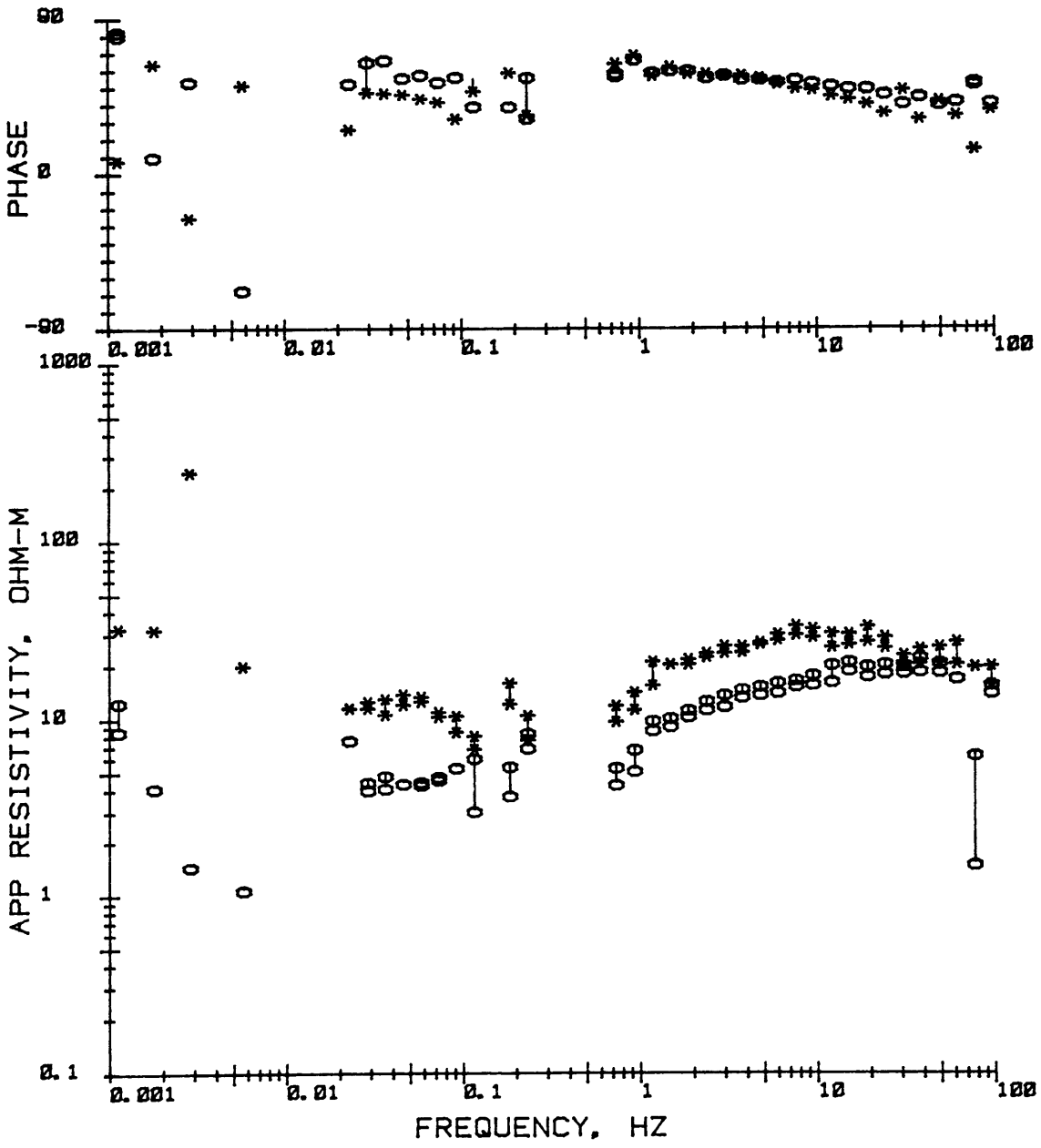


Figure 4.3.11--Beowawe MT Site 12

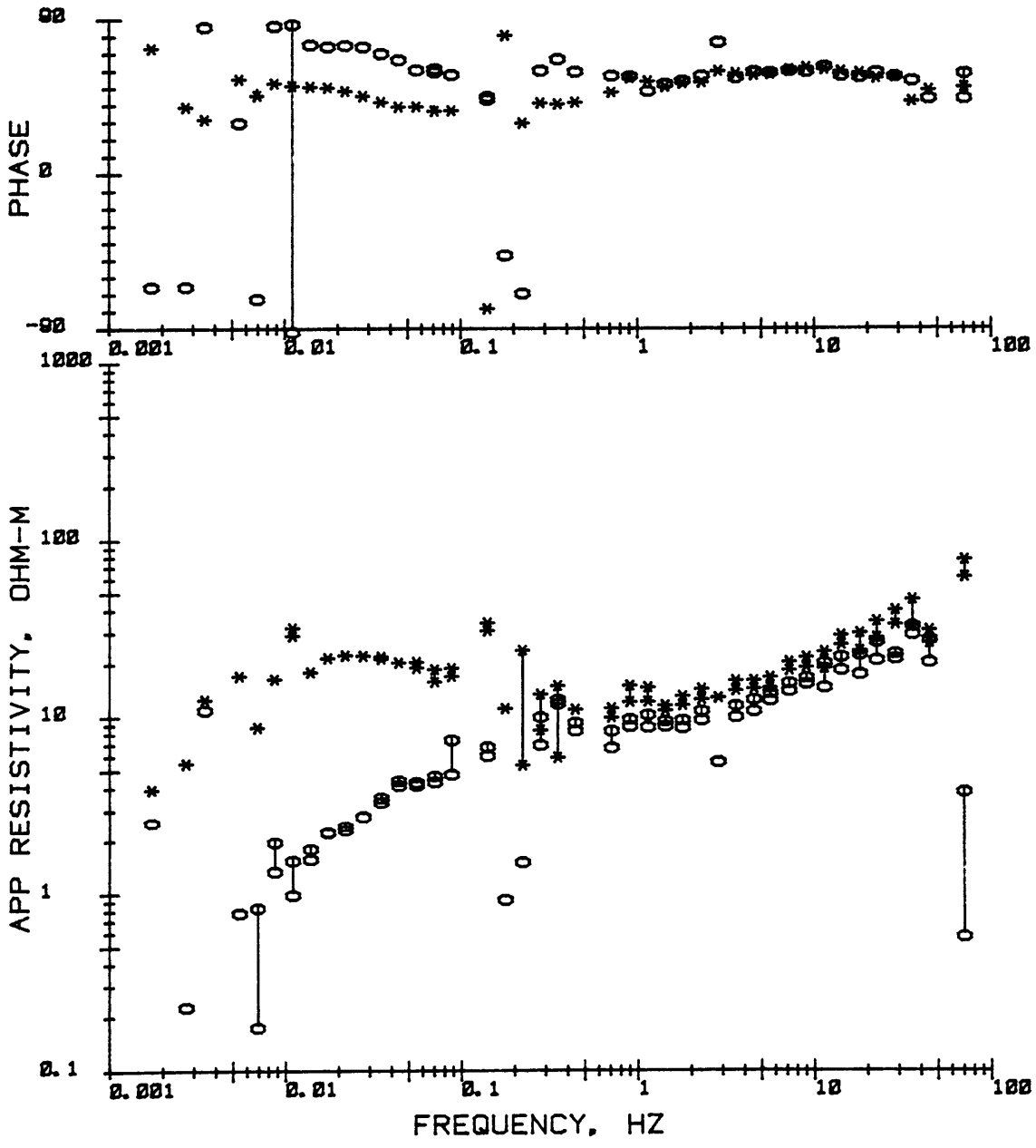


Figure 4.3.12--Rotation Angles for Sites 1-3

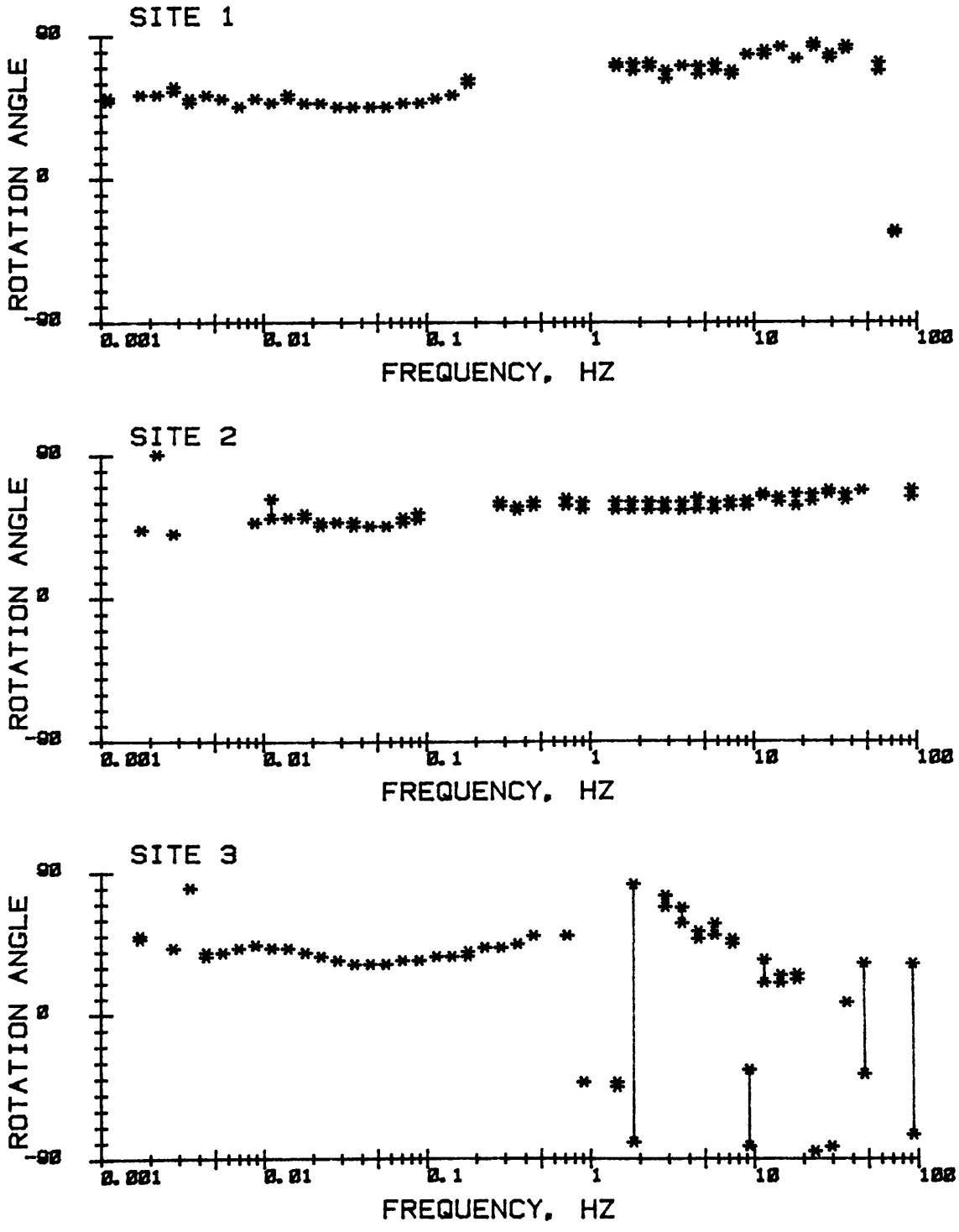


Figure 4.3.13--Rotation Angles for Sites 4-6

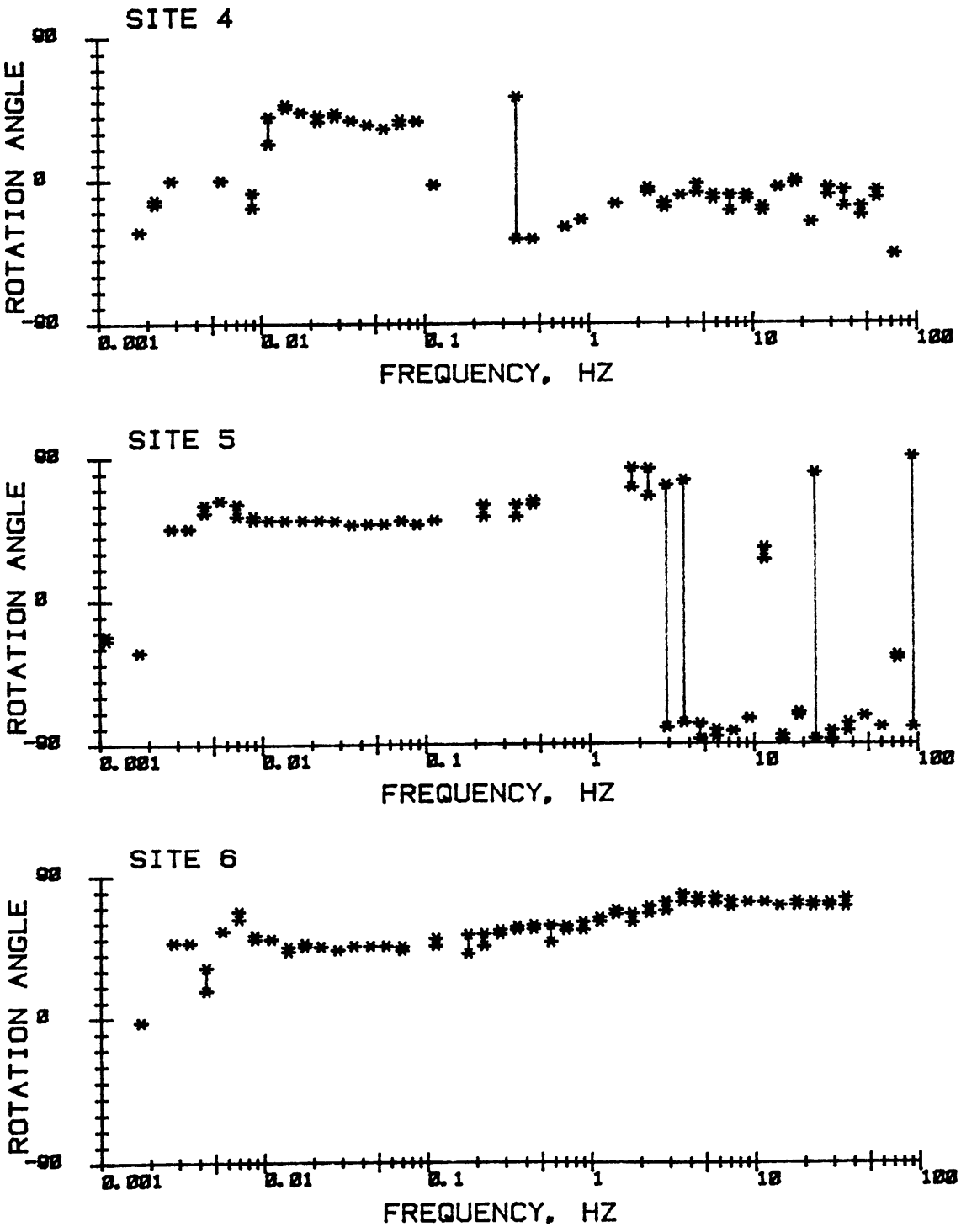


Figure 4.3.14--Rotation Angles for Sites 7-10

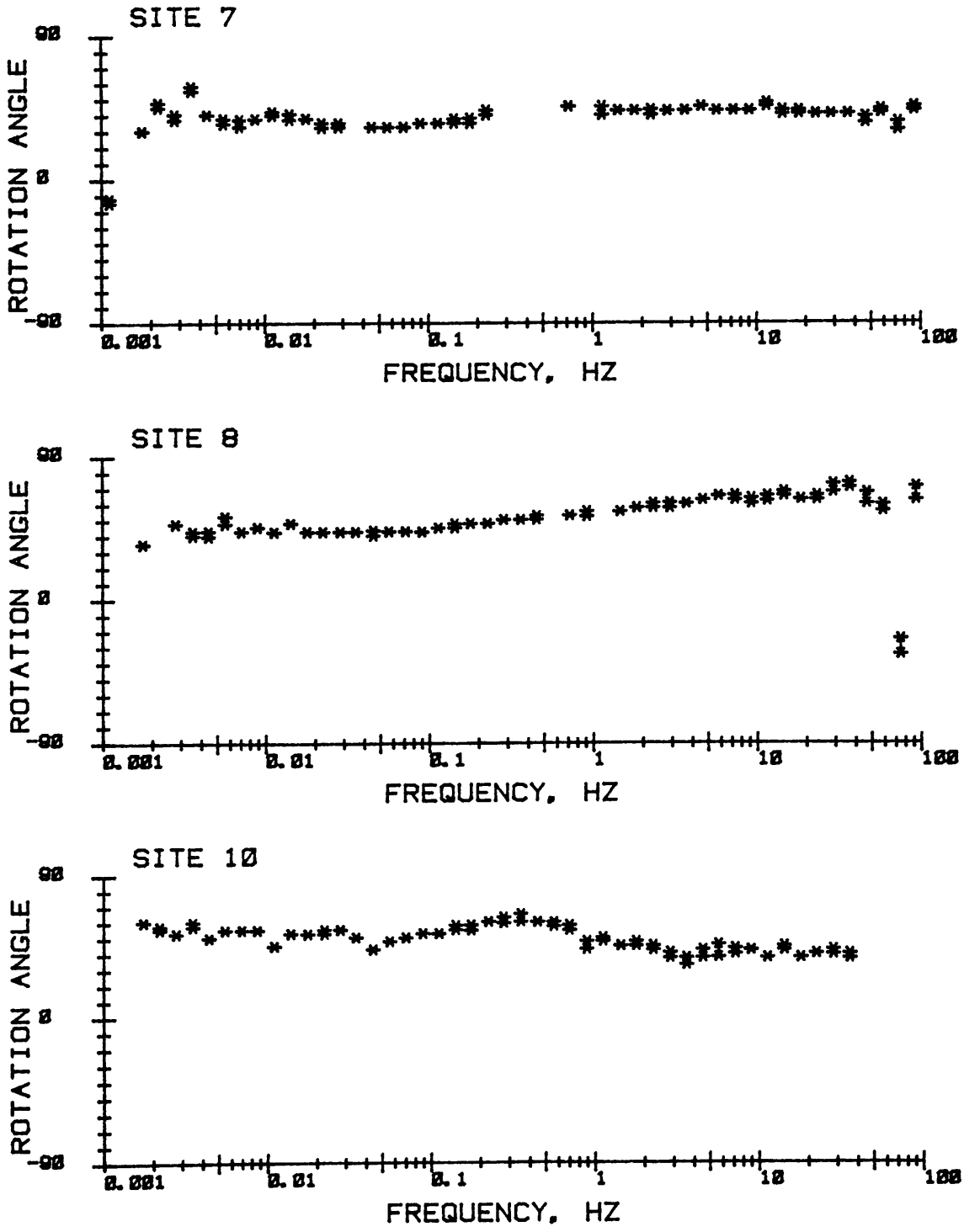


Figure 4.3.15--Rotation Angles for Sites 11-12

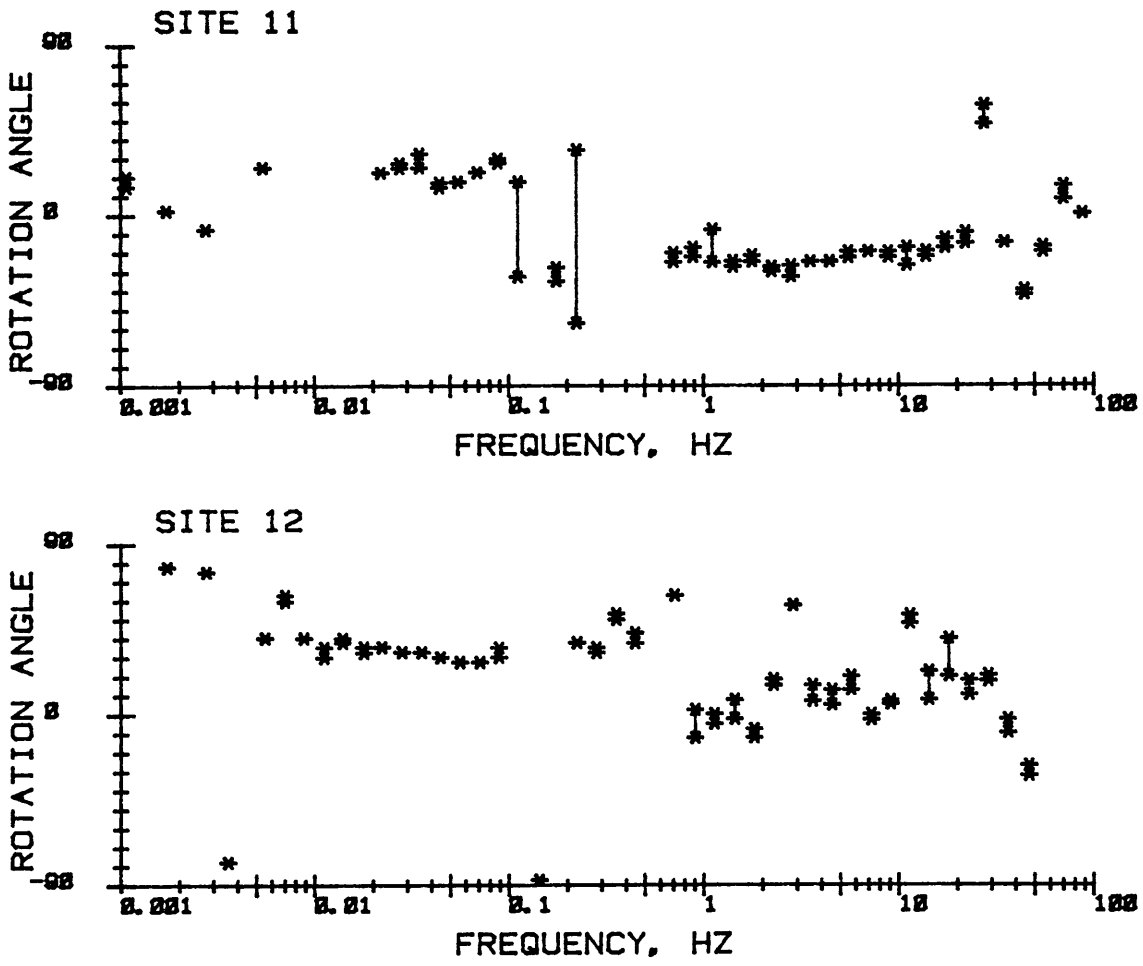


Figure 4.3.16--Plot of All Sounding Curves Corrected for Surface Heterogeneity

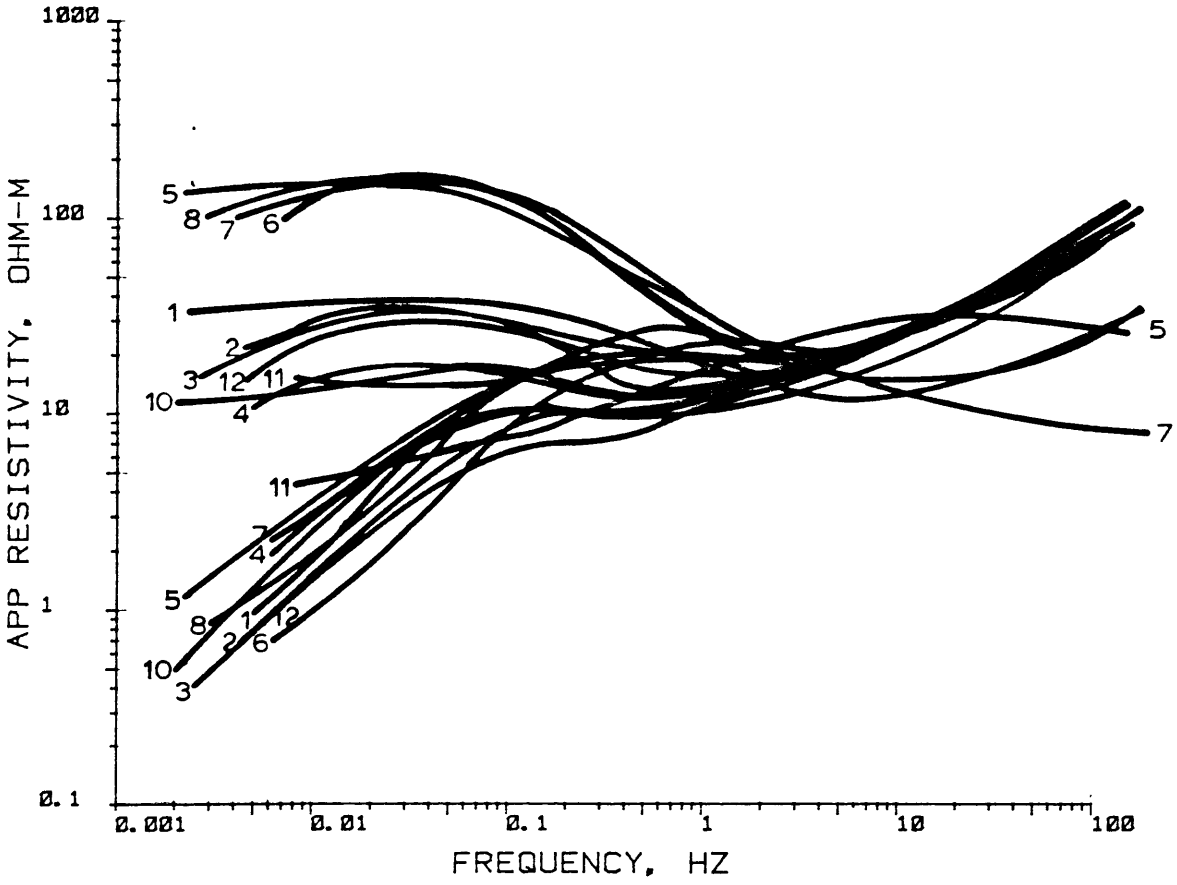


Figure 4.3.17--Generalized MT Sites 1 and 2 with Curves of Good Fit

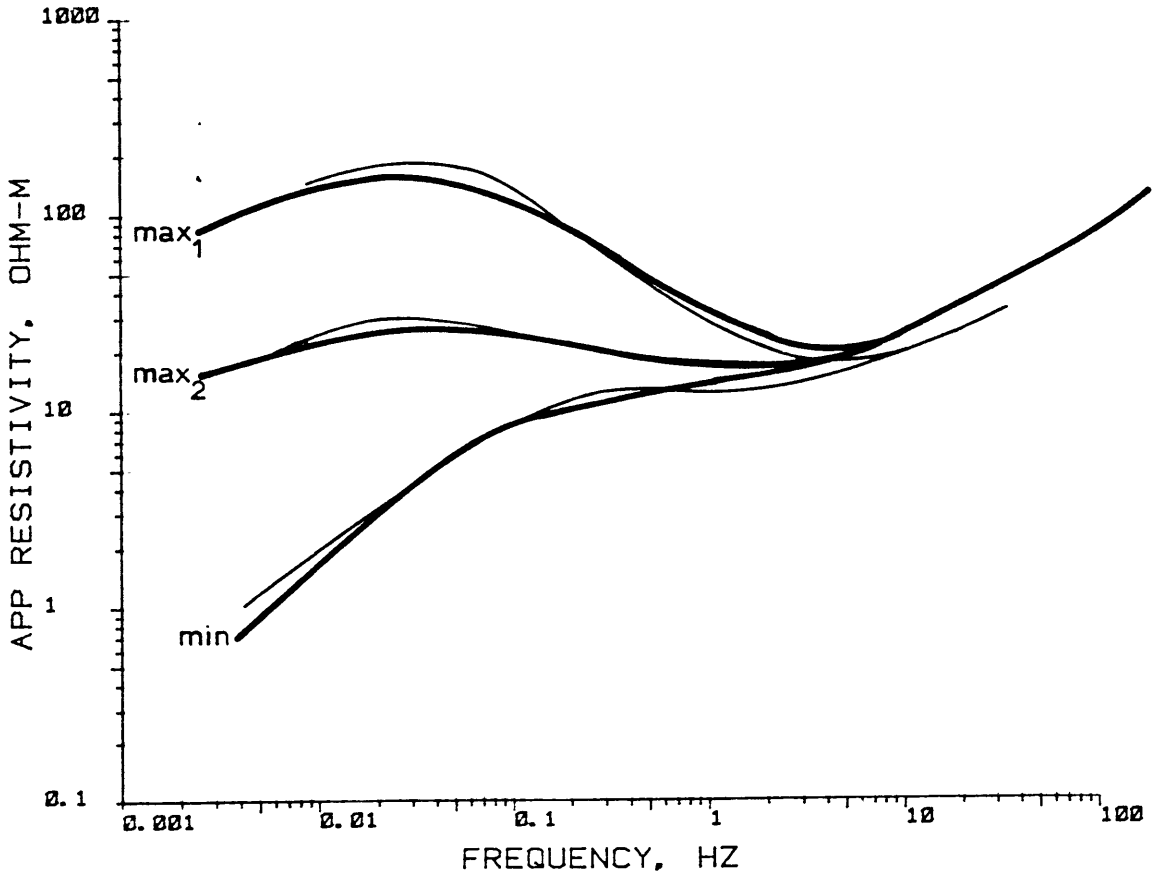


Figure 4.3.18--Model Used to Generate Curves of Good Fit

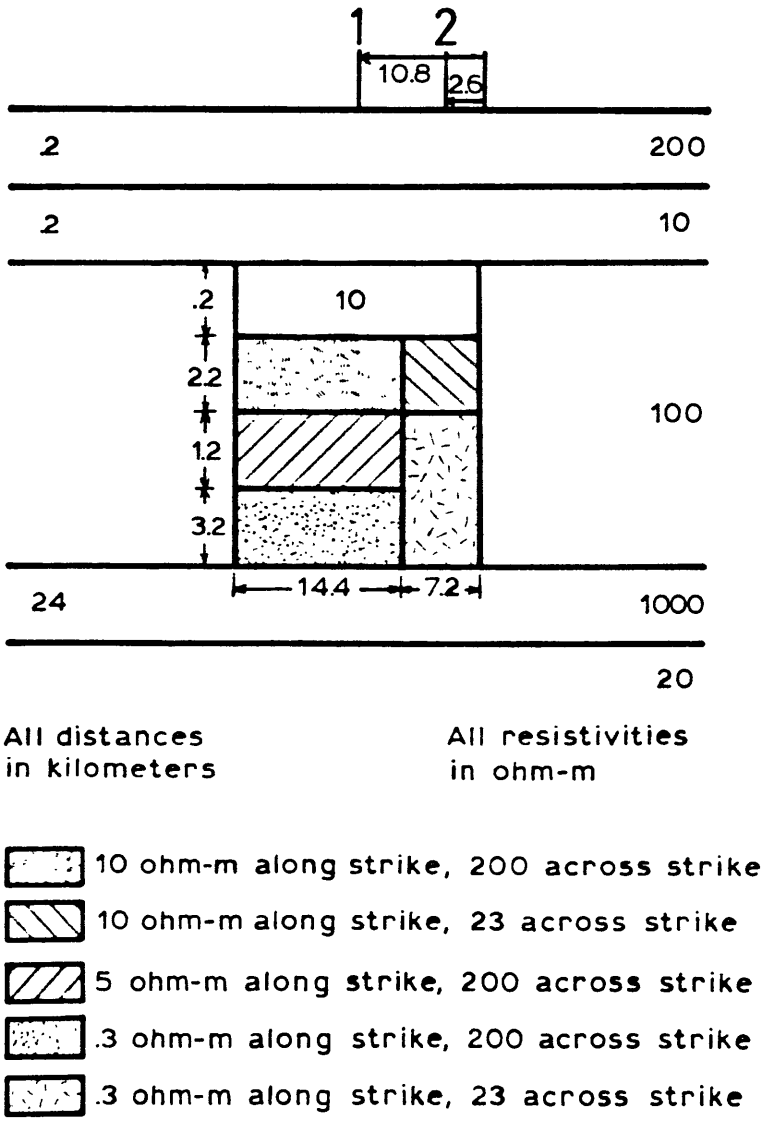
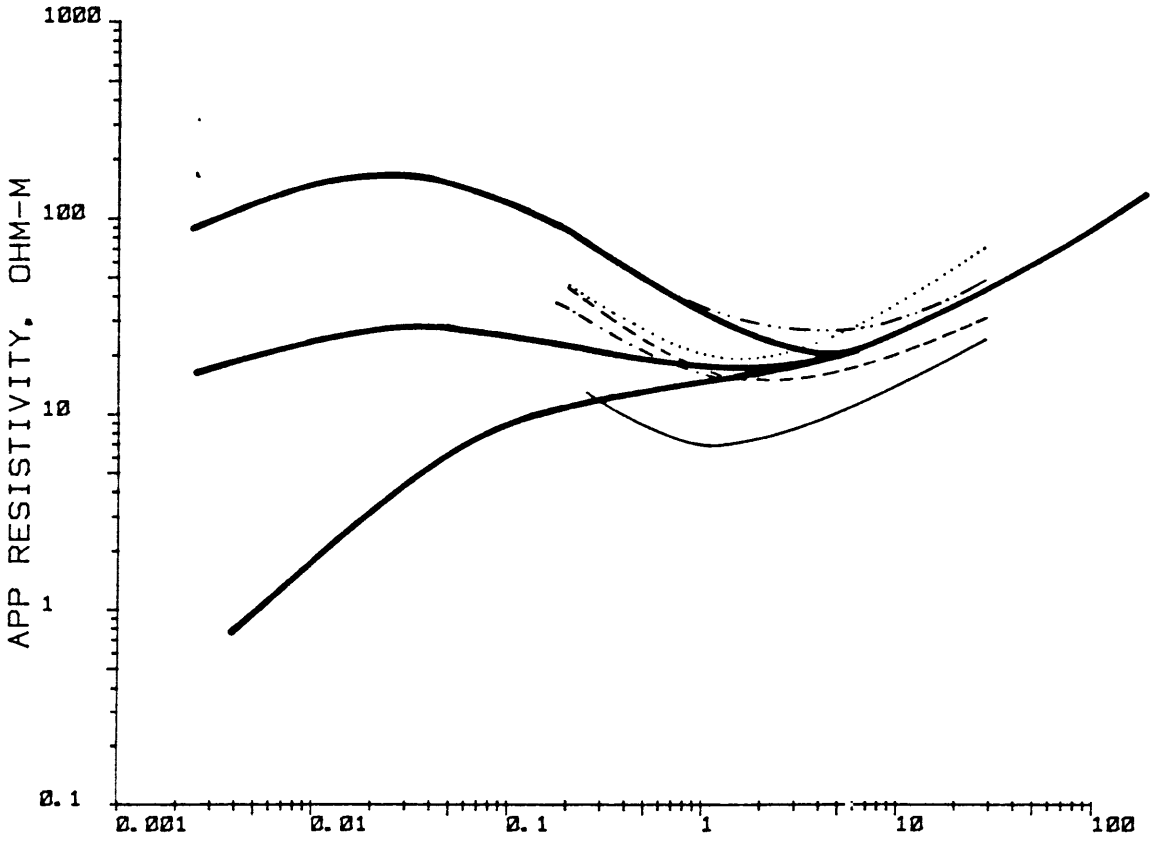


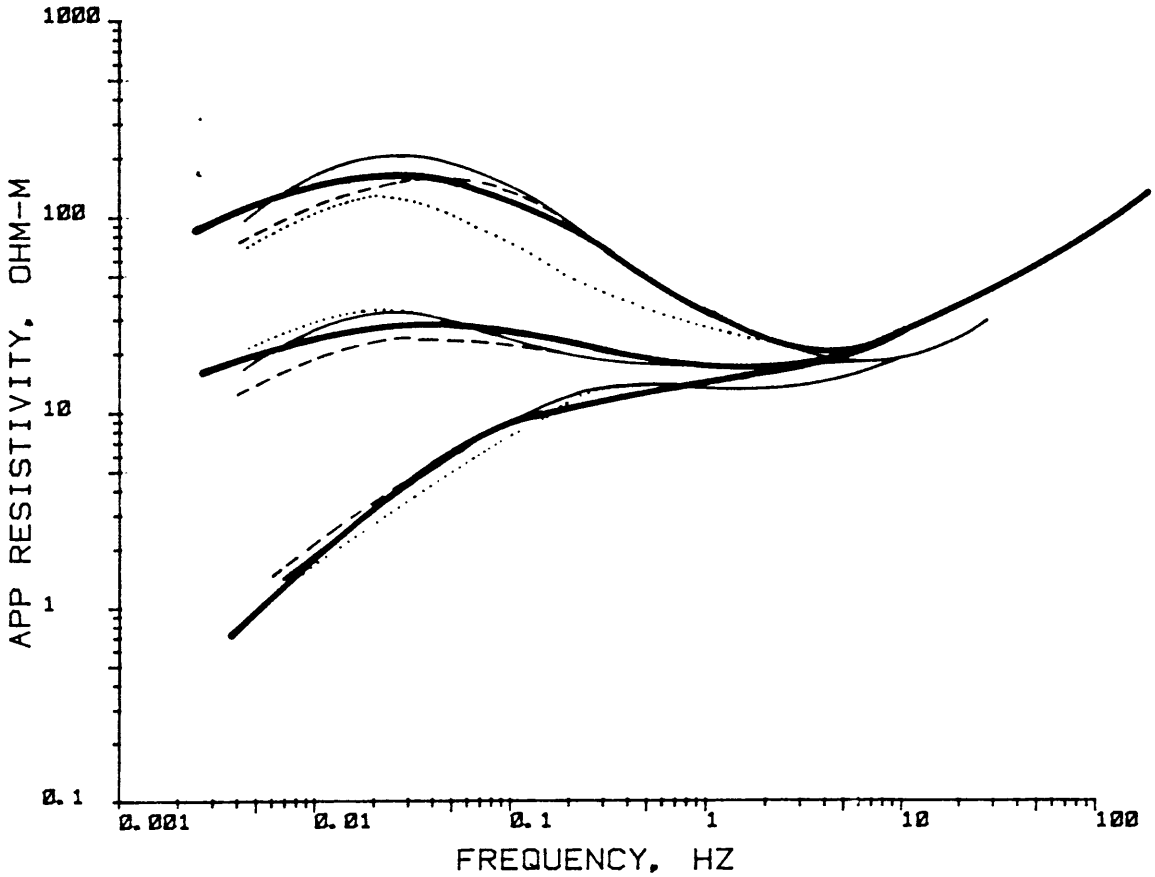
Figure 4.3.19--Sensitivity Analysis--Surface Structure



KEY

—— 2nd layer resistivity decreased from 10Ω•m to 5Ω•m
- - - Top layer resistivity increased from 200Ω•m to 400Ω•m
····· Top layer thickness increased from 200m to 400m
—·— 2nd layer thickness increased from 200m to 400m
—··— 2nd layer resistivity increased from 10Ω•m to 20Ω•m

Figure 4.3.20--Sensitivity Analysis--Lower Crust



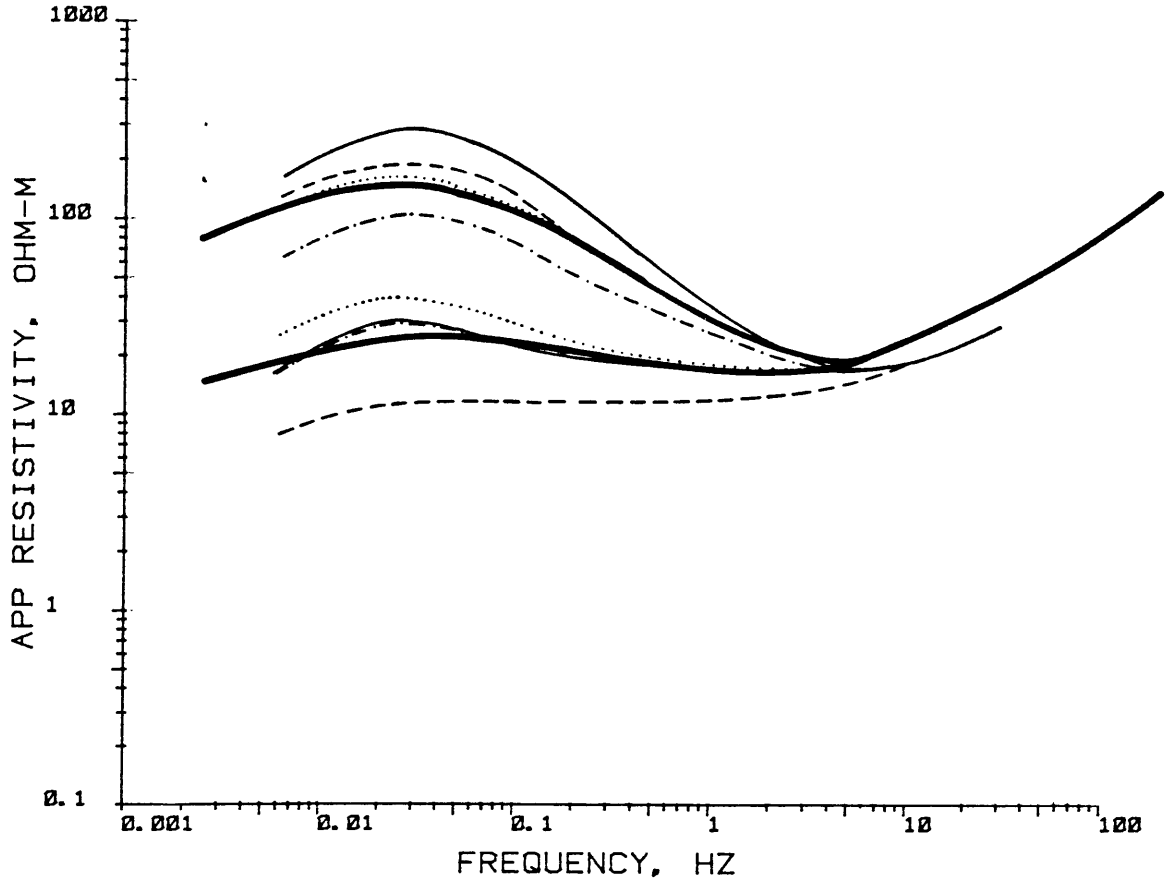
KEY

—— Lower crustal resistivity increased from 1000Ω•m to 10000Ω•m

- - - Lower crustal thickness decreased from 24km to 16km

····· Lower crustal thickness increased from 24km to 32km

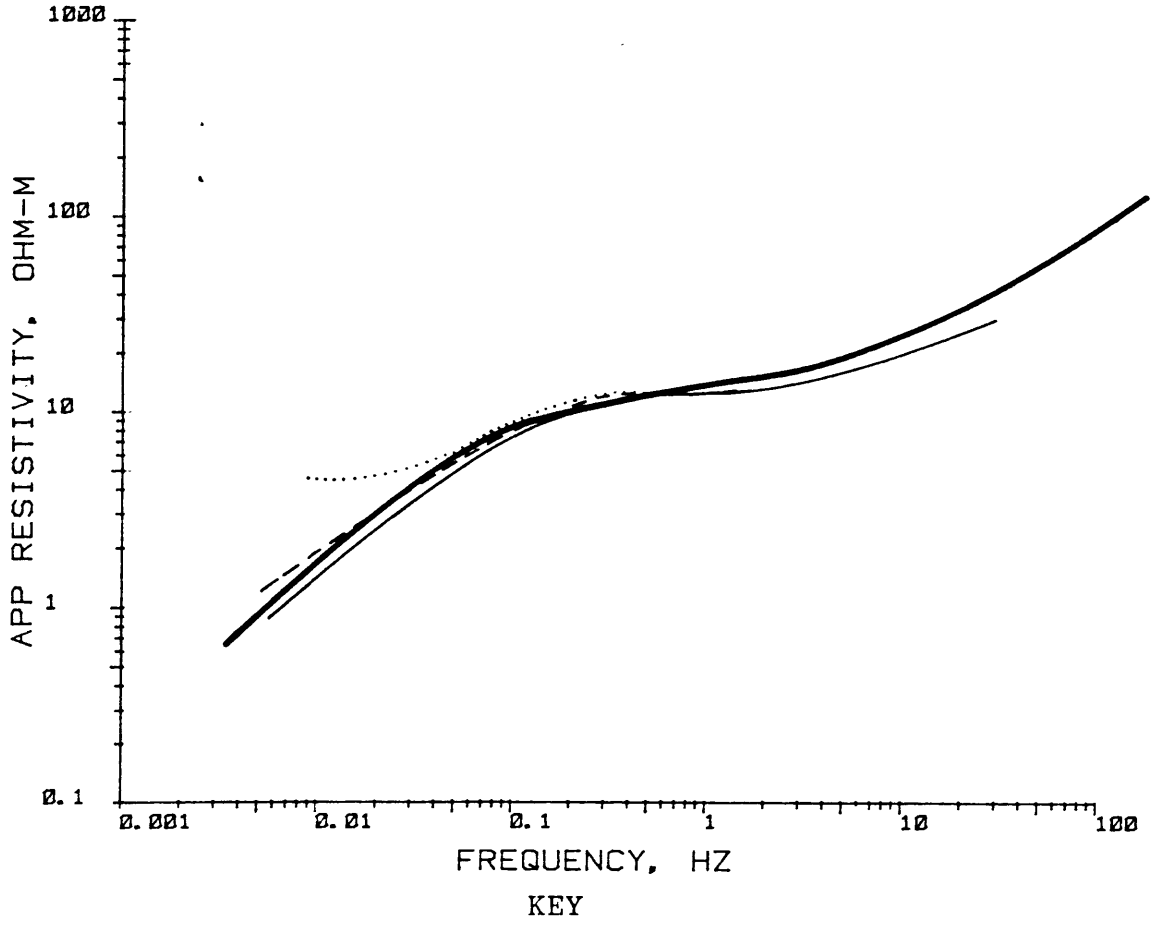
Figure 4.3.21--Sensitivity Analysis--Resistivity Across Strike



KEY

——— Resistivity increased from 200Ω•m to 400Ω•m
– – – Resistivity decreased from 23Ω•m to 11Ω•m
····· Resistivity increased from 23Ω•m to 30Ω•m
—·— Resistivity decreased from 200Ω•m to 100Ω•m

Figure 4.3.22--Sensitivity Analysis--Resistivity Along Strike



4.4 Effect of Truncation of a 2-D Body

The previous section produced a 2-D model which exhibited all the essential characteristics of the observed data. We answer here the question of whether this 2-D body can be truncated along strike without significantly affecting the fields. We simplify the model of Figure 4.3.18 to prevent confusion from factors such as anisotropy. The simplified model is presented in Figure 4.4.1. We examine the truncation effect at one frequency (.01 Hertz) only. The essential behavior can be seen without multi-frequency plots.

LaTorraca (1981) examined the change in the DC field within a conductive ellipsoid buried in a homogeneous half-space. The ellipsoid is prolate (cigar-shaped), so it is a rough approximation to our rectangular conductive body. The conductivity contrast in our model (Figure 4.4.1) is 100:1. LaTorraca (1981) predicts the apparent resistivity along strike should be 0.7% of its 2-D value for an aspect ratio of 3:1, and 11% for an aspect ratio of 10:1. These changes assume the field behaves only in a resistive (i.e., DC) manner. The conductive feature draws current towards itself, but is unable to attract enough because of its finite dimensions along strike.

Table 4.4.1 summarizes the results of 3-D modelling

applied to the model in Figure 4.4.1 for various aspect ratios. Included in this table is an evaluation of the effect of the repetition assumption. The apparent resistivities shown here are for a site above the symmetry point of the conductive body. The effect of the repetition assumption was tested by using rectangular blocks with aspect ratios of 3:1. This change moved the image features 3 times further away along strike, making it 240 kilometers away from the conductive body. The apparent resistivity along strike changed by about 15% for the aspect ratio of 3:1. The effect of the image conductors are thus present in the solutions, but it cannot explain the large deviations observed from the expected DC behavior.

The most striking feature of Table 4.4.1 is that the apparent resistivity along strike did not decrease by an order of magnitude when we changed the aspect ratio from ∞ to 7:1. The apparent resistivity actually increased by 20%, but we believe this increase is due to interactions between the conductive feature and its images. The resistivity along strike decreases as we decrease the aspect ratio, but the maximum change is only 20% for any aspect ratio above 3:1. The mechanism controlling the current in the conductor is clearly not DC current flow.

We know from Section 2.3 that local induction plays an important role in this model (The model in Figure 4.4.1 is essentially the model in Figure 2.3.11). The induction

contribution is primarily dependent upon the body thickness (See Appendix B), so varying the horizontal aspect ratio should have little effect. We observe this in Table 4.4.1. Hence, local induction is responsible for the lack of change in apparent resistivities.

We conclude that the aspect ratio need not be very large for the apparent resistivities along strike to be within a few percent of the values for the 2-D model. The conductive body is such a good conductor that local induction dominates the electric field. Hence, varying the aspect ratio does not affect the current level much. The conductive 2-D body in Figure 4.3.18 is 18 kilometers wide, so any length along strike greater than 60 kilometers is allowable (based on a 3:1 aspect ratio). The length inferred from the aeromagnetic survey is 120 kilometers, so we have good agreement between the length estimates.

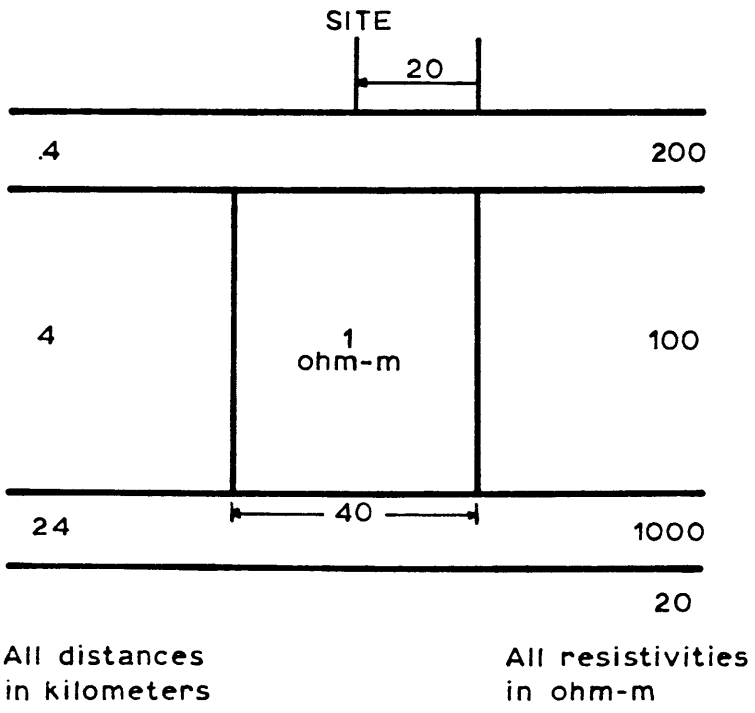
Table 4.4.1

Aspect Ratio	Model Size	ρ_a Across Strike	ρ_a Along Strike
∞	40 km × ∞	.58	1.56
7:1	40 km × 280 km	.58	1.93
3:1	40 km × 120 km	.56	1.74
3:1*	40 km × 120 km	.60	1.52
1:1	40 km × 40 km	.99	.99

All apparent resistivities in ohm-m.

* Denotes test of repetition assumption using rectangular blocks with aspect ratio of 3:1.

Figure 4.4.1--Simplified Model Used to Study Truncation Effects



4.5 Summary

The structure beneath the Beowawe, Nevada KGRA is an anisotropic feature 20 mkm wide and 7 km thick. The body has a NW strike and minimum length along strike of 60 km. The conductivity anisotropy is due to a series of NNW trending diabase dikes which make the structure conductive along strike (1 Ω•m) and resistive across strike (200 Ω•m). The body is buried beneath a thin (400 m) veneer of sediments and andesite flows. The lower crust beneath the region is fairly resistive (1000 Ω•m) but not too thick (24 km). This interpretation is consistent with gravity, resistivity, and aeromagnetic data for this region. Many of the lateral structural constraints are based on these other data, and the MT soundings are used to establish limits for the conductivities and thicknesses.

'When in doubt, try something. It doesn't matter what. Anything at all, but try something.'

Ken Bond

CHAPTER 5

5.1 Introduction

Structures several hundred kilometers from a measurement site can influence the electric and magnetic fields at that site. A good example of this is the field distortion due to the ocean-continent boundary. This distortion has been documented in data (e.g., Kasameyer, 1974) and has been theoretically modelled (Ranganayaki and Madden, 1980). We desire local structural information from an MT survey used for exploration. The typical scale size for these local structures is one kilometer. A practical, efficient modelling algorithm must include both the local scale and the regional scale. The technique presented in Chapter 2 uses just one scale, and is thus inadequate.

One method to incorporate many scales into the modelling algorithm is the 'multiple scales' technique proposed by Ranganayaki (1978). The fields are determined on a regional scale, and these results are used as boundary terms for the local scale. This method will theoretically work for many scales, but was applied to just two scales by Ranganayaki (1978). We will continue to use just two scales in our work.

We review Ranganayaki's multiple scales approach and illustrate its shortcomings in this chapter. We also present our unsuccessful attempt to improve her multiple scales method. Finally, we suggest a possible way to successfully perform the multiple scale analysis. The results presented in this chapter are all negative, but provide considerable insight into the problem.

5.2 Ranganayaki's Approach

We review the multiple scales method in this section and discuss its problems. We also present our attempt to improve the method. Figure 5.2.1 illustrates the model we use here. The heavy dotted lines are the coarse grid, or regional scale. The thin solid lines are the fine grid, or local scale. The unshaded region is the exterior region, while the shaded region is the interior region (or region of interest). We wish to determine the local scale fields in the interior region without solving for the local fields everywhere. We use the regional solution to estimate the local fields in the exterior region, and assume that the errors incurred using this approximation are small. We show here that this assumption is not valid.

Ranganayaki (1978) begins with Maxwell's equations in the form presented by equations (2.2.13) and (2.2.14). These equations give the total field change across a thin layer. The thin layer can be thought of as a laminate of a conductive, heterogeneous layer and a resistive, homogeneous layer. The electric field changes across the resistive layer, but not the conductive layer. The magnetic field, however, changes across the conductive layer, but not the resistive layer. The resistive, homogeneous layer may be incorporated into the layered half-space, while the conductive, heterogeneous layer must be treated as a thin sheet. There are thus no electric field changes across

the heterogeneous layer.

The equation governing the field changes across the heterogeneous layer is

$$H_s^+ = H_s^- + \Delta Z\left(\hat{i}_z \times (\sigma_s E_s^-) - \nabla_s((\nabla_s \times E_s^-)\cdot\hat{i}_z)/(j\omega\mu)\right) \quad (5.2.1)$$

Ranganayaki (1978) uses the following boundary conditions at the top and bottom of the thin layer

$$H_s^- = Y_{earth} * E_s^- \quad (5.2.2)$$

$$H_s^+ = H_{s0} + Y_{air} * E_s^- \quad (5.2.3)$$

where Y_{earth} is the admittance of the layered half-space, Y_{air} is the admittance of the air, and H_{s0} is the source magnetic field. We substitute (5.2.2) and (5.2.3) into (5.2.1) to derive an equation for E_s^-

$$H_{s0} = \left[Y_{earth}* - Y_{air}* + \Delta Z\left(\hat{i}_z \times (\sigma_s \cdot) - \nabla_s((\nabla_s \times \cdot)\cdot\hat{i}_z)/(j\omega\mu)\right)\right]E_s^- \quad (5.2.4)$$

The operator in (5.2.4) is a full convolution operator in the space domain. We rewrite this equation to simplify the notation

$$H_{s0} = Y' * E_s^- \quad (5.2.5)$$

where Y' is the operator shown in (5.2.4).

We set up and solve (5.2.5) at the regional scale in the first step of the multiple scales process. This procedure yields one electric field value per large block in Figure 5.2.1. The fields in the exterior region are approximated by the regional solution. The single regional field is assigned to each of the 9 small blocks which make up the large block. The local scale fields in the exterior region are thus generated in this manner. Equation (5.2.5) is reformulated using the fine grid, and E_s^- is broken up into the known values in the exterior region and the unknown values in the interior region

$$H_s^- = Y' * E_s^-{}_{exterior} + Y' * E_s^-{}_{interior} \qquad (5.2.6)$$

We then transfer the known portion of the convolution to the source side of (5.2.6) to get the final equation for the interior region fields

$$H_s^- - Y' * E_s^-{}_{exterior} = Y' * E_s^-{}_{interior} \qquad (5.2.7)$$

Ranganayaki (1978) applied this multiple scales method to the problem of resistive islands in a conductive ocean and achieved good results. This success was possible because the fields in the exterior region were much smaller than in the interior region. Errors in the approximation

were much smaller than the interior fields. Hence, the errors in the effective source term , $Y' * \bar{E}_s$ exterior, were negligible.

The problems with the approximation scheme surface when the multiple scales method is applied to conductive bodies (geothermal reservoirs or mineral bodies) in a resistive medium. The fields in the exterior region are at least an order of magnitude larger than those in the interior region. Errors in approximation in the exterior region thus become significant. The convolution process creates some constructive interference of the errors, and source term inaccuracies are frequently larger than the individual field errors in the exterior region. Individual exterior region field errors may be as much as 100%, and source term errors are higher. The key is that these errors in estimation are 10 times the magnitude of the interior region fields, and produce severe mistakes in the interior solution.

Figure 5.2.2 illustrates a model used for comparison of the correct solution and the multiple scales solution. The interior region for this comparison is the central large block containing the conductive feature. Figure 5.2.3 presents the fields for this comparison. The correct solution was computed using the fine grid and solving for the fields in both the interior and exterior regions. The fields are presented in units of apparent resistivity. Comparison shows that the fields inside the conductive

feature are consistently overestimated, and the fields outside are underestimated.

The multiple scales approach proposed by Ranganayaki is a sound one in theory. The difficulty with the method lies in the approximation scheme for the exterior region. None of the field distribution information in the exterior region is preserved. We accordingly attempt to improve this estimation process. The frequencies in our problem are low enough that the DC solution is a good approximation to the fields in the exterior region. We first solve the DC (resistivity) problem at the local scale and then use these results to predict the current (and hence field) distribution in the exterior region.

We use a network approximation to the DC problem (Madden, 1972) and solve the equations

$$\nabla \cdot J = 0 \qquad (5.2.8)$$

$$\nabla \times E = 0 \qquad (5.2.9)$$

We get the x and y current densities at the local scale from the DC solution and average the fine grid solution within each coarse grid block. In this manner, we generate the ratio of the local scale current to the average regional scale current in the exterior region. We also compute the average conductivity for each large block from the average electric field and average current density for the DC solution. We next compute the regional scale solution for

the electromagnetic (EM) problem, just as Ranganayaki does. The local current density in the exterior region is predicted from the regional current density

$$J_{exterior,local,EM} = J_{exterior,regional,EM} \cdot \left[\frac{J_{local}}{J_{regional}}\right]_{DC} \tag{5.2.10}$$

The electric fields for the exterior region are

$$E_{exterior,local,EM} = \frac{\sigma_{regional,DC}}{\sigma_{local}} \cdot \left[\frac{J_{local}}{J_{regional}}\right]_{DC} \cdot E_{regional,EM} \tag{5.2.11}$$

This estimation procedure yields exterior region fields which are much closer to the correct solution, but errors may still be 10-20%. These errors are still sufficient to produce large errors in the interior region fields. Figure 5.2.4 shows a model used for comparison of the modified multiple scales solution to the correct solution. Figure 5.2.5 presents the fields for this comparison. The multiple scales solution is still erroneous, but it is much closer to the correct solution than the results in Figure 5.2.3. Two-dimensional symmetry is expected in the fields because the model is two-dimensional. This symmetry is missing in the multiple scales solution in Figure 5.2.5 because of the field estimation process. The lack of symmetry indicates

that the multiple scales solution is erroneous. The improved approximation scheme helps, but not enough.

The basic problem with this multiple scales method is that it is too sensitive to errors in fields in the exterior region. This sensitivity is a result of the convolution operation--it amplifys errors. We now suggest an alternate scheme which may bypass this problem.

Figure 5.2.1--Multiple Scales Grid

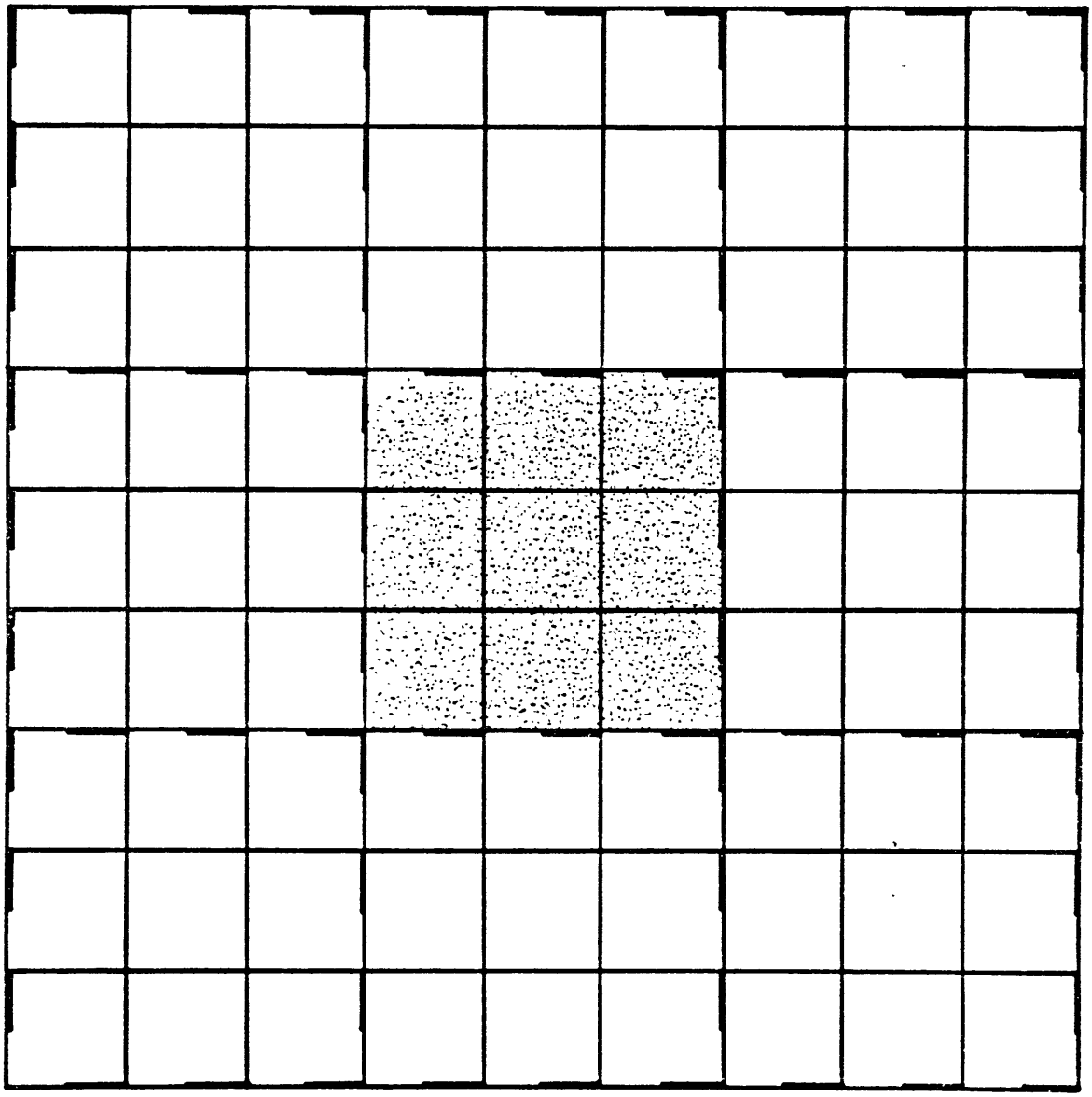
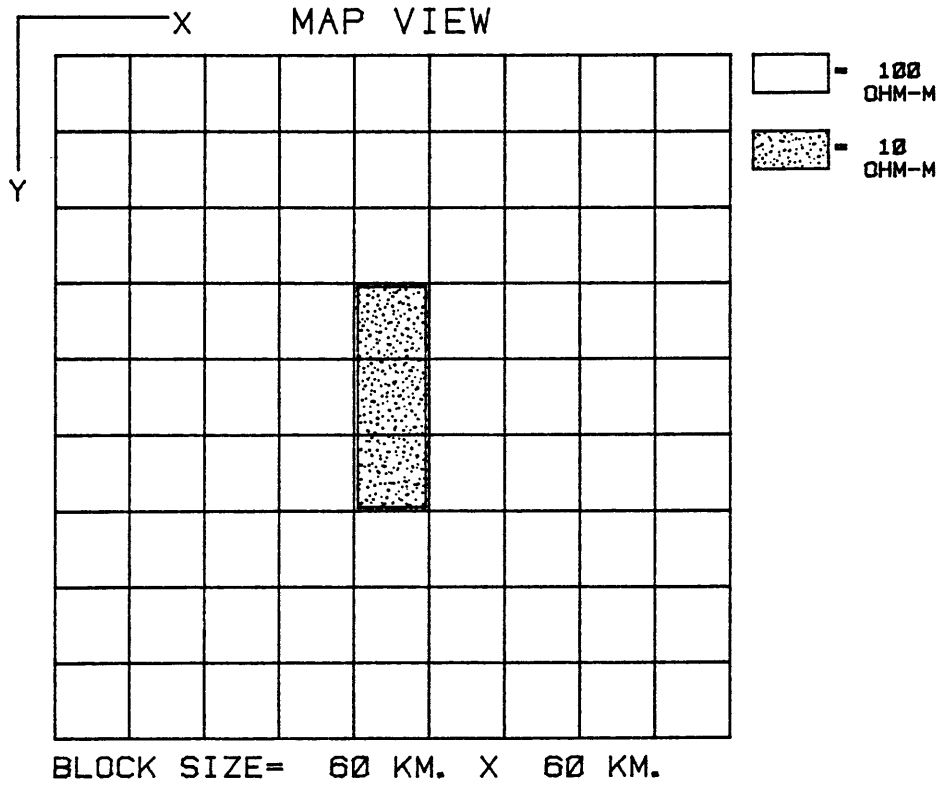


Figure 5.2.2--Model Used to Compare Ranganayaki's Solution to Correct Solution



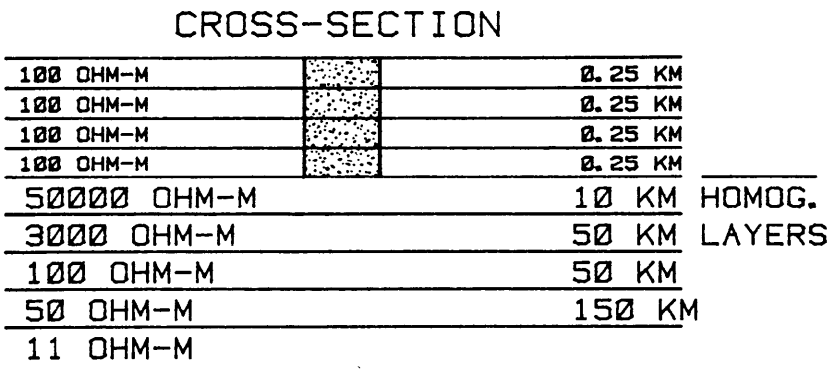


Figure 5.2.3--Comparison of Multiple Scales Solution to Correct Solution

MULTIPLE SCALES SOLUTION

Ex

382	162	382
502	80	502
382	162	382

Ey

199	246	199
253	119	253
199	246	199

CORRECT SOLUTION

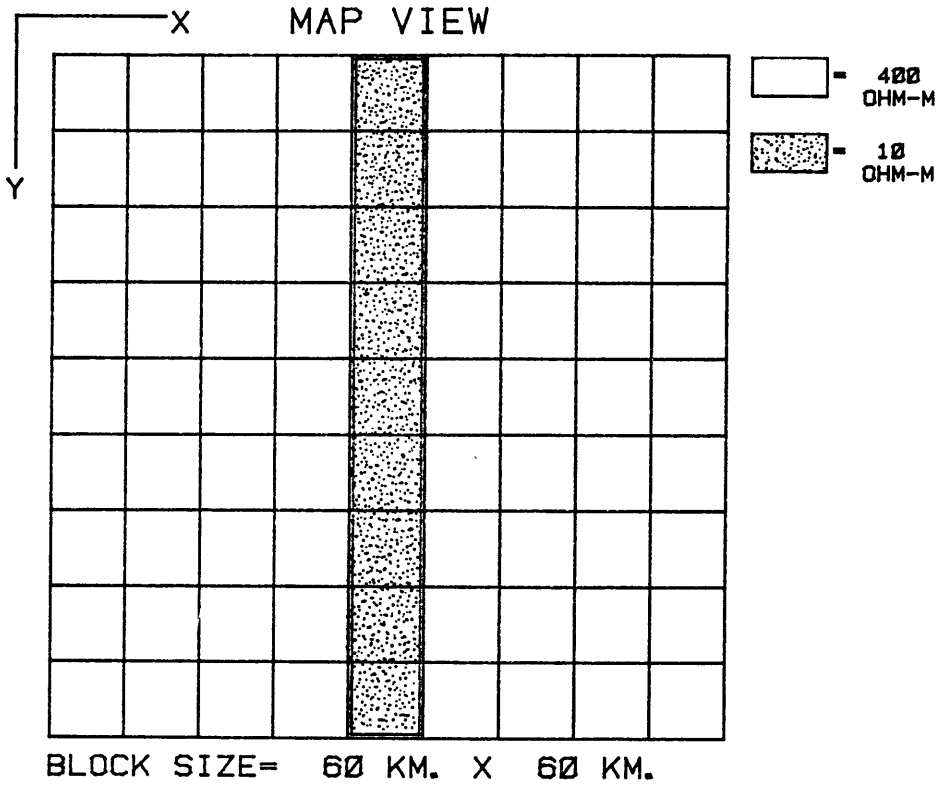
Ex

557	11	557
545	6.5	545
557	11	557

Ey

218	44	218
172	62	172
218	44	218

Figure 5.2.4--Model Used to Compare Improved Multiple Scales Solution to Correct Solution



CROSS-SECTION

400 OHM-M	2 KM	
400 OHM-M	4 KM	HOMOG.
10000 OHM-M	20 KM	LAYERS
3030 OHM-M	50 KM	
100 OHM-M	50 KM	
50 OHM-M	50 KM	
10 OHM-M		

Figure 5.2.5--Comparison of Improved Multiple Scales Solution to Correct Solution

MULTIPLE SCALES SOLUTION

Ex

98	.08	98
98	.05	98
98	.08	98

Ey

31	28	31
63	121	63
31	28	31

CORRECT SOLUTION

Ex

87	.26	87
87	.26	87
87	.26	87

Ey

44	44	44
44	44	44
44	44	44

5.3 Equivalent Sources and Multiple Scales

We propose an alternate approach to the multiple scales problem in this section. This approach differs from the previous one in that we replace the exterior region with fields sources on the boundary of the interior region.

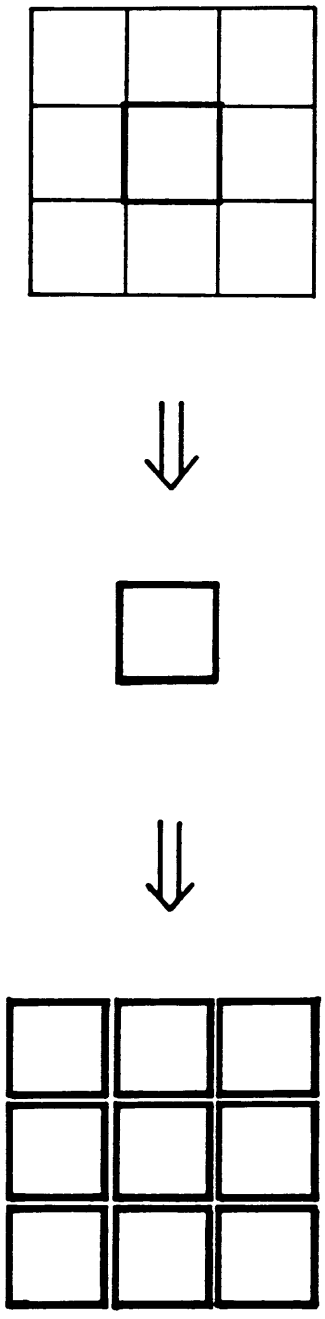
We use the average conductivity from the DC solution and compute the regional solution as in the previous section. We then get fields at the boundary between the interior and exterior regions. Figure 5.3.1 is a graphic representation of our proposed procedure. The heavy, solid lines in the top sketch represent the boundary fields. The second sketch in Figure 5.3.1 shows these fields on the boundaries of the interior region.

The final step is to embed the interior region with its sources in an infinite, repetitive medium of like cells. This embedding is shown in the third sketch of Figure 5.3.1. We can then use a modified form of the thin sheet solution method presented in Chapter 2 to solve for fields at the surface. The problem is complicated because the boundary fields must be substituted for the exterior region at all levels in the structure including the homogeneous, layered half-space and the air above the surface.

This proposed method eliminates the need for the convolution of the local scale Y' with the local scale fields in the exterior region. Ranganayaki's multiple scale approach (1978) essentially dealt with only one scale

because the boundary for model repetition did not change. The total number of wavenumbers for the whole region (interior and exterior) increased as finer subdivisions of the grid were used. Our procedure retains the same number of wavenumbers at each step, although the actual wavenumbers are different. The local scale information in the exterior region is not needed in the proposed procedure. All necessary information is contained within the boundary fields we use.

Figure 5.3.1--Proposed Multiple Scales Method



'What a long, strange trip it's been.'

Grateful Dead

CHAPTER 6

We have developed an efficient 3-D modelling alogorithm in this thesis. This modelling procedure has been used to extend our knowledge about interactions of MT fields with complicated structures. We have used simple techniques to identify which physical mechanism is controlling field behavior. These mechanisms are horizontal current gathering, vertical current gathering, and local induction. The emphasis has been on understanding why the fields behave the way they do, rather than generating a catalog of models. We believe the estimation techniques can be applied to real data to identify the dominant mechanism. This identification will, in turn, lead to an accurate qualitative interpretation of the data--the first step towards good quantitative interpretation.

We have also outlined the theoretical groundwork for a practical 3-D inversion based on the forward modelling scheme of Chapter 2. We showed this complicated theory reduced to known results when applied to a simple problem. We believe this procedure will be the most efficient inversion method for complicated structures. Practical application of this theory has begun.

We applied the techniques and insights in Chapter 2 to

interpretation of MT data from Beowawe, Nevada. The most important result from this interpretation is that, when local induction dominates the electric field, horizontal dimensions along the strike of a 2-D body are relatively unimportant. We also showed that the 12 sites comprising this survey were really only 2 unique sites. The rest were just duplicates affected by surface heterogeneities. We see from this survey that adequate areal coverage of the region, both on and off the target, is essential for accurate interpretation. These data would have been uninterpretable without independent geologic and geophysical information.

We finally discussed our unsuccessful attempts at solving the most critical, difficult, and interesting problem in MT modelling--that of multiple scaling. We must be able to effectively model both the local, fine structure and the regional, gross structure simultaneously. We understand the problem more thoroughly now, but a correct approach to its solution eludes us. We suggest a possible method, but much work is still needed.

REFERENCES

Boehl, J.E., F.X. Bostick, Jr., and H.W. Smith, 1977. An Application of the Hilbert Transform to the Magnetotelluric Method, Electrical Geophysics Research Laboratory Report, Univ. of Texas at Austin, 98 pp.

Cagniard, L., 1953. "Basic Theory of the Magnetotelluric Method of Prospecting", Geophys. 18, p. 605-635.

Chevron Resources Company, 1975. Well Summary Report for Ginn #1-13 Well.

Dawson, T.W., and J.T. Weaver, 1979. "Three-dimensional Induction in a Non-uniform Thin Sheet at the Surface of a Uniformly Conducting Earth", Geophys. Jour. R.A.S. 59, p. 445-462.

Erwin, J.W., 1974. Bouguer Gravity Map of Nevada, Winnemucca Sheet, Nev. Bur. of Mines and Geol. Map 47.

Hermance, J.F., 1982. "The Asymptotic Response of Three-dimensional Offsets to Magnetotelluric Fields at Long Periods: The Effects of Current Channeling", Geophys. 47, p. 1562-1573.

Hohmann, G.W., and S.C. Ting, 1978. Three-dimensional Magnetotelluric Modelling, Dept. of Energy Rept. ID0-1601-4, Univ. of Utah Research Institute, 48 pp.

Jacobs, J.A., 1970. Geomagnetic Micropulsations, Springer-Verlag, New York, 179 pp.

Jiracek, G.R., M.E.Anders, and H.T. Holcombe, 1979. "Magnetotelluric Soundings of Crustal Conductive Zones in Major Continental Rifts" in Rio Grande Rift: Tectonics and Magmatism, AGU, p. 209-222.

Kasameyer, P.W., 1974. Low-frequency Magnetotelluric Survey of New England, PhD Thesis, Massachusetts Institute of Technology, 204 pp.

Kaufman, A.A., and G.V. Keller, 1981. The Magnetotelluric Sounding Method, Elsevier Scientific Publishing Co., Holland, 595 pp.

Kong, J.A.,1975. Theory of Electromagnetic Waves, Wiley, New York, 339 pp.

Laird, E.E., and F.X.Bostick, Jr., 1970. One-dimensional Magnetotelluric Modelling Techniques, Electrical Engineering Research Laboratory, Tech. Rept. 101, Univ. of Texas at Austin.

Lanczos C., 1956. Linear Differential Operators, Van Nostrand, New York, 564 pp.

LaTorraca, G.A., 1981. Differential Tellurics, PhD Thesis, Massachusetts Institute of Technology, 182 pp.

Lines, L.R., and F.W. Jones, 1973. "The Perturbation of Alternating Geomagnetic Fields by Three-dimensional Island Structures", Geophys. Jour. R.A.S. 32, p. 133-154.

Madden, T.R. ,1972. Transmission Systems and Network Analogies to Geophysical Forward and Inverse Problems, ONR Rept. N000-14-67-A-0204-0045, 45 pp.

_____, 1980. "Lower Crustal Effects on Magnetotelluric Interpretations or Pulling the Mantle Up by Its Bootstraps" presented at Workshop on Research in Magnetotellurics: Implications of Electrical Interpretation for Geothermal Exploration.

_____, and S.K. Park, 1982. Magnetotellurics in a Crustal Environment, USGS Final Rept.

Morrison, H.F., K.H. Lee, G. Oppliger, and A. Dey, 1979. Magnetotelluric Studies in Grass Valley, Nevada, Lawrence Berkeley Laboratory Report LBL-8646, 50 pp.

Oppenheim, A.V., and R.W. Schafer, 1975. Digital Signal Processing, Prentice Hall, New Jersey, P. 337-366.

Orzag, S.A., 1972. "Comparison of Pseudospectral and Spectral Approximation", Stud. Appl. Math. 51, p. 253-259.

Park, S.K., A.S. Orange, and T.R. Madden, 1983. "Effects of Three-dimensional Structure in Magnetotelluric Sounding Curves", Geophys. in press.

Ranganayaki, R.P., 1978. Generalized Thin Sheet Approximation for Magnetotelluric Modelling, PhD Thesis, Massachusetts Institute of Technology, 204 pp.

_____, and T.R. Madden, 1980. "Generalized Thin Sheet Analysis in Magnetotellurics: An Extension of Price's Analysis", Geophys. J. R.A.S. 60, p. 445-457.

Reddy, I.K., D. Rankin, and R.J. Phillips, 1977. "Three-dimensional modelling in Magnetotelluric and Magnetic Variation Sounding", Geophys. J. R.A.S. 51, p. 313-325.

Roberts, R.J., K.M. Montgomery, and R.E. Lehner, 1967. Geology and Mineral Resources of Eureka County, Nevada, Nevada Bur. of Mines and Geol. Bull. 64 , 152 pp.

Robinson, E.A., 1966. "Multichannel Z-Transforms and Minimum Delay", Geophys. 31, p. 482-500.

Smith, C., 1979. Interpretation of Electrical Resistivity and Shallow Seismic Reflection Profiles, Whirlwind Valley and Horse Heaven Areas, Beowawe KGRA, Nevada, Univ. of Utah Research Institute Rept. ESL-25, 43 pp.

Stanley, W.D., J.E. Boehl, F.X., Bostick, Jr., and H.W. Smith, 1977. "Geothermal Significance of Magnetotelluric Sounding in the Eastern Snake River Plain--Yellowstone Region", J.G.R. 82, p. 2501-2514.

Stewart, J.H., G.W. Walker, and F.J. Kleinhampl, 1975. "Oregon-Nevada Lineament", Geology 3, p. 265-268.

Stewart, J.H., E.H. McKee, and H.K. Stager, 1977. Geology and Mineral Deposits of Lander County, Nevada, Nevada Bur. of Mines and Geol. Bull. 88, 106 pp.

Strangway, D.W., C.M. Swift, Jr., and R.C. Holmer, 1973. "The Application of Audio-frquency Magnetotellurics to Mineral Exploration", Geophys. 38, p. 1159-1175.

Swift, C.M., Jr., 1967. A Magnetotelluric Investigation of an Electrical Conductivity Anomaly in the Southwestern United States, PhD Thesis, Massachusetts Institute of Technology, 211 pp.

_____, 1979. "Geophysical Data, Beowawe Geothermal Area, Nevada", Geothermal Resources Council Trans. 3, p. 701-703.

Weidelt, P., 1975. "Electromagnetic Induction in Three-dimensional Structures", J. Geophys. 41, p. 85-109.

Vozoff, K., 1972. "The Magnetotelluric Method in the Exploration of Sedimentary Basins", Geophys. 37, p. 98-141.

APPENDIX A

Analytic error estimation for the numerical algorithm discussed in Section 2.2 is elusive because the errors are model-dependent. We do, however, present analytic and empirical errors for a limited class of models in this appendix. The analytic results are derived for an anisotropic half-space with wavenumber structure in the source field. This is essentially a 1-D problem. The numerical results are presented for a 3-D model similar to those used later in Section 2.3.

The anisotropic half-space has vertical resistivity, σ_v, and horizontal conductivity, σ_h. The source field is a magnetic field with an exp $(jk_x x+jk'_z z)$ spatial dependence. Maxwell's equations decouple into two modes: the Transverse Magnetic (TM) mode and the Transverse Electric (TE) mode. We examine the TM mode first. The equations governing the TM mode within the half-space are

$$\frac{\partial E_x}{\partial z} - \frac{\partial E_z}{\partial x} = j\omega\mu H_y \qquad \text{(A.1.1)}$$

$$\frac{\partial H_y}{\partial z} = -\sigma_h E_x \qquad \text{(A.1.2)}$$

$$\frac{\partial H_y}{\partial x} = \sigma_v E_z \qquad \text{(A.1.3)}$$

We substitute (A.1.2) and (A.1.3) into (A.1.1) and assume an x-z dependence of exp$(jk_x x+jk_z z)$ to derive the dispersion

relation. This relation is

$$k_z^2 = j\omega\mu\sigma_h - k_x^2(\sigma_h\rho_v) \qquad (A.1.4)$$

The TM mode has a magnetic field perpendicular to the direction of propagation given by (k_x,k_z), so $H=H_y$. The k_x in the half-space must be the same as that of the source field because of phase matching. The associated electric field is derived from (A.1.2) and (A.1.3). The half-space fields are

$$H=H_y\exp(jk_xx+jk_zz) \qquad (A.1.5)$$

$$E=jH_y\exp(jk_xx+jk_zz)[-\rho_hk_z\hat{i}_x+\rho_vk_x\hat{i}_z] \qquad (A.1.6)$$

We derive an error estimate for the field continuation operator (equations (2.2.13) or (2.2.14)). Suppose we continue the fields at $z=(z_0+\Delta z)$ up to $z=z_0$. The horizontal field at $z=z_0$ is then

$$E_{\text{approx}} = \rho_hk_zH_y\exp(jk_xx+jk_z(z_0+\Delta z))[-j-k_z\Delta z] \qquad (A.1.7)$$

The exact field at $z=z_0$ is

$$E_{\text{exact}} = -j\rho_hk_zH_y\exp(jk_xx+jk_zz_0) \qquad (A.1.8)$$

We divide (A.1.7) by (A.1.8) to get the ratio of the approximated field to the exact field

$$\frac{E_{\text{approx}}}{E_{\text{exact}}} = (1-jk_z\Delta z)\exp(jk_z\Delta z) \qquad (A.1.9)$$

Equation (A.1.4) gives the relation between k_x, k_z, and σ. We have two cases to examine: one in which k_x dominates k_z; and one in which $j\omega\mu\sigma$ dominates k_z. The first is important when source fields exhibit rapid horizontal fluctuations. The vertical wavenumber then is $jk_x(\sigma_h\rho_v)$. Notice that there is amplification of the error by the anisotropy factor, $\sigma_h\rho_v$, for the TM mode. We substitute this expression for k_z into (A.1.9) to get

$$\frac{\text{E approx}}{\text{E exact}} = (1+k_x(\sigma_h\rho_v)\Delta z)\exp(-k_x(\sigma_h\rho_v)\Delta z) \quad \text{(A.1.10)}$$

Table A.1.1 contains estimates of this ratio for different values of $k_x\Delta z$ and anisotropy factor.

This first case is heuristically similar to small scale conductivity heterogeneities in the presence of uniform source fields. The repetition assumption in Section 2.2 limits the number of horizontal wavenumbers, and the spatial Nyquist 'frequency' gives us the largest wavenumber. The maximum wavenumber is $k=\pi/\Delta L$, where ΔL is the horizontal block length. We see for no anisotropy (Table A.1.1) that $k\Delta z=.6$ is the maximum value for which fields are accurate to within 10%. This maximum value limits us to using Δz no greater than 20% of the horizontal block length.

The second case is the case of zero k_x. The dispersion relation then gives

$$k_z = (1+j)\sqrt{(\omega\mu\sigma_h/2)}=(1+j)/\delta \quad \text{(A.1.11)}$$

where δ is the electromagnetic skin depth. We substitute (A.1.11) into (A.1.9) to get the error criterion

$$\frac{\text{E approx}}{\text{E exact}} = (1+(1+j)\Delta z/\delta)\exp(-(1-j)\Delta z/\delta) \qquad \text{(A.1.12)}$$

We now have both amplitude and phase errors. These errors are tabulated in Table A.1.2 for several values of $\Delta z/\delta$. These limitations are much less restrictive than those of Table A.1.1. We can use thicknesses up to 70% of the skin depth in this case.

We now examine the TE mode. The equations governing field behavior in the anisotropic half-space are

$$\frac{\partial H_x}{\partial z} - \frac{\partial H_z}{\partial x} = \sigma_h E_y \qquad \text{(A.1.13)}$$

$$\frac{\partial E_y}{\partial z} = -j\omega\mu Hx \qquad \text{(A.1.14)}$$

$$\frac{\partial E_y}{\partial x} = j\omega\mu Hz \qquad \text{(A.1.15)}$$

The dispersion relation is derived as before by substituting (A.1.14) and (A.1.15) into (A.1.13) and assuming an $\exp(jk_x x + jk_z z)$ dependence in E_y. The dispersion relation is

$$k_z^2 = j\omega\mu\sigma_h - k_x^2 \qquad \text{(A.1.16)}$$

The anisotropy factor does not appear in the TE mode. The TE mode is so named because the electric field is polarized perpendicular to the direction of propagation. The electric

field is thus $E_y \exp(jk_x x+jk_z z)$. The associated magnetic field is determined by substituting E_y into (A.1.14) and (A.1.15). The TE mode fields are

$$E=E_y \exp(jk_x x+jk_z z) \tag{A.1.17}$$

$$H= E_y \exp(jk_x x+jk_z z)[-k_z \hat{i}_x+k_x \hat{i}_z]/\omega\mu \tag{A.1.18}$$

We again use (2.2.13) to predict the approximated field and divide by the exact field to get

$$\frac{E \text{ approx}}{E \text{ exact}} = (1-jk_z \Delta z)\exp(jk_z \Delta z) \tag{A.1.19}$$

The cases of large k_x and zero k_x are again considered. Comparison of (A.1.16) and (A.1.4) shows that the zero k_x cases for the TE and TM modes are identical. The large k_x case for the TE mode is identical to the same case for the TM mode with no anisotropy ($\sigma_h \rho_v=1$). Hence, Tables A.1.1 and A.1.2 contain the errors for the TE mode also.

The previous analytic error criteria are strictly only valid for an anisotropic half-space. This analysis can be extended to layered, anisotropic media, but not to laterally heterogeneous media. Lateral heterogeneity is always the case for 3-D bodies. We must resort to empirical error estimates for 3-D bodies. Figure A.1.1 illustrates a model used to evaluate these errors. The heterogeneous region is successively divided into more layers with smaller thicknesses so that the total thickness is always 600 m. We

present errors for the cases of large k and zero k for a frequency of 0.01 Hz. We have both k_x and k_y in this problem, so the effective k_z for large k is $k_x\sqrt{2}$. The largest horizontal wavenumber present in the solution is $kx=\pi/\Delta L$, so $k\Delta z$ for our model is $\sqrt{2}\pi\Delta z/\Delta L$. We first present errors for the large k case in Table A.1.3. Maximum errors in apparent resistivity inside and outside the heterogeneity are tabulated. The error shown is $|1-\rho_a/\rho_a$ at 9% thickness$|*$ 100%. We see from these errors that we are limited to using thicknesses less than 5% of the horizontal dimensions if we want errors less than 10%.

The second case we evaluate is that of zero k. The ratio of the thickness to the skin depth is now important, so the model in Figure A.1.1 has been changed. Block sizes are increased ten-fold, decreasing the maximum wavenumber by an order of magnitude. The frequency is increased to 1 Hz so that the minimum thickness used is now 10% of the skin depth. We perform the same error analysis as before by varying the individual layer thicknesses and the total number of layers. The results of this analysis are presented in Table A.1.4. We see that a thickness of half of the skin depth may be used before 10% errors appear.

We have presented both analytic and empirical error analyses in this appendix. These two types of analysis qualitatively agree. The aspect ratio ($\Delta z/\Delta L$) is much more restrictive than is the thickness:skin depth ratio. Field

errors of 10% or less occur for aspect ratios of less than 0.2. The thickness:skin depth ratio can be much larger--up to 0.5 is the same 10% error level is sought. These errors are model-dependent, however. The relative importance of solutions with the large wavenumber behavior is dependent upon the conductivity structure. Rapid spatial conductivity variations will produce a solution with large wavenumber structure.

Table A.1.1--Error Analysis for TM Mode

$\sigma_h\rho_v$ \ $k_x\Delta z$	.1	.2	.3	.4	.6	.8	1.0
0.3	1.00	.998	.996	.993	.985	.975	.963
1.0	.995	.982	.963	.880	--	--	--
3.0	.963	.880	--	--	--	--	--

Table A.1.2--Error Analysis for TE Mode

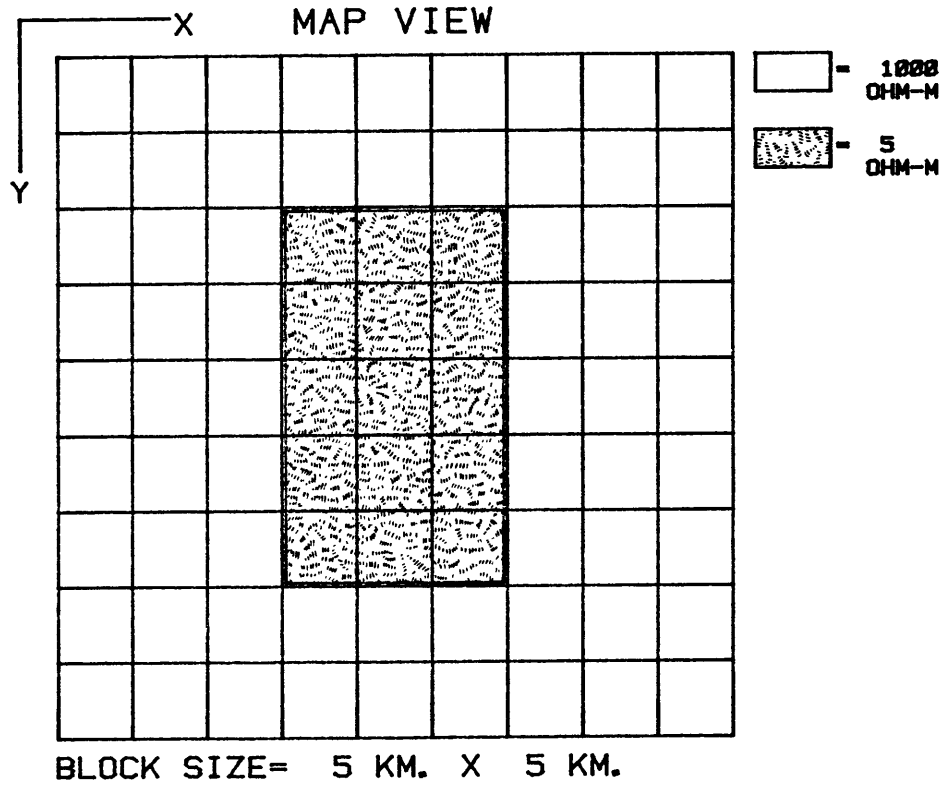
$\frac{\Delta z}{\delta}$	.1	.2	.3	.4	.6	.8	1.0
$\frac{E_{approx}}{E_{exact}}$	1.00	.996	.988	.976	.938	.890	.820
	0.6°	2.6°	5.9°	7.0°	14°	22°	31°

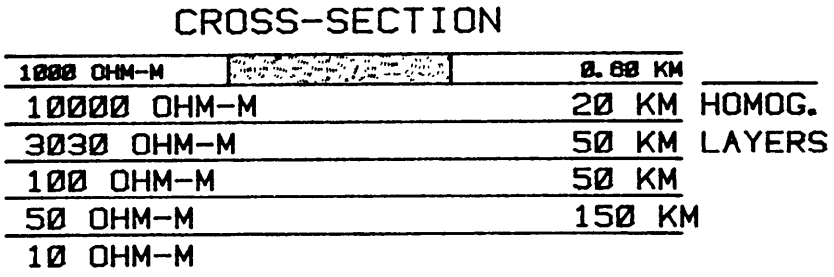
Table A.1.3--Numerical Error Analysis

No. of Layers	Thickness	$\frac{\Delta z}{\delta}*100\%$	$\frac{\sqrt{2\pi}\Delta z}{\Delta L}*100\%$	Max. error outside	Max. error inside
6	100m	1%	9%	0	0
3	200m	1.7%	18%	1%	13%
2	300m	2.7%	27%	37%	500%

No. of Layers	Thickness	$\frac{\Delta z}{\delta}*100\%$	$\frac{\sqrt{2\pi}\Delta z}{\Delta L}*100\%$	Max. error outside	Max. error inside
6	100m	9%	1%	0	0
3	200m	18%	1.7%	0.1%	2.2%
2	300m	27%	2.7%	0.2%	5.0%
1	600m	53%	5.3%	0.3%	12%

Figure A.1.1--Model for Numerical Evaluation of Error Criteria





APPENDIX B

The AC magnetic field induces regional electric fields which we treat as background fields in the following analysis. These background fields are perturbed by local conductivity heterogeneities. We recognize three different mechanisms responsible for these perturbations at low frequencies. Figure B.1.1 illustrates these mechanisms. The first is vertical current gathering, and has been discussed extensively by Ranganayaki and Madden (1980). The second is horizontal current gathering. These first two mechanisms have essentially DC behavior--their electric field magnitudes are frequency-independent. The third is local induction. The regional magnetic field creates local current cells in a good conductor. This local induction is frequency-dependent. Each mechanism has a different influence on the spatial behavior of the local electric field, so the importance of identifying the dominant contribution is clear. We present a simple method of estimating each contribution to within an order of magnitude. This estimation process is only valid for frequencies at which the skin depth is much greater than the thickness of the heterogeneous region.

We consider the vertical current mechanism first. We esitmate the electric field change due to vertical current gathering by a conductive body. Ranganayaki and Madden (1980) give the solution for the perpendicular electric

field over two anisotropic quarter-spaces (see Figure B.1.2) as

$$E_{x1} = E_{01} - \frac{\sigma_1 E_{01} - \sigma_2 E_{02}}{\sigma_1 + \sigma_2} \exp\left(-|x|/\sqrt{(\sigma_1 \Delta Z_1 \rho_1 \Delta Z_2)}\right) \quad \text{(B.1.1)}$$

$$E_{x2} = E_{02} - \frac{\sigma_1 E_{01} - \sigma_2 E_{02}}{\sqrt{(\sigma_1 \sigma_2) + \sigma_2}} \exp\left(-|x|/\sqrt{(\sigma_2 \Delta Z_1 \rho_2 \Delta Z_2)}\right) \quad \text{(B.1.2)}$$

where E_{01} and E_{02} are respective 1-D solutions, σ_1 and σ_2 are horizontal conductivities, and ρ_1 and ρ_2 are vertical resistivities. We see from (B.1.2) that the electric field is enhanced on the resistive side of the contact because the conductor attracts current. This excess current is responsible for a change in the electric field. The change is

$$\Delta E_{out,AD} = \frac{\sigma_1 E_{01} - \sigma_2 E_{02}}{\sqrt{(\sigma_1 \sigma_2) + \sigma_2}} \exp\left(-|x|/\sqrt{(\sigma_2 \Delta Z_1 \rho_2 \Delta Z_2)}\right) \quad \text{(B.1.3)}$$

The field on the conductive side of the contact is depressed, and reaches a minimum at the contact. The field increases as we recede from the boundary because vertical current is flowing into the conductor. The electric field increase is

$$\Delta E_{in,AD} = \frac{\sigma_1 E_{01} - \sigma_2 E_{02}}{\sigma_1 + \sigma_2}\left[1 - \exp\left(-|x|/\sqrt{(\sigma_1 \Delta Z_1 \rho_1 \Delta Z_2)}\right)\right] \quad \text{(B.1.4)}$$

We now have expressions for the changes in electric field

on both sides of the contact. These changes are due to vertical current gathering. Note that (B.1.3) and (B.1.4) are approximate because they are the field changes over quarter-spaces, while the actual bodies are three-dimensional.

The next mechanism we examine is horizontal current gathering. This mechanism has DC behavior at low frequencies, so we will just consider an electrostatic solution. Lee (1977) presents the solution for a conductive ellipsoid, but his solution contains both horizontal and vertical current gathering effects. We are interested in just the horizontal effects, so we simplify his problem to a vertical 2-D body with elliptical cross-section (Figure B.1.3). This new problem will have no vertical current gathering.

We assume the incident electric field, E_0, is in the x direction. The equation describing the elliptical surface is

$$\frac{x^2}{a^2} + \frac{y^2}{b^2} = 1 \qquad \text{(B.1.5)}$$

The solution for the electrostatic potential inside and outside the conductive body (Lee, 1977) is

$$V_{out} = -E_0 x + E_0(\varepsilon-1)\left(\frac{A_\lambda x}{1+A_0(\varepsilon-1)}\right) \qquad \text{(B.1.6)}$$

$$V_{in} = -\frac{E_0 x}{1+A_0(\varepsilon-1)} \qquad \text{(B.1.6)}$$

where $\varepsilon=\sigma_1/\sigma_2$ and

$$A_\lambda = \frac{ab}{2}\int_\lambda^\infty \left(\frac{du}{(a^2+u)^{1.5}(b^2+u)^{.5}}\right) \qquad (B.1.7)$$

λ is the positive real root of

$$\frac{X^2}{a^2+\lambda} + \frac{Y^2}{b^2+\lambda} = 1 \qquad (B.1.9)$$

A_0 is A_λ evaluated for $\lambda=0$. We must use a change of variable to integrate (B.1.8). This change of variable we use depends upon whether a>b or a<b. We consider the case a>b first. The change of variable is $a^2+u = (a^2-b^2)/\sin^2\psi$ (Lee, 1977). We substitute this into (B.1.8) and integrate to get

$$A_\lambda = \frac{ab}{a^2-b^2}(1-\cos\phi) \qquad (B.1.10)$$

where $\sin^2\phi = (a^2-b^2)/(a^2+\lambda)$. The electric field is the negative gradient of the potential, so

$$E_{in} = \left(\frac{E_0}{1+A_0(\varepsilon-1)},\ 0\right) \qquad (B.1.11)$$

$$E_{out} = \left[E_0+\frac{E_0(\varepsilon-1)}{1+A_0(\varepsilon-1)}\left(-A_\lambda-x\frac{\partial A_\lambda}{\partial x}\right),\ \frac{E_0(\varepsilon-1)}{1+A_0(\varepsilon-1)}\left(-y\frac{\partial A_\lambda}{\partial y}\right)\right] \qquad (B.1.12)$$

We choose to look at the electric field only along the symmetry axis of the conductive body (given by y=0), so E_y is zero. The derivative of (B.1.10) with respect to x is

$$\frac{\partial A_\lambda}{\partial x} = \left[\frac{ab}{a^2-b^2}\sin\phi\right]\left[-\frac{\tan\phi}{2(a^2+\lambda)}\right]\left[\frac{2x}{a^2+\lambda}\right]\left[\frac{x^2}{(a^2+\lambda)^2}+\frac{y^2}{(b^2+\lambda)^2}\right]^{-1} \tag{B.1.13}$$

We evaluate (B.1.13) along a line of y=0,and substitute this and (B.1.10) into (B.1.12) to get

$$E_{out} = E_0+\left[\frac{E_0(\varepsilon-1)}{1+A_0(\varepsilon-1)}\right]\left[\frac{1-\cos\phi}{\cos\phi}\right]\left[\frac{ab}{a^2-b^2}\right] \tag{B.1.14}$$

We desire the change in the electric field due to the presence of the conductor. The background field outside is E_0, so from (B.1.14)

$$\Delta E_{out,h} = \left[\frac{E_0(\varepsilon-1)}{1+A_0(\varepsilon-1)}\right]\left[\frac{1-\cos\phi}{\cos\phi}\right]\left[\frac{ab}{a^2-b^2}\right] \tag{B.1.15}$$

The background field inside is not so simple. We want the electric field change due to excess current gathered by the conductor. The background current density is $\sigma_2 E_0$. The background field is that field that would be present is the background current were flowing in a conductor with conductivity σ_1. The background field is thus $(\sigma_2 E_0)/\sigma_1$, and the electric field change inside is

$$\Delta E_{in,h} = \frac{E_0}{1+A_0(\varepsilon-1)} - \frac{\sigma_2}{\sigma_1} E_0 \tag{B.1.16}$$

These field change estimates due to horizontal current

gathering are only valid for a>b. We now consider the case a<b.

We must use the substitution $a^2+u=(b^2-a^2)/\sin^2\psi$ for b>a. This results in the following expression for A_λ

$$A_\lambda = \frac{ab}{a^2-b^2}\left[\sqrt{\left(\frac{b^2+\lambda}{a^2+\lambda}\right)}-1\right] \qquad \text{(B.1.17)}$$

We go through the same manipulations that led to (B.1.15) and derive an alternate expression for $\Delta E_{out,h}$

$$\Delta E_{out,h} = -\frac{E_0(\varepsilon-1)}{1+A_0(\varepsilon-1)}\left[\frac{ab}{b^2-a^2}\left(\frac{\sqrt{(b^2-a^2+x^2)}}{x}-1\right)-\frac{ab}{x\sqrt{(b^2-a^2+x^2)}}\right] \qquad \text{(B.1.18)}$$

The expression for $\Delta E_{in,h}$ is unchanged for b>a. All of the electric field changes ((B.1.15), (B.1.16), and (B.1.18)) are approximations because the elliptical body is two-dimensional.

The last mechanism is local induction. The fluctuating magnetic field induces current cells in the conductive body. The magnetic field has a large constant component (80-90% of the total field) within the body, and this component is coupled to the fundamental mode (illustrated in Figure B.1.1). We estimate the electric field due to this fundamental mode by using Faraday's law

$$\int_l E \cdot dl = j\omega\mu \int_A H \cdot da \qquad (B.1.19)$$

where A is the area encircled by the path l. The area for the fundamental mode is roughly the cross-section of the body (ΔY long and ΔZ thick). We assume E is constant on the path since the current is circulating in a loop, and that the magnetic field threading the loop is constant. Equation (B.1.19) reduces with these assumptions to

$$E(2\Delta Y+2\Delta Z) = j\omega\mu H \Delta Y \Delta Z \qquad (B.1.20)$$

Equation (B.1.20) simplifies even further because $\Delta Z << \Delta Y$. The final expression for E is

$$E_{induct} = \frac{j\omega\mu H \Delta Z}{2} \qquad (B.1.21)$$

Local induction effects also exist outside the conductor. A rough approximation to these effects is the field due to a horizontal magnetic dipole with moment m=I*area. Stratton (1941) gives the far field electric field as

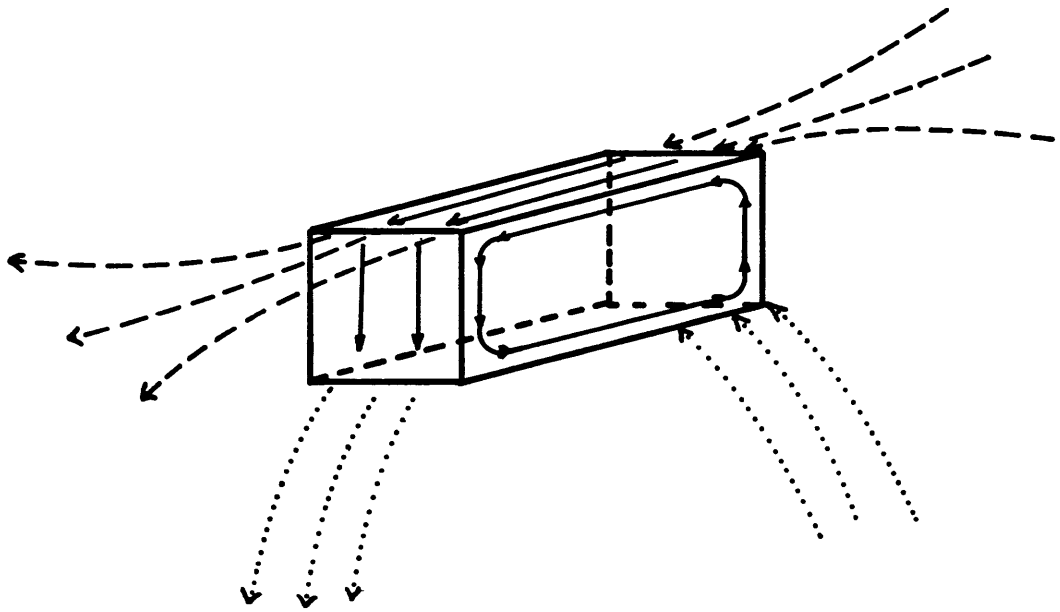
$$E_\phi = \frac{k^2}{4\pi} \sqrt{\frac{\mu}{\varepsilon}} \left(\frac{1}{R} + \frac{j}{kR^2}\right) |m| \sin\theta \qquad (B.1.22)$$

where E_ϕ is the ϕ component in a spherical coordinate system aligned along the axis of the horizontal dipole. The axis of the conductor is perpendicular to the dipole axis, so the

line y=0 has $\theta=90°$. The ϕ vector is aligned parallel to the z axis at the surface, so the electric field given by (B.1.22) is all E_z. There is no horizontal electric field at the surface due to the magnetic dipole to a first approximation. Local induction effects can thus be neglected outside the conductor in this analysis.

We have presented methods for determining the dominant mechanism governing local electric field perturbation. The mechanisms are local induction, horizontal current gathering, and vertical current gathering. Each produces a different spatial field behavior. The field separation procedure outlined here is only approximate, but suffices for an order-of-magnitude study. We will apply this method to the models presented in Section 2.3 when discussing the MT sounding curves.

Figure B.1.1--Field Perturbation Mechanisms



——Local Induction

---Horizontal Current Gathering

·····Vertical Current Gathering

Figure B.1.2--Anisotropic Quarter-Spaces

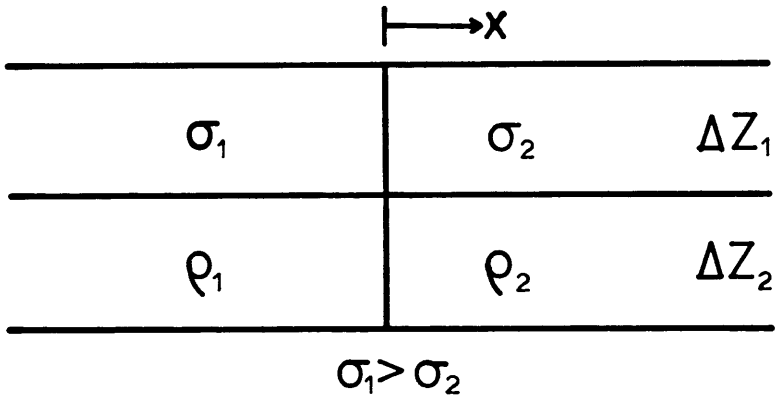
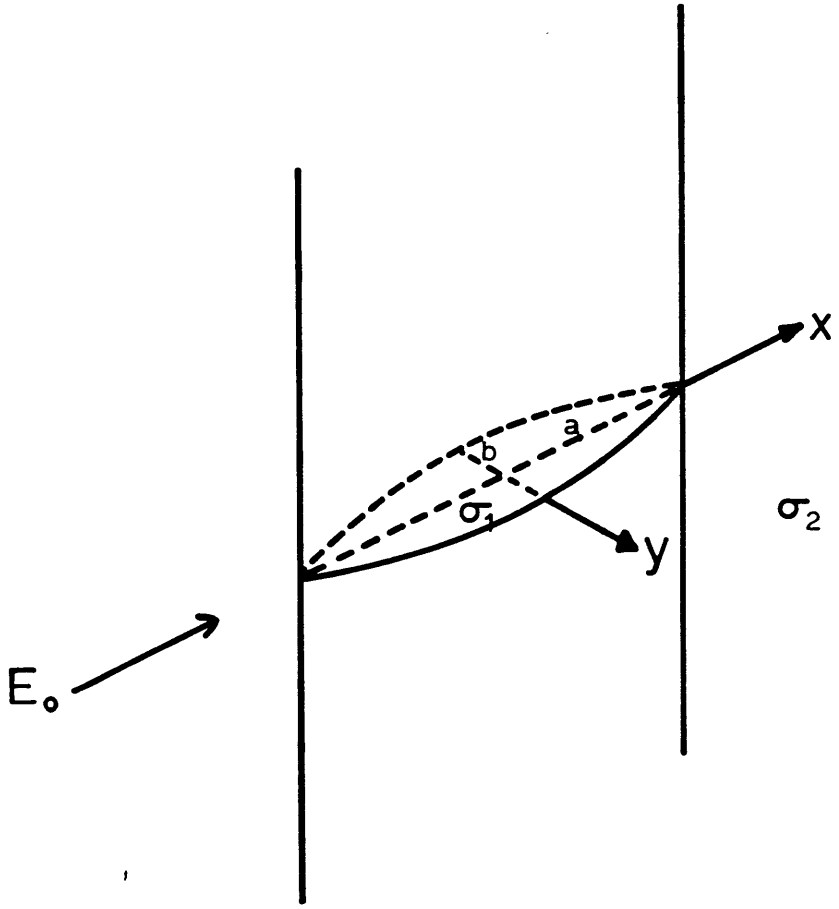


Figure B.1.3--Two-Dimensional Elliptical Body



APPENDIX C

We present here the processing done on the raw power spectra from Beowawe to produce the needed impedance tensor estimates. Geotronics Corporation records time series which are filtered to pass one frequency decade. The effective passband of the system is about 3 decades, centered on the single decade of interest. These time series are Fourier transformed, and power estimates are computed between all channels. These are the raw power spectra supplied by Geotronics on computer tape. The data consist of 5 overlapping frequency bands (runs) which need to be 'stacked' to yield a single power estimate at any given frequency. Each sounding curve in Chapter 4 is a compilation of 5-10 data runs over different frequency decades.

We use constant bandwidth averaging to achieve this 'stacking'. Each band is .1 frequency decade wide. All power estimates within each band are weighted by the number of spectral harmonics contributing to that estimate and then summed. The sum is normalized by the total number of spectral harmonics used to produce the sum. This procedure yields a single average spectral estimate for each .1 frequency decade over the 5 decades for which we have data.

The next step in the process is to estimate impedance tensors for each frequency band. We use two different estimates called the E estimate and the H estimate. The

impedance tensor is slowly varying for a narrow frequency band so

$$\begin{bmatrix} E_x(\omega) \\ E_y(\omega) \end{bmatrix} = \begin{bmatrix} Z_{xx} & Z_{xy} \\ Z_{yx} & Z_{yy} \end{bmatrix} \begin{bmatrix} H_x(\omega) \\ H_y(\omega) \end{bmatrix} \qquad \text{(C.3.1)}$$

We postmultiply by $(H^*)^T$, average over a narrow frequency band, and invert HH^T to yield the H estimate of the impedance tensor

$$Z_H = \begin{bmatrix} \langle E_x H_x^* \rangle & \langle E_x H_y^* \rangle \\ \langle E_y H_x^* \rangle & \langle E_y H_y^* \rangle \end{bmatrix} \begin{bmatrix} \langle H_x H_x^* \rangle & \langle H_x H_y^* \rangle \\ \langle H_y H_x^* \rangle & \langle H_y H_y^* \rangle \end{bmatrix}^{-1} \qquad \text{(C.3.2)}$$

where $\langle\ \rangle$ is the average power estimate over .1 frequency decade band. The E estimate can be similarly derived

$$Z_E = \begin{bmatrix} \langle E_x E_x^* \rangle & \langle E_x E_y^* \rangle \\ \langle E_y E_x^* \rangle & \langle E_y E_y^* \rangle \end{bmatrix} \begin{bmatrix} \langle H_x E_x^* \rangle & \langle H_x E_y^* \rangle \\ \langle H_y E_x^* \rangle & \langle H_y E_y^* \rangle \end{bmatrix}^{-1} \qquad \text{(C.3.3)}$$

Sims, et. al. (1979) show that the E estimate is biased up by noise in the electric fields, and the H estimate is biased downward by noise in the magnetic fields. These two estimates should thus bracket the noise-free impedance tensor estimate.

We also look at predicted E field coherencies as a

measure of noise. The predicted E field is calculated from the tensor impedance

$$E_{i\ pred} = Z_{ix}H_{x\ data} + Z_{iy}H_{y\ data} \qquad (C.3.4)$$

We then compute the coherency between the predicted field and the measured field

$$coh(E_{i\ pred}E_{i}^{*}{}_{data}) = \frac{\langle E_{i}^{*}{}_{data}E_{i\ pred}\rangle}{\sqrt{(\langle E_{i\ pred}E_{i}^{*}{}_{pred}\rangle\langle E_{i\ data}E_{i}^{*}{}_{data}\rangle)}} \qquad (C.3.5)$$

This coherency can be rewritten in terms of the measured power spectra solely. Tensor estimates in the Beowawe data set were rejected if either of the predicted E coherencies was below 0.9. This corresponds to about 45% noise (noise=$\sqrt{(1-coh^2)}$).

Swift (1967) demonstrates that the impedance tensor reduces to two off-diagonal elements along symmetry axes for a 2-D structure. This off-diagonalization also occurs for tensors along symmetry axes of 3-D structures. We rotate the tensor about the z axis to find these axes of symmetry. The rotated tensor is

$$Z' = \begin{bmatrix} \cos\theta & \sin\theta \\ -\sin\theta & \cos\theta \end{bmatrix} \begin{bmatrix} Z_{xx} & Z_{xy} \\ Z_{yx} & Z_{yy} \end{bmatrix} \begin{bmatrix} \cos\theta & -\sin\theta \\ \sin\theta & \cos\theta \end{bmatrix} \qquad (C.3.6)$$

We minimize the magnitude of the sum of the diagonal elements of the rotated tensor to choose the symmetry directions. This sum is often non-zero after it has been minimized however, because of data noise or the presence of 3-D structures. We use two further quantities, the skew and ellipticity, as indicators of 3-D structure (or noise). These quantities are defined in Section 3 of Chapter 2, so need not be restated here. Apparent resitivities and phases are computed from the off-diagonal elements of the rotated tensor and plotted versus frequency.

LaTorraca (1981) has developed an alternate method of tensor analysis based on eigenvalue decomposition which has some advantages over the conventional method outlined above. LaTorraca's procedure was used on the Beowawe data set, but the high degree of two-dimensionality eliminated any advantage the eigenanalysis had over the conventional method.

APPENDIX D

We prove that the off-diagonal terms in the conductivity tensor are equal in this appendix. This proof assumes that the z axis is one of the principal axes of the medium. There is thus some set of orthogonal axes in the x-y plane for which

$$\sigma = \begin{bmatrix} \sigma_1 & 0 \\ 0 & \sigma_2 \end{bmatrix} \tag{D.1.1}$$

Rotation about the z axis to any set of x-y axes is achieved through matrix multiplication

$$\begin{bmatrix} \sigma_{xx} & \sigma_{xy} \\ \sigma_{yx} & \sigma_{yy} \end{bmatrix} = \begin{bmatrix} \cos\theta & \sin\theta \\ -\sin\theta & \cos\theta \end{bmatrix} \begin{bmatrix} \sigma_1 & 0 \\ 0 & \sigma_2 \end{bmatrix} \begin{bmatrix} \cos\theta & -\sin\theta \\ \sin\theta & \cos\theta \end{bmatrix} \tag{D.1.2}$$

This equation reduces to

$$\begin{bmatrix} \sigma_{xx} & \sigma_{xy} \\ \sigma_{yx} & \sigma_{yy} \end{bmatrix} = \begin{bmatrix} \sigma_1\cos^2\theta+\sigma_2\sin^2\theta & \sin\theta\cos\theta(\sigma_1-\sigma_2) \\ \sin\theta\cos\theta(\sigma_1-\sigma_2) & \sigma_1\sin^2\theta+\sigma_2\cos^2\theta \end{bmatrix} \tag{D.1.3}$$

We see immediately from (D.1.3) that $\sigma_{xy}=\sigma_{yx}$.

BIOGRAPHICAL NOTE

The author was conceived in Berkeley, California (which explains a lot of things). He was born roughly 9 months later on April 27, 1956 in a Quonset hut on Lackland Air Force Base in San Antonio, Texas. His mother was simultaneously experiencing two firsts--her first child and her first thunderstorm. As she put it, 'Life with you as a small child--I'm not sure if the thunderstorm ever ended'. Birth in Texas, for those unfamiliar with Texan customs, automatically confers membership in the Good Ole Boy Club.

Courtesy of the U.S. Air Force, the author was moved many times until he got old enough to move himself. He spent 7 years in Waco, Texas, where he learned a game called "North vs. South" in elementary school. In this game, all the popular (or big) kids in school got together on one side (they were the South) and knocked down everyone else (the North). After living in El Cerrito, California (next to Berkeley!), Wiesbaden, Germany, Escondido, California, and Tucson, Arizona, the author was given the privilege of attending high school in Biloxi, Mississippi. He learned here from an American History teacher that "V.D. was God's way of showing who the sinnners were". He moved to Grandview, Missouri shortly after this pearl of wisdom and finished high school in the 20th Century.

The author chose to attend college, but aside from going to Berkeley, he was not sure what he wanted to do.

He found a short paragraph in a book on careers in physics about the exciting field of geophysics. He had planned to major in physics, but decided what the hell, why not geophysics? He had always enjoyed collecting pretty rocks anyway. The author ended up at the University of California at Riverside after redirection from Berkeley and San Diego. He learned about Beer Drinking, Volleyball, Water Polo, Explosives Fun, and Geophysical Hell-Raising in the Desert from 1974 to 1978 under the tutelage of Shawn Biehler and Tien C. Lee. He decided at this time that field geophysics was not a bad life after all.

The author began work with Ted Madden at the Massachusetts Institute of Technology in 1978. He enjoyed living on the East Coast so much that he promptly arranged so that he could spend 6-8 months a year out West. He continued his work in Water Polo, Volleyball, and Beer Drinking during his rare visits to the East Coast. He also learned something about being flexible from his advisor during this time. He does not and never has played ice hockey, however!

The author quickly discovered the monetary and travel benefits of summer employment with the oil companies. He has had the opportunity to rape and pillage the environment in such diverse places as the Michigan swamps, south Texas, Arizona, Berkeley (there it is again!), and the San Juan Mountains of Colorado while ostensibly employed by big oil. His work with Ted Madden on earthquake prediction (sic) has

allowed him to sample the charms of the California towns of Palmdale and Hollister.

The author has taken a position with Chevron Oil Field Research Company in La Habra, California as one-half of their non-seismic research group. He is a member in good standing of the Sierra Club.